

Design, Fabrication and Characterization of Mid-Infrared Strip Waveguide for Laser Spectroscopy in Liquid Environments

THÈSE N° 5577 (2012)

PRÉSENTÉE LE 13 DECEMBRE 2012

À LA FACULTÉ DES SCIENCES ET TECHNIQUES DE L'INGÉNIEUR

INSTITUT DE MICROTECHNIQUE

PROGRAMME DOCTORAL EN PHOTONIQUE

ÉCOLE POLYTECHNIQUE FÉDÉRALE DE LAUSANNE

POUR L'OBTENTION DU GRADE DE DOCTEUR ÈS SCIENCES

PAR

Yu-Chi CHANG

acceptée sur proposition du jury:

Prof. N. de Rooij, président du jury
Prof. H. P. Herzig, directeur de thèse
Prof. B. Lendl, rapporteur
Prof. M. W. Sigrist, rapporteur
Dr L. Sirigu, rapporteur



ÉCOLE POLYTECHNIQUE
FÉDÉRALE DE LAUSANNE

Suisse
2012

Abstract

Optical sensors based on the interaction between molecular vibrations and mid infrared radiations attracted high attentions in the last decades. In this study, we present the development of a waveguide evanescent field sensor based on the absorption spectroscopy in liquid environments. The device consists of a single mode strip waveguide integrated with a microfluidic system. With a quantum cascade laser at the wavelength of 5.8 μm , we demonstrate the detection of cocaine dissolved in tetrachloroethylene (PCE).

Mid infrared germanium waveguides on silicon have been proposed but not experimentally demonstrated. Here we realize this new type of waveguide with a monocrystalline germanium layer on a silicon substrate (Ge-on-Si) with standard photolithography and reactive ion etching. It is designed to be singlemode in transverse magnetic polarization at 5.8 μm . We used a method based on the Fabry-Perot resonance to measure the propagation loss, and the achieved lowest loss is 2.4 dB/cm. The bending loss was measured to be 0.12 dB per 90° bend with the radius of 115 μm .

A microfluidic chip made from a UV-curable adhesive is integrated to the Ge-on-Si waveguide. This is the first integration of this waveguide with a microfluidic system. Solutions of cocaine in PCE flow in the microfluidic channel and absorb the light in the evanescent field. A reference waveguide and an integrated Y-junction eliminate the noise from coupling fluctuations, and the limit of detection is calculated to be 5 $\mu\text{g/ml}$.

Mid infrared photonics can be further developed based on the platform of Ge-on-Si waveguides. We demonstrate a detection of refractive index changes with a Mach-Zehnder interferometer integrated with a microfluidic system. Subwavelength structures for antireflection of the waveguide facets are also experimentally tested. We foresee an increasing development and applications based on this waveguide in the mid infrared.

Keywords: mid infrared waveguide, germanium waveguide, mid infrared photonics, microfluidics in mid infrared, waveguide spectroscopy, mid infrared spectroscopy, germanium on silicon, cocaine detection, mid infrared integrated interferometer.

Résumé

Dans cette dernière décennie, les senseurs optiques se basant sur l'interaction entre les vibrations moléculaires et les rayonnements infrarouges (IR) moyens ont attiré beaucoup d'attention. Dans cette étude, nous présentons le développement d'un senseur d'onde évanescente basé la spectroscopie à absorption IR dans un milieu liquide. Le dispositif est constitué d'un guide d'onde rectangulaire monomode associé à un système microfluidique. Un laser à cascade quantique d'une longueur d'onde de $5.8\text{ }\mu\text{m}$ est utilisée comme source IR. Ce dispositif est finalement exploité pour démontrer la détection de cocaïne dissoute dans du tetrachloroethylene (PCE).

La fabrication de guides d'ondes IR en germanium sur silicium a été proposé mais jamais validé expérimentalement jusqu'à présent. Ici, nous avons réalisé un nouveau type de guide d'ondes avec une couche mono-crytalline de germanium sur un substrat de silicium (Ge-on-Si) par photolithographie standard et gravure par ions réactifs. La géométrie rectangulaire du guide a été choisie afin d'obtenir un mode unique en polarisation transverse magnétique (TM) à une longueur d'onde de $5.8\text{ }\mu\text{m}$. Nous avons utilisé une méthode s'appuyant sur les résonances Fabry-Perot (créées par les réflexions en entrée et sortie du guide) pour estimer les pertes de propagation qui sont de l'ordre de 2.4 dB/cm pour l'échantillon le plus performant. Les pertes liées à la courbure du guide sont de 0.12 dB pour un angle de 90° avec un rayon de courbure de $115\text{ }\mu\text{m}$.

Un dispositif microfluidique, réalisé avec une résine photopolymérisable par irradiation UV, a été intégré au système de guide d'onde Ge-on-Si. Plusieurs solutions de cocaïne injectées dans le canal microfluidique ont été détectées en mesurant l'absorption spécifique du signal IR par la cocaïne dans le champ évanescent du guide. Un guide d'onde de référence et une jonction Y ont été utilisés pour éliminer le bruit lié aux fluctuations de couplage. La limite de détection ainsi obtenue est de $5\text{ }\mu\text{g/ml}$.

La photonique dans le moyen infrarouge pourrait être développée sur la base des plate-formes de guide d'onde 'Ge-on-Si'. Nous avons démontré une détection de changements de l'indice de refraction avec un interféromètre de Mach-Zehnder intégré avec un système microfluidique. Nous avons également étudié expérimentalement la possibilité de réduire les réflexions aux extrémités du guide en y introduisant des nanostructures. Nous prévoyons une augmentation du développement et des applications basés sur ce guide d'onde dans le moyen-infrarouge.

Mots clés: guide d'onde moyen-infrarouge, guide d'onde en germanium, photonique moyen-infrarouge microfluidique dans le moyen-infrarouge spectroscopie dans le moyen-infrarouge germanium-on-silicon, detection de cocaine, interferomètre intégré dans le moyen-infrarouge.

Contents

1	Introduction	3
2	Sensing scheme	5
2.1	Sensing in the evanescent field	5
2.2	Absorption spectroscopy in the evanescent field	7
2.3	Mid infrared absorption spectroscopy	10
2.4	Mid infrared laser spectroscopy in liquid phases	11
3	Germanium strip waveguide on silicon	15
3.1	Materials	15
3.2	Waveguide design	17
3.3	Waveguide fabrication	19
3.3.1	Photolithography	19
3.3.2	Pattern transfer with dry plasma etching	20
3.3.3	Edge polishment	25
3.4	Waveguide coupling	26
3.4.1	End-fire method	26
3.4.2	Butt coupling method	30
3.5	Propagation loss measurement	32
3.5.1	Fabry-Perot resonance method	33
3.5.2	Measurement results	36
3.6	Bending loss measurement	40

4 Cocaine detection in liquids with a Ge-on-Si strip waveguide	43
4.1 Sensing scheme and the selection of wavelength	44
4.2 Integrated microfluidic chip	46
4.3 Static measurement of cocaine with changes of propagation loss	49
4.4 Dynamic measurement of cocaine	51
4.4.1 Thermal fluctuations due to Fabry-Perot fringes	53
4.4.2 Noise due to misalignment of the coupling	55
4.5 Reduction of thermal fluctuations due to Fabry-Perot fringes	56
4.5.1 Temperature control of the device	57
4.5.2 Reduction of the Fabry-Perot fringe contrast	58
4.5.3 Noise reduction by a pulse-driving QCL	60
4.6 Response time of the device	65
4.7 Effective path length of the waveguide evanescent field	67
4.8 Reference waveguide and integrated Y splitters	68
4.9 Long waveguide for enhanced interaction	72
4.10 Varied waveguide width	74
4.11 Outlook of sensitivity improvement	75
5 Outlook of Ge-on-Si mid IR photonics	77
5.1 Mach-Zehnder interferometer based on Ge-on-Si waveguide	77
5.1.1 Temperature actuated Mach-Zehnder interferometers	78
5.1.2 Mach-Zehnder interferometer integrated with microfluidics	80
5.2 Antireflection for end-facets of Ge-on-Si waveguides	83
5.2.1 Single quarter wave film	84
5.2.2 Subwavelength structures for antireflection	85
6 Conclusion	89
Bibliography	91
Acknowledgement	99
Curriculum Vitae	101

Chapter 1

Introduction

In the wavelength range of mid infrared (mid IR) from 2.5 to 25 μm , where light has strong interactions with molecular vibrations, we see an increasing attention on applications in the fields of chemical and biological sensing, trace gas detection, environmental monitoring, spectroscopy, astronomy, metrology, security, and industrial process control. A main driving force here is the development of the light sources, especially the quantum cascade lasers (QCLs) [1], which provide a compact laser source for sensing of trace gases. On the other hand in liquid environments, a low loss integrable waveguide is needed for the development of compact mid IR spectroscopy devices.

Mid IR waveguides in silicon have been made from silicon-on-insulator and silicon-on-sapphire. In this study, we presented the development of a new type of waveguide based on a monocrystalline germanium layer on a silicon substrate. It extended the usable wavelength to a wider range and can be an excellent platform for further development of mid IR photonics [2] like mid IR optoelectronics in silicon, mid IR plasmonics, and nonlinear applications like frequency combs [3].

In a compact sensing device for liquid samples, a microfluidic system has the advantage of small sample volume and can integrate multiple functions for a lab-on-chip solution. Based on Ge-on-Si waveguides, we aimed to develop a portable optical sensing device which integrates a microfluidic system to detect chemical and biomedical substances, using mid IR spectroscopy in liquid environments. Cocaine detection was a pilot example to demonstrate this technology.

In the following chapters, we will present the basic components including singlemode waveguides, low loss bends, subwavelength structures for antireflection, and Mach-Zehnder interferometer. By incorporation with integrated microfluidic systems, mid IR photonics based on Ge-on-Si waveguides showed great potential in (bio-) chemical sensing applications.

In chapter 2, we introduced the sensing scheme of mid IR waveguide spectroscopy in liquids. ATR (attenuated total reflection) technique shows advantage over transmissive measurements and has been used for cocaine detection [4]. Based on a similar scheme of light absorption in the evanescent field, optical waveguides show the potential to be integrated with lasers and detectors for sensing purposes [5-8].

Chapter 3 describes the development of mid IR Ge-on-Si strip waveguide, including design, fabrication, and optical characterization. A method based on the Fabry-Perot resonances was used for the measurements of propagation losses and the bending loss.

Chapter 4 presents the detection of cocaine with a Ge-on-Si waveguide integrated with a microfluidic system, including the fabrication and the measurement. To improve the performance of the device, we used several methods to increase the signal level and to reduce the system noises, including an integrated reference waveguide.

In chapter 5, we presented further development in mid IR photonics based on Ge-on-Si waveguide, including integrated Mach-Zehnder interferometer and subwavelength structures for antireflection of the waveguide facets.

Chapter 6 presents the conclusion.

Chapter 2

Sensing scheme

In the visible and near infrared, integrable optical devices for (bio-) chemical sensing in liquid environments are mostly based on the measurement of refractive index changes and require surface functionalized layers.

In the mid infrared, however, strong and unique absorption spectrum of each molecule can provide a solution which is free of labels and also free of functionalized layers. In the following, we briefly introduced the sensing schemes of optical sensors which use the light in the evanescent field of a waveguide, and the potentials of integrable devices for mid IR spectroscopy in liquids.

2.1 Sensing in the evanescent field

A dielectric optical waveguide guides light with the phenomenon of total internal reflections. It consists of a core which has a refractive index higher than the cladding (and the substrate) materials surrounding the core.

The light is confined in the geometry of the structure and can propagate with supported waveguide modes. A typical example is the glass fibers for optical communication, which have cylindrical shapes. In the case of planar waveguides, as shown in figure 2.1, light is confined in (or near) the core by parallel planar interfaces. At the core-cladding and the core-substrate boundaries, the light penetrates into the cladding and the substrate, and the field amplitude decays exponentially with the distance from the interfaces. The field outside the core material is the evanescent field.

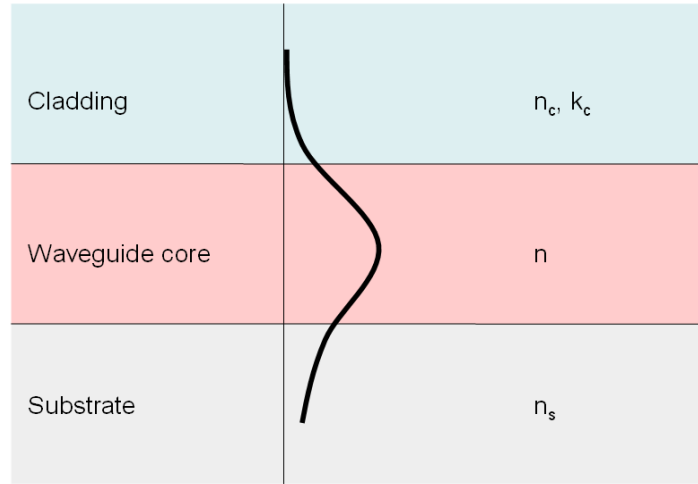


Figure 2.1 Illustration of the evanescent field of a planar waveguide: The evanescent field in the cladding can be used for sensing of changes of the optical constant of the cladding.

The properties of the light propagating in the waveguide are sensitive to the dimensions of the waveguide and the optical constants of the core, the substrate, and the cladding. In the evanescent field in the cladding, variations of the refractive index and/or the absorbance can be detected by measuring the intensity, phase, polarization, or the propagation constant of the light. This type of sensing happens in the vicinity of the core with a thickness near the depth of penetration, which is where the field amplitude decreases to $1/e$. It is determined by [9]

$$d_p = \frac{\lambda}{2\pi \sqrt{n_{eff}^2 - n_c^2}} \quad (eq.2.1)$$

Here λ is the wavelength of the light, n_{eff} is the effective index of the waveguide mode, and n_c is the refractive index of the cladding. For a high refractive index contrast, d_p is usually smaller than several hundred nanometers. This short depth is an advantage to detect only local phenomenon near the waveguide surface, but also a disadvantage when large objects like biological cells are involved in sensing.

One type of these sensors is based on the measurement of the changes of the refractive index in the cladding. The readout can be achieved in several ways, including integrated Mach-Zehnder interferometers [10], optical resonators [11], optical grating [12], or surface plasmon resonances [13] which can be combined with an optical waveguide. These methods can be designed very sensitive that the limit of detection is near several nanograms per milliliter.

However, these methods need an additional recognition layer [14,15] to distinguish specific analytes from other substances. As shown in figure 2.2, a recognition layer is formed on the surface of the waveguide core before the measurement. The cladding is the sample containing the substance to be measured. The recognition layer can bind only the specific analytes. This binding event changes the refractive index of the local area in the evanescent field, and can be measured in a real time that the dynamics of the binding can be recorded. Some examples of the recognition layer are antibodies, nucleic acids, polymers with molecular imprint. Beside an additional process to form the recognition layer, which is often a multi-step process, another disadvantage to use a recognition layer is that the response time is limited by slower diffusion and binding of the analytes. It often requires more than several tens minutes for one measurement [15].

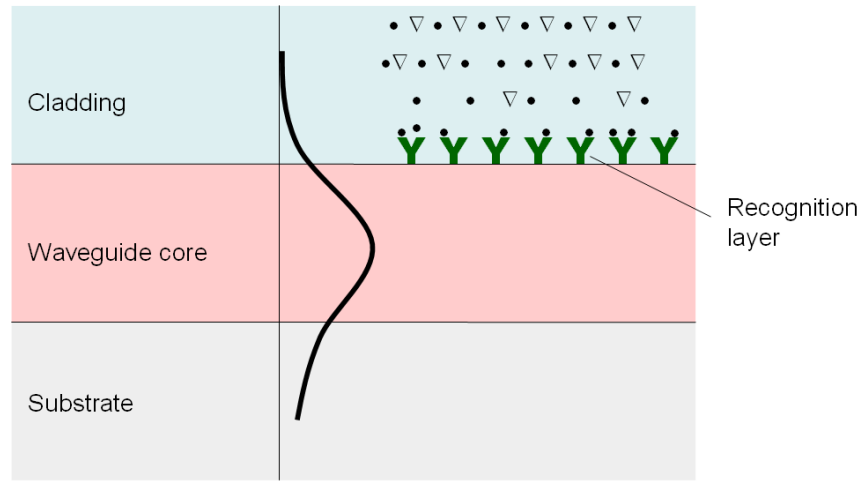


Figure 2.2 Illustration of sensors based on refractive index changes: A recognition layer is necessary to limit the response to specific analytes.

2.2 Absorption spectroscopy in the evanescent field

In the evanescent field, another type of sensing is based on the changes of the absorbance, while the analytes being detected can absorb the light propagating in the waveguide. Therefore the transmittance of the waveguide can be used to determine the concentration of the analytes. According to the Beer-Lambert law, the absorbance A has a linear relationship with the concentration, and can be written as:

$$A = \varepsilon lc \quad (\text{eq.2.2})$$

where ε is the molar absorptivity, l is the path length of light traveling in the sample, and c is the concentration of the analytes. By scanning the wavelength of light, one can obtain the absorption spectrum of the analytes.

The study of the absorption spectroscopy in the evanescent field has started from the fundamental works made by Harrick and Fahrenfort independently [16,17]. They introduced the technique of measuring the reflected light from attenuated total internal reflections (ATR). Conventionally for highly absorbing materials, transmissive-type spectroscopy requires very thin samples to shorten the optical path to the range of 10 μm . The complication of sample preparation even increases more when liquid samples need a thin flow cell. The use of ATR technique largely reduces the difficulties of sample preparations, and hence has a better repeatability of the measurement results. In combination with the FTIR spectroscopy (Fourier transform infrared spectroscopy), ATR-FTIR becomes the most powerful tool for rapid spectral analysis of highly absorbing materials.

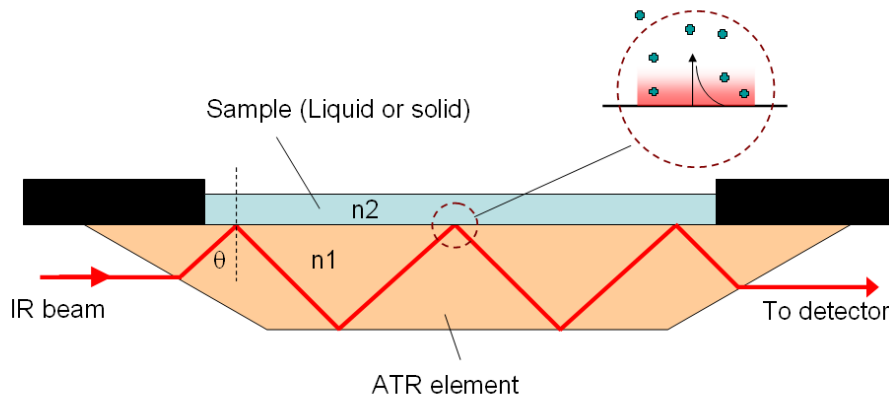


Figure 2.3 Scheme of an ATR measurement: Absorption is in the evanescent field of total internal reflections. The sensitivity is proportional to the number of bounces at the sample-ATR element interfaces.

The basic scheme of the ATR technique is shown in figure 2.3. The light beam is injected into the ATR element, which is made from a transparent material in the spectral range of interest. In the mid IR range, it is often made from ZnSe, Ge, Si, or diamond. On top of the ATR element, a liquid (or solid) sample covers a fixed area with a good contact to the element surface. The refractive index of the ATR element is larger than the sample. At the interface of the ATR and the sample, when the incident angle θ is larger than the critical angle $\theta_c = \sin^{-1}(n_2/n_1)$, total reflection happens, and some part of the light penetrates into the sample with exponentially decayed field intensity. The depth of penetration is determined by

$$d_p = \frac{\lambda}{2\pi \sqrt{n_1^2 \sin^2(\theta) - n_2^2}} \quad (eq.2.3)$$

where λ is the wavelength. The absorption from the sample happens in the evanescent field and can be measured from the spectrum of the reflected light.

Since the depth of penetration is determined only by the wavelength, the refractive indices of the two materials, and the incident angle, the ATR technique provides a very stable and short optical path length for absorption measurement, while the sample is much thicker than the penetration depth.

Here the total effective path length [18] is proportional to the number of bounces happen at the ATR-sample interface. For longer and thinner ATR elements, the bounce numbers are larger. Depending on the requirement of sensitivity, the bounce number often range from 1 to 20, and the total effective path length often vary from less than 1 μm to more than 40 μm .

In the view of ray optics of an optical waveguide, which has a thickness near the wavelength of the light, the number of bounces becomes thousands times larger than the conventional ATR element in a unit length. This means absorption measurement based on a planar optical waveguide provides a higher sensitivity than conventional ATR elements [19]. Furthermore, the small dimensions of these waveguides have several advantages and potentials in spectroscopy and sensing applications.

First, the required sample volume for one measurement can be decreased to a level of tens nanoliters [5], which is an advantage for special applications which have limited amount of samples. Second, an optical waveguide keeps the advantages of stable effective path lengths from ATR elements, and also reduces the device size to the level that it can be integrated into a compact and portable system.

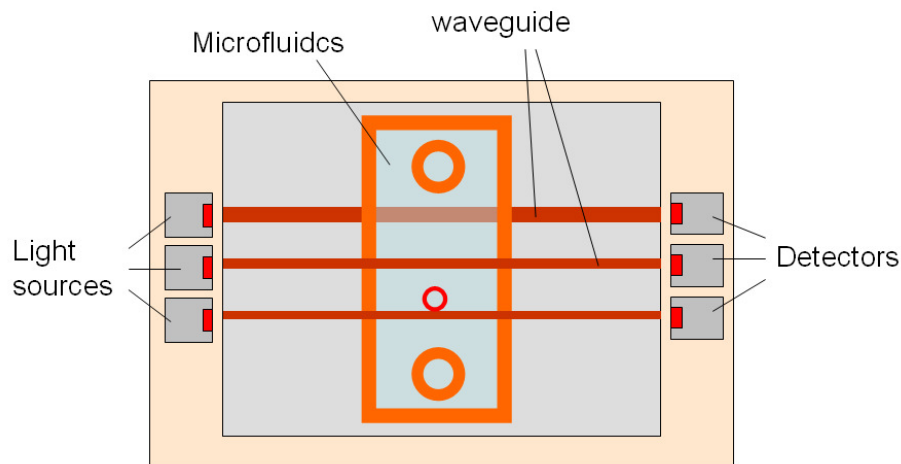


Figure 2.4 Illustration of lab-on-chip sensing scheme: The optical waveguides are integrable to various elements and can provide multiple channels for parallel measurements.

Figure 2.4 shows a scheme of a lab-on-chip system for sensing applications. The optical waveguide has the potential to be integrated into a chip with various elements, including the semiconductor light sources, detectors, and

microfluidic systems for sample treatments before or after the measurement. Besides, parallel measurements with different waveguides and optical elements enhance the functionality of a single chip and can gain more information from one single sample. In addition, the sensing is localized in a small area of the sample, not only in the thickness but also in the lateral dimension when a channel waveguide is used. This allows the study of local phenomena in the samples.

2.3 Mid infrared absorption spectroscopy

Optical measurement based on absorption of light can be used to distinguish different substances without additional intermediate recognition layers, because characteristic absorptions can be obtained during light-matter interactions. In the ultraviolet-visible range, the absorption is related to the electron states of the atoms or the molecules. In the near and mid IR range, the absorption is caused by molecular vibrations and rotational-vibrations. An infrared spectrum contains information of the molecular structures, the strength and the orientation of chemical bonds, and the rotational states of the molecules. As an example, the stretching and bending of water molecules are illustrated in figure 2.5. When the light frequency overlaps with the frequencies of the vibrations, absorption can happen due to the resonances.

Especially in the mid IR range from 2.5 μm to 25 μm , where the light has the frequencies of the fundamental modes of the vibrations, the absorption is much stronger than in the near infrared, where the absorption by molecular vibrations is mostly due to the overtones.

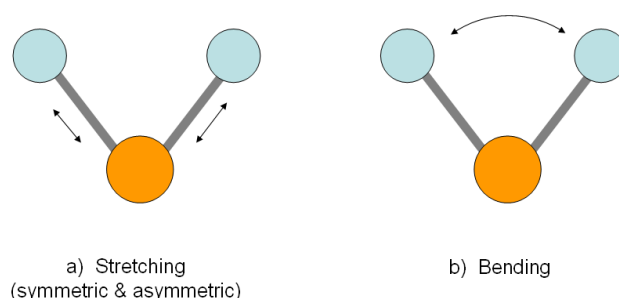


Figure 2.5 Illustration of stretching and bending of a water molecule: a) Stretching corresponds to absorptions of shorter wavelength ($\sim 2.68 \mu\text{m}$). b) Bending of water absorbs light near $6.27 \mu\text{m}$.

Mid infrared spectroscopy is an important tool for chemical identification and analysis, especially for small organic molecules. Absorptions from some functional groups can be assigned in the range about $1500\text{--}3700 \text{ cm}^{-1}$ ($2.7\text{--}6.7 \mu\text{m}$). The range near $600\text{--}1500 \text{ cm}^{-1}$ ($6.7\text{--}16.7 \mu\text{m}$) is the so called fingerprint region, in which the absorption is complex and unique for different molecules. In addition, the sensitivity to the molecular structures provides the selectivity to isomers and isotopes.

In the last several decades, FTIR replaced dispersive infrared instruments and became the standard of infrared spectroscopy. It is easy to use and commercially available, and therefore extends the application of infrared spectroscopy to the fields like biology and forensic analysis. However, their broadband sources showed limitations in some highly absorbing environments, especially in the liquid phase. Instead of a broadband light source, infrared spectroscopy utilizing narrowband sources (e.g. lasers) provides a high spectral power density, and can allow measurement through a longer path [20].

Among various infrared lasers, quantum cascade lasers (QCLs) are the most promising, because of the high power output in a narrow spectral band, the compact dimensions, a long life time, and the high tunability. They are semiconductor lasers and generate light through intersubband transitions designed by multiple quantum structures. Their emission wavelengths are determined by the quantum structures and can be tailored to cover the mid-infrared range and extend to the terahertz region.

QCLs are particularly suitable for sensing applications when singlemode planar waveguides are involved. A main disadvantage of using a singlemode waveguide is the difficulty of light coupling, especially with a broadband light source [19]. The light emitted from a QCL has high spatial and temporal coherences, and has a mode profile which can match well to a singlemode strip waveguide. A high coupling efficiency can be established with a simple butt coupling method.

In addition, the compact sizes of the QCLs enable the potential of integration with other devices (e.g. waveguides and semiconductor detectors) into a lab-on-chip sensing scheme. In an integrated chip, the alignments of the waveguide to the QCL and the detector become robust and less susceptible to mechanical vibrations and thermal displacements which are main reasons of the measurement uncertainty.

2.4 Mid infrared laser spectroscopy in liquid phases

In the mid IR laser spectroscopy, to obtain the characteristic absorption spectra of molecules of interest, the emission spectrum of the laser needs to satisfy some requirements. They depend on the absorption spectra of the analytes.

For small molecules in the gas phase, because the molecules can rotate freely without interaction with other molecules, their spectra show sharp peaks, which are the vibrations combined with discrete rotational levels. Depending on the gas pressure and temperature, the linewidths of these peaks can be smaller than 0.1 cm^{-1} . To resolve the details of these fine structures in gas phases, the laser emission should have a spectrum narrower than the gas linewidths. For this purpose, a distributed feedback (DFB) QCL is good because of the stable and sharp spectrum [21]. Considering the scanning range of wavelength, several cm^{-1} is enough to cover a part of characteristic absorptions when the emission is carefully selected.

For analytes in the liquid phase or dissolved in liquids, the collisions between molecules increase and the molecules are not free to rotate. The

absorption peaks are broadened and lost the fine rotational levels. In addition, the central position of the peaks can be shifted in liquids, when there are intermolecular interactions, such as hydrogen bonding or solute-solvent interactions [22,23]. As an example, figure 2.6 shows the absorption of water in the gas phase and in the liquid phase.

The characteristic absorptions in the liquid phase often have peaks or bands which have the linewidths from several cm^{-1} to several hundreds cm^{-1} . Therefore a narrow spectrum of the laser emission is not obligatory to resolve the band shapes. Instead, a wide tuning range of wavelength becomes important to plot these bands. For DFB QCLs, a small wavelength change can be made with a varied laser current and temperature. For large wavelength changes, external-cavity QCLs have shown a wide tuning range for more than several hundred cm^{-1} [24].

Another issue for spectroscopy in liquid environments is the handling of liquid samples. Conventional methods include using a liquid flow cell for transmissive measurements, or the ATR technique for highly absorbing materials. Microfluidics have been used for infrared detection in separate devices [25-27], and has been integrated with optical waveguides for sensing purposes in the near and mid IR range [28-30]. Because of the small dimensions and multi-functionality, it has great potential for further integrated devices. Recently an integrable droplet-based microfluidic liquid-liquid extraction system is demonstrated [31].

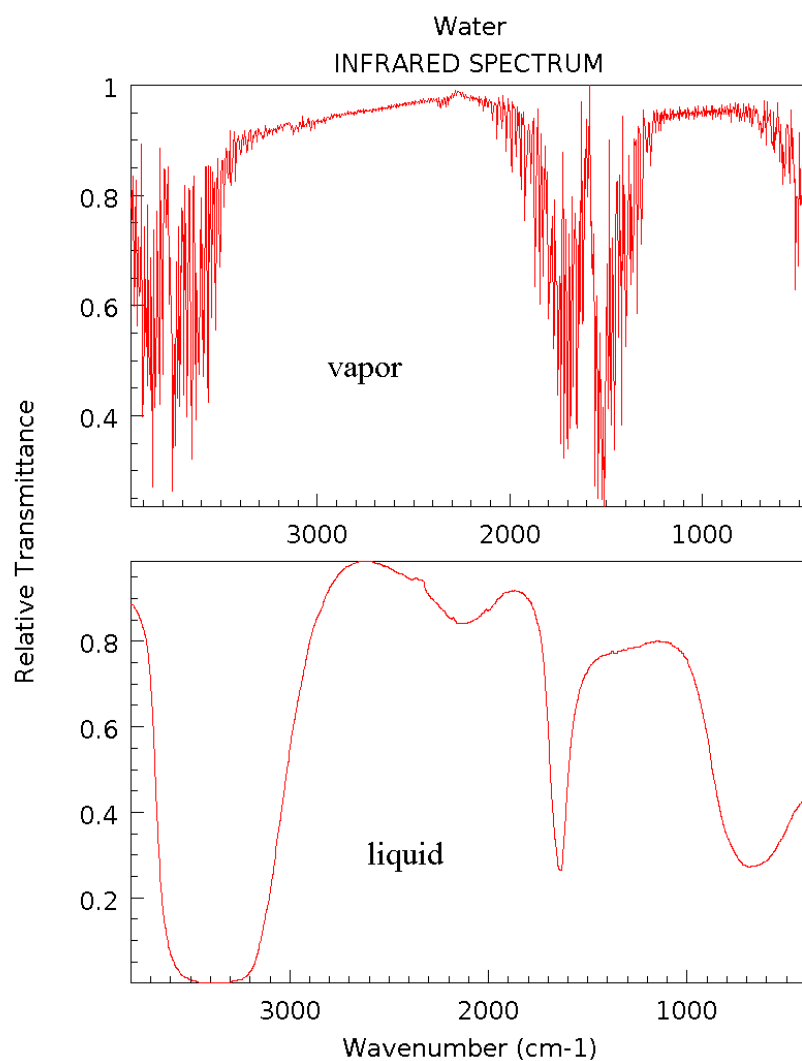


Figure 2.6 Absorption spectra of water in vapor phase and in liquid phase: Sharp peaks in the gas phase are broadened and merged into a band due to increasing collisions between molecules. [32] NIST Chemistry Webbook

Chapter 3

Germanium strip waveguide on silicon

A planar waveguide is a basic building block for various integrated optical devices. Light confined in the geometry of waveguide can propagate through supported modes. In the mid IR range, silver halides and chalcogenide glasses are the dominant materials for passive waveguides. For silicon (Si) compatible devices, planar waveguides based on silicon-on-sapphire and silicon-on-insulator have been demonstrated [33,41,42]. However, the buffer layer absorption and the substrate absorption limit their applicability in the longer wavelength region of mid IR. Here, we presented a strip waveguide based on monocrystalline germanium (Ge) on Si, which has been proposed [33] but not experimentally realized. It was coupled to a quantum cascade laser at $5.8\mu\text{m}$ and a mercury-cadmium-telluride detector for optical characterization. The propagation loss was measured with a method based on Fabry-Perot resonances. The achieved lowest propagation loss was 2.4 dBcm^{-1} , and the bending loss was measured to be 0.12 dB (2.8%) per 90° bend for the radius of $115\mu\text{m}$.

3.1 Materials

In the visible and the near infrared wavelength range, optical waveguides based on silicon dioxide (SiO_2) have been extensively studied and developed for the applications like fiber communications, fiber sensing, and integrated optical devices. However, the material absorption of SiO_2 increases rapidly when the wavelength is above $2\text{--}3\mu\text{m}$.

Various materials have been made into passive components in mid IR. They include silver halides, chalcogenide glasses, Si, Ge, gallium arsenide, indium phosphide, zinc selenide, calcium fluoride, and some metal fluorides. Figure 2.1 shows the transmission spectra of several materials measured with

Fourier transform infrared spectroscopy. The Fresnel reflection was included and reduced the transmission of some materials with high refractive index. Ge and Si had wide ranges of good transmission in mid-IR. Due to water molecules in the atmosphere, some ripples appeared near 6 μm during the measurements.

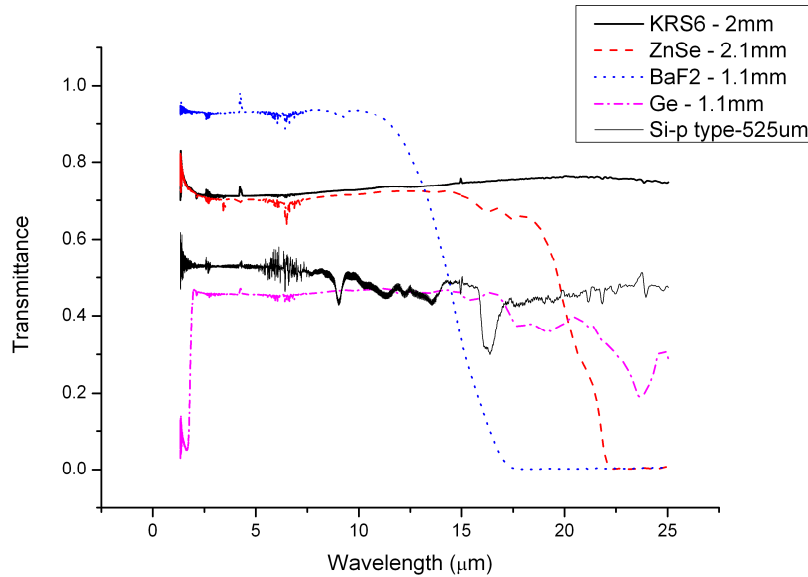


Figure 3.1 Transmission spectra of some materials for the mid-IR: They are measured with FTIR spectroscopy and include Fresnel reflection. Ge and Si have a wide range of transmission in the mid-IR.

Silver halide fibers [34,35] have been used for high power laser transmission (e.g. CO₂ laser transmission for medical applications), and also for chemical sensing with spectroscopy technique in liquid environments [36]. Planar waveguides made from this material have also been demonstrated in singlemode and multimode transmissions [37,38]. The advantage of these waveguides is a wide spectrum of low absorption in the range of 3-30 μm , but the fabrication process still need to be improved to reduce the propagation losses [38,39].

Chalcogenide glasses have the flexibility of micro structuring and attract great interest for various photonics devices. IR fibers, planar waveguides, resonators, and various passive and active devices have been demonstrated with chalcogenides [8,28,40]. Their transmission range can be tuned from visible to the far-infrared, but some chalcogenide glasses contains toxic elements (e.g. arsenic or selenium), and require special care when handling and machining these materials.

In Si based material systems, silicon on insulator wafers (SOI) are very promising for the wavelength of 1.2-3.6 μm [33]. Silicon on sapphire wafers (SOS) extended the usable wavelength range to near 6 μm [41,42]. However, due to the buffer layer absorption and the substrate leakage, the propagation loss increases rapidly for longer wavelengths. Therefore, mid-IR photonics in Si needs another material system to cover a wider wavelength range.

Ge has a broad transparent wavelength range (2-14 μm) in the mid-IR [2]. It is an important material for IR windows and lenses, and has been made into fibers, and also planar waveguides on ZnS and IRTRAN2 [43-46]. Ge and Si have refractive indices around 4 and 3.4 respectively, and therefore guiding can be achieved by their index contrast. In addition, Ge and Si are non-toxic, bio-compatible [47] and also compatible with Si complementary metal oxide semiconductor (CMOS) technology. Active devices like Ge on Si laser at 1590-1610 nm have also been reported [48]. Monocrystalline Ge strip waveguides on Si substrate have been proposed by Soref et al, but not experimentally realized. Here, we demonstrated singlemode Ge-on-Si strip waveguide in mid IR with low propagation loss and low bending loss.

3.2 Waveguide design

The idea of this Ge-on-Si strip waveguide was to support singlemode transmission at 5.8 μm in TM polarization. Wider sections at the two ends of the waveguide were important for better coupling. In addition, we needed a 90° bend in each waveguide in order to detect light perpendicularly to the QCL emission axis. Between a wide section and a singlemode section, a taper structure was inserted. These are the criterions for further numerical simulations.

The tool of simulation was commercially available software (CST Microwave Studio), which is based on a finite differential time domain (FDTD) method. Dr. Vincent Paeder (Optics & Photonics Laboratory, EPFL) performed the simulation of the above mentions elements, including waveguides, bends, and tapers.

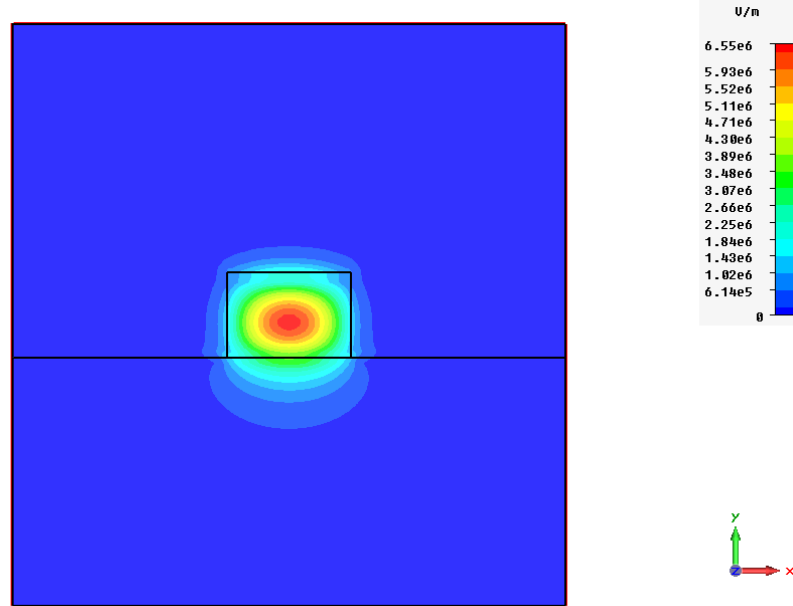


Figure 3.2 Simulated fundamental mode of TM wave at 5.8 μm : The waveguide width was 2.9 μm , and the thickness is 2 μm . Simulation: Vincent Paeder, OPT-EPFL.

Due to the high index-contrast of the Ge core and the air cladding, the waveguide dimension needed to be sufficiently small to support only the fundamental mode. Here the waveguide was designed to be $2.9\text{ }\mu\text{m}$ wide and $2\text{ }\mu\text{m}$ thick. Figure 3.2 shows the simulated mode profile for the rectangle-shaped cross-section of the single mode waveguide.

For better coupling to the laser and to the detector, two $300\text{ }\mu\text{m}$ -long coupling sections were designed at the entrance and the exit of the waveguide. These coupling sections had the same thickness of $2\text{ }\mu\text{m}$, but a larger width of $15\text{ }\mu\text{m}$, which allowed more light to be coupled into the waveguide and the detector. Between a wider coupling section and a narrower single-mode section, a taper section was inserted for the matching of the widths.

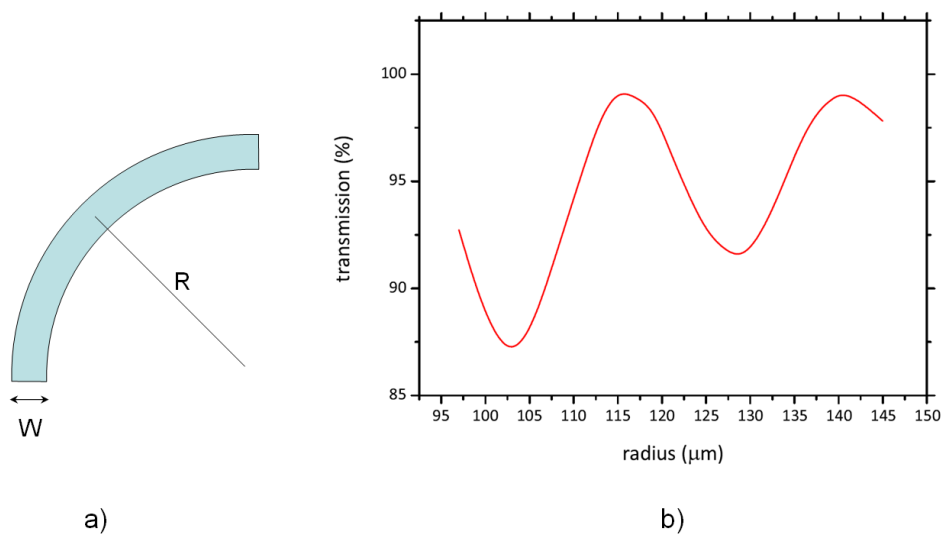


Figure 3.3 Bend Optimization by tuning the radius: a) The right bend had the radius R and the width is W . b) The radius for the maximum transmittance was $115\text{ }\mu\text{m}$. Simulation: Vincent Paeder, OPT-EPFL.

The purpose to add a 90° bend was to reduce the noise of the stray light. When the infrared detector was placed on the axis of the QCL, strong stray light went into the detector and produce large noise. This configuration avoided most of the stray light going through the air and the Si substrate. The bend worked as a spatial filter which allows only the light in the waveguide going to the detector, and hence increased the signal to noise ratio which was important for further experiments.

For a fixed thickness, the bending loss could be optimized by tuning the radius and the width of the bend. For a bend width of $4.36\text{ }\mu\text{m}$, the simulated transmittance of the bend varied with the radius as shown in figure 3.3b. Here we chose the radius of $115\text{ }\mu\text{m}$ and the estimated loss was 2% (0.09dB).

3.3 Waveguide fabrication

The fabrication of Ge-on-Si waveguides started from a mono-crystalline grown Ge layer on a $\langle 100 \rangle$ p-type Si substrate [49]. Between the Ge layer and the substrate, a 10 μm -thick intrinsic Si was added in order to reduce the material absorption from p-type Si substrate for some wavelengths. The 2 μm -thick Ge layer was then grown with reduced pressure chemical vapor deposition (RP-CVD). This high quality mono-crystalline Ge layer ensured a low material absorption during the later development of low-loss Ge-on-Si waveguides.

Due to the large lattice mismatch between Ge and Si (4.2%), a layer of Ge was first grown at 400 °C to obtain a nearly plastically relaxed Ge layer. The growing temperature was then switched to 750 °C for the rest of the 2 μm -thick Ge. In the end of the growth, high temperature cycling (750-890 °C) reduced the total amount of defects. Near the interface with Si, the Ge layer contained some misfit dislocations in the first several-hundred nanometers. These defects contributed a part of the propagation loss of the waveguide.

The process flow of the fabrication is shown in figure 3.4. The Ge layer was grown in the cooperation with CEA-Leti of Minatec Campus in Grenoble, France. A standard photolithography was used to define the geometry of the waveguides. It was then followed by a reactive ion etching (RIE) to transfer the micro structures from the photoresist into the Ge layer. The step in figure 3.4d was to grind and polish the edges of the Si substrate for 1~2 mm, because the following optical characterization required the end facets of the waveguides to be at the edge of the chip.

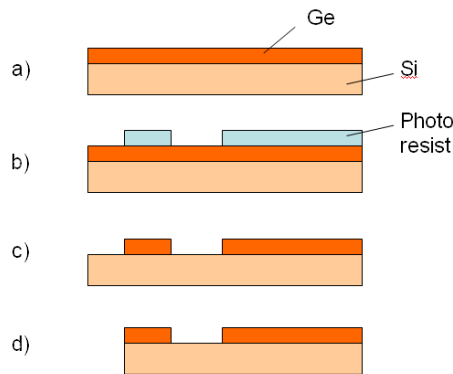


Figure 3.4 Fabrication process flow: a) A 2 μm -thick monocrystalline Ge layer on a Si substrate; b) Standard photolithography defines the waveguide structures; c) Ge layer is patterned with reactive ion etching; d) Grinding and polishing of the edges.

3.3.1 Photolithography

For photolithography, the photoresist is AZ1518 from Clariant Corporation. It is a positive photoresist and suitable as a mask for dry and wet etching. It is sensitive to a wide UV spectrum from 310nm to 440nm, which covers the g, h, and i lines of mercury-vapor lamps. Depending on the speeds and the duration of spin-coating, its thickness varies from 1.4 to 2.5 μm .

Photoresist	AZ1518, Clariant Corp.
Spin coating	3000 rpm, 30 seconds
Soft bake	110 °C hotplate, 60 seconds
Exposure time	6 seconds
Development	AZ351B : water = 1:3 Duration 30-35 seconds
Dry	N2 air blow dry

Table 3.1 Parameters of the photolithography: The waveguide structure was defined in the photoresist which is 2.3 μ m thick.

The parameters of photolithography are listed in table 3.1. At room temperature, the photoresist AZ1518 is spun to the thickness of 2.3 μ m at 3000 rpm for 30 seconds. The exposure was done with a 3-inch mask aligner, MJB3 from Karl Suss KG. During the exposure, the mask is in contact with the photoresist, and the resolution limit is around 1-2 μ m, which depends on the thickness of the photoresist. After exposure, the chip is dipped into the developer and stirred slightly for 30-35 seconds. The developer is AZ351B diluted with de-ionized water by the volume ratio of 1:3 in a room temperature. The development is followed by rinsing in de-ionized water for 30 seconds, and drying with blowing nitrogen gas on the sample.

3.3.2 Pattern transfer with dry plasma etching

Using the photoresist as an etching mask, the waveguide structures were transferred to the Ge layer by RIE, which is one of the most important dry etching methods for micro-structuring. It combines the advantages of methods based on physical bombardment and methods based on chemical reactions [50]. The etching profile is anisotropic and the etch rate is high when compared with other dry etching methods. Because RIE has the nature of chemical reactions, the etch rates are selective to different materials, and can be tuned by choosing suitable gases and etching parameters [51]. With a high selectivity between the mask material and the material to be etched, one can achieve profiles with a high aspect ratio. Table 3.2 lists the parameters of the RIE process for etching Ge on Si substrates in our experiments. The typical etch rate of Ge was in the range of 150-200 nm per minute.

Equipment	Plassys MG200
Gas and flow rates	Oxygen=0.8sccm, CF4=40sccm
Pressure	6Pa
Power and bias voltage	45W, 420V
Etch rate	150-200 nm/min
End point detection	Laser reflectivity method

Table 3.2 Parameters of RIE for etching the Ge layer: The waveguide microstructures are transferred into the Ge layer with RIE based on CF4 and oxygen. The etching duration is controlled by monitoring the reflectivity of the sample surface.

Here, the etching is investigated with two materials, Ge and Si, and two reactive gases, CF4 (tetrafluoromethane) and oxygen. The instrument was Plassys-MG200 which has the maximum 100W RF (radio frequency) output intensity at the frequency of 13.56MHz. Figure 3.5 is an image of the etching system. The flow rates of gases can be controlled between 0 and 50 sccm (standard cubic centimeters per minute) while the pressure of the specimen chamber can be controlled from 1 to several tens Pa. It is equipped with a reflectivity monitor for the end-point detection. The maximum sample size for it is a 4-inch wafer.



Figure 3.5 Image of Plassys MG200 for reactive ion etching: Ge dry etching is performed in the RF plasma of CF4 and O2.

For a Ge-on-Si strip waveguide, the Ge outside the masking area was removed by RIE. To stop etching at the interface of Ge and Si, it is desirable to have a higher etch-rate for Ge and a lower rate for Si, which means a higher selectivity of Ge over Si. In fluorine-based plasma, the ratio of etch-rates of Ge and Si can be as high as 30 while the chamber pressure is as high as 33 Pa [51]. In these high pressure conditions, the etching was dominated by the chemical reactions rather than physical bombardment, and therefore had a higher selectivity of Ge over Si. However, higher chamber pressure also lead to an

isotropic etching profile, which had a larger undercut and limited the smallest feature size of the microstructures.

Figure 3.6 shows the SEM (scanning electron microscope) images of the etching tests on Ge and Si material with plasma of CF₄ and oxygen at the RF power of 45W with two different specimen chamber pressures of 13 and 6 Pa. The flow rates were 40 sccm for CF₄ and 0.8 sccm for oxygen, and the etching duration was 10 minutes. In these tests, Ge was etched faster than Si and the Ge/Si selectivity were 3.28 and 2.39 for the pressures of 13 Pa and 6 Pa respectively. While the higher pressure gave a larger Ge/Si selectivity, it also produced an isotropic etching shape and an undercut of approximately 1.7 μm for Ge. The undercut effect can limit the smallest feature size for this etching recipe and can hinder the development of some devices which need small and precise etching results. For example, directional couplers based on the evanescent coupling in general need a very narrow spacing between two strip waveguides [52].

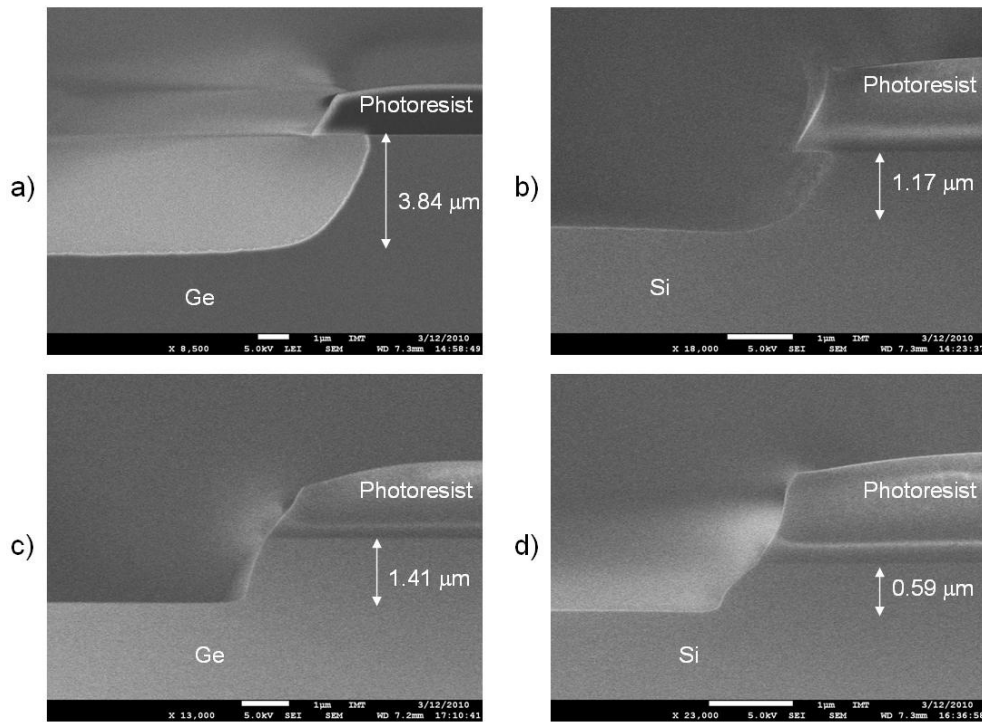


Figure 3.6 SEM images of etching tests on Ge and Si with different pressures in the specimen chamber: a) & b) Ge and Si are etched at 13 pascal and the Ge/Si selectivity is 3.28 while the etching profile is isotropic with a large under cut; c) & d) Ge and Si are etched at 6 pascal and the Ge/Si selectivity is 2.39.

The top surface quality was influenced with higher chamber pressure. As shown in figure 3.7, Ge surface became rougher when the chamber pressure went higher. This was due to the initial point defects and lines on the top surface became larger and wider after etching. This phenomenon might be originated

from the different etching rates for different crystalline orientation of Ge, when chemical reactions dominate the etching process.

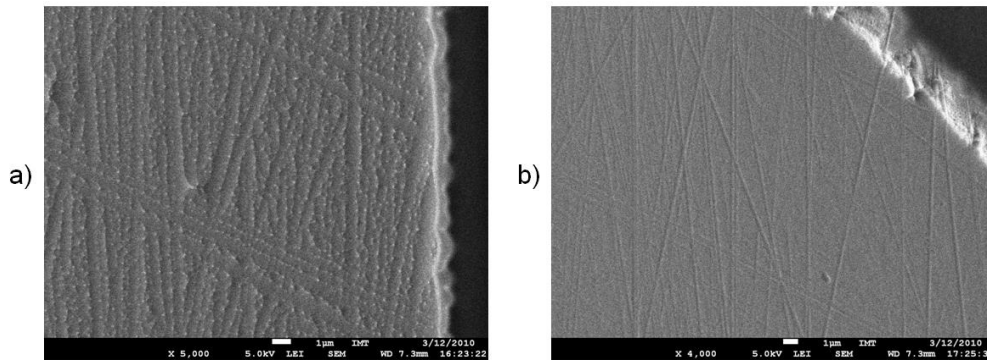


Figure 3.7 Ge surface after etching with different chamber pressure: a) Ge etching at 13 Pa, b) Ge etching at 6 Pa; After etching with CF₄ and oxygen plasma, the top surface of Ge became rough by following the original defects and lines on the Ge. This phenomenon became more serious in a higher pressure of the specimen chamber.

The etch rate depended on various parameters, including materials to be etched, reactive gas compositions and flow rates, RF power intensity, the chamber pressure, the substrate temperature, the sample size, and also the aspect ratio of microstructures. For etching Ge with RIE of CF₄ and oxygen, the typical etch rate was in the range of 50-500nm per minute. Due to the large range of the etch rate, depth control became an important issue for having a repeatable etching result.

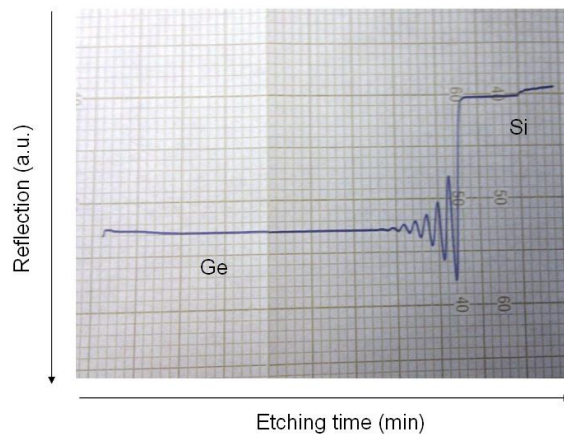


Figure 3.8 Typical curve of the laser reflection during the etching of Ge on Si: The reflection of Si is lower than Ge. (Lower reflection is higher in the curve.) During the transition from Ge to Si, interference fringes of the thin Ge film can be observed.

In the case of Ge-on-Si, the Si substrate actually became the etching stop for the etching of Ge, where the Ge/Si selectivity is approximately 2~3. In addition, we monitored the reflectivity of the sample surface and determined the

end-point of etching. A visible laser was pointed to the sample top surface and a photo detector measured the intensity of the reflected light. Because the reflectivity of Si was about 25% lower than Ge, we could observe a drop of the laser reflection when Ge was removed and Si became the top surface of the sample. Figure 3.8 is a typical curve of the reflectivity against time during the etching. In the transition of the top surface from Ge to Si, we could observe the interference fringes of the changing thickness of the Ge layer, while the Ge layer was thin and became partially transparent to visible light. In the end of the transition, the etch process continued for 1 minute more to ensure the completion of Ge etching on the whole chip.

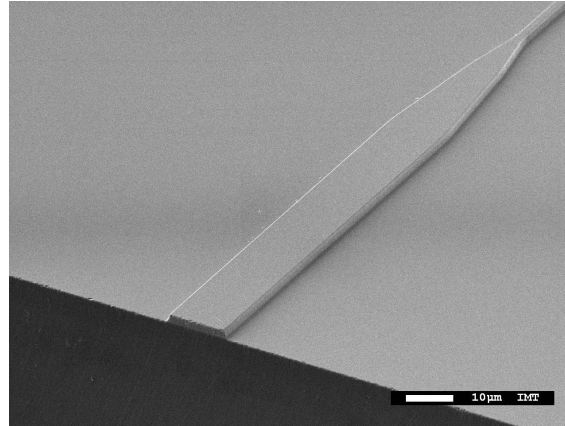


Figure 3.9 SEM image of the coupling section: At the beginning and the end of the waveguide, a 15 μm -wide section was designed to have better coupling to the laser and the detector. A taper connected the wider and the narrower sections of the waveguide. This sample had been polished at the edge to the coupling section.

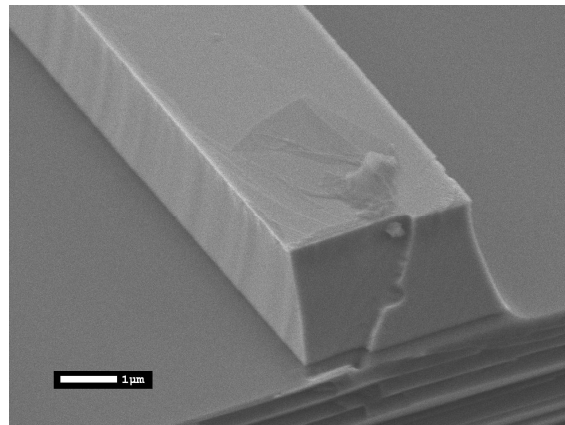


Figure 3.10 SEM image of a Ge waveguide on Si: In the narrower section of the waveguides, the width was 2.9 μm , and the thickness was 2 μm . It was designed for single mode transmission for TM polarization at the wavelength of 5.8 μm .

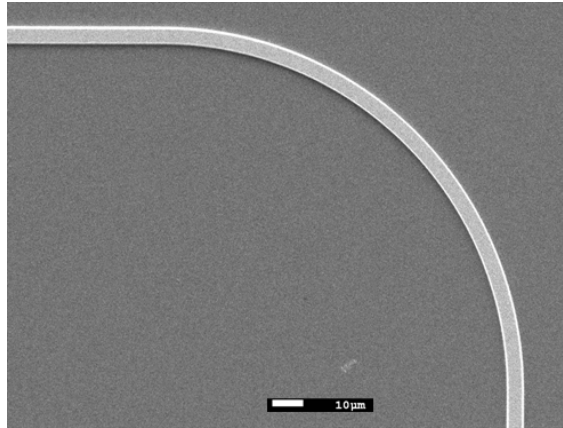


Figure 3.11 SEM image of a 90° bend of a radius 115 μm : The purpose of the bend was to avoid doing measurement on the emission axis of the laser. Therefore one can reduce the stray light going through the free space and the Si substrate. The bending loss was measured to be 0.12dB in a later experiment in section 3.6.

3.3.3 Edge polishment

After RIE, the two ends of the waveguide were 1~2 mm away from the edge of the substrate. However, the waveguide was going to be coupled to the QCL and the detector with the methods of butt-coupling and end-fire. Both the two methods require the facets of waveguides to be at the edges of the substrate in order to have better coupling efficiency. Therefore we grinded and polished the edges until the waveguide facets.

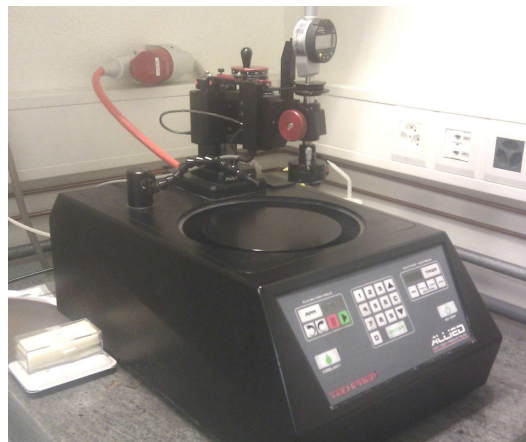


Figure 3.12 Image of the grinding/polishing machine: It is TechPrep from Allied High Tech Product Inc., and has 8-inch platen with exchangeable lapping films.

As shown in figure 3.12, the equipment used here was a grinding and polishing system, TechPrep from Allied High Tech Products Inc., which has an 8-inch rotating platen with exchangeable diamond lapping films. The substrate was mounted perpendicularly to the waveguide coupling section with a thermal plastic adhesive, Crystalbond 509 from Ted Pella. Inc. The sample was grinded to

the desired depth with a lapping film with diamond particle size of 30 μm , and then polished with several films of smaller diamond particles until the size of 0.5 μm .

Cleaving along the crystal cleavages is often used to produce nearly perfect surface quality in applications like semiconductor lasers. In this study, we used the polishing method because it was easier to control the position of the edges with an acceptable surface quality in the mid IR.

3.4 Waveguide coupling

For optical characterization, the waveguide was coupled with a QCL from one facet and with a mid IR detector from the other facet. The coupling was achieved with two methods, which were end-fire coupling with lenses or mirrors and butt-coupling without optical elements. Butt coupling provided higher efficiency than end-fire coupling but it was also more sensitive to misalignment and mechanical vibrations.

3.4.1 End-fire method

Figure 3.13 shows the scheme of the setup for optical measurement. One end facet of the waveguide was coupled to the QCL with two ZnSe (Zinc Selenide) lenses. These biconvex lenses have the diameter of 25 mm and a focal length of 25mm. Since the refractive index of ZnSe is near 2.4, antireflection multilayer coating was used on both sides of the lenses to reduce the Fresnel loss. Compared with off-axis parabolic mirrors, these lenses facilitated the alignment procedures. Over the spectral range from 3 to 12 μm , the transmittance was increased from $\sim 70\%$ to more than 90%. These lenses and the QCL were aligned and mounted together on a 3-dimensional translation stage, which has precision of 10 μm over a range of 25mm. The focused laser spot could be moved around the end facet of the waveguide to find a best alignment position.

The detector was a liquid-nitrogen cooled photoconductive MCT (mercury cadmium telluride) with a ZnSe window. The element size is $0.25 \times 0.25 \text{ mm}^2$ and has a high sensitivity over a broad spectral band from 2 to 16.6 μm . For coupling of the detector with one facet of the waveguide, two gold coated 90° off-axis parabolic mirrors were used to image the waveguide facet onto the active element of the detector. These mirrors are 50.8 mm in diameter and the effective focal length is 50.8 mm. The use of mirrors eliminated the chromatic aberration of lenses. The MCT detector and the two parabolic mirrors were aligned and mounted together on a 3-dimensional translation stage, which allowed scanning of the focal spot in the vicinity of the waveguide end facet to find an optimum alignment position. The translation stage has a precision of 10 μm over a range of 25mm in the 3 axes.

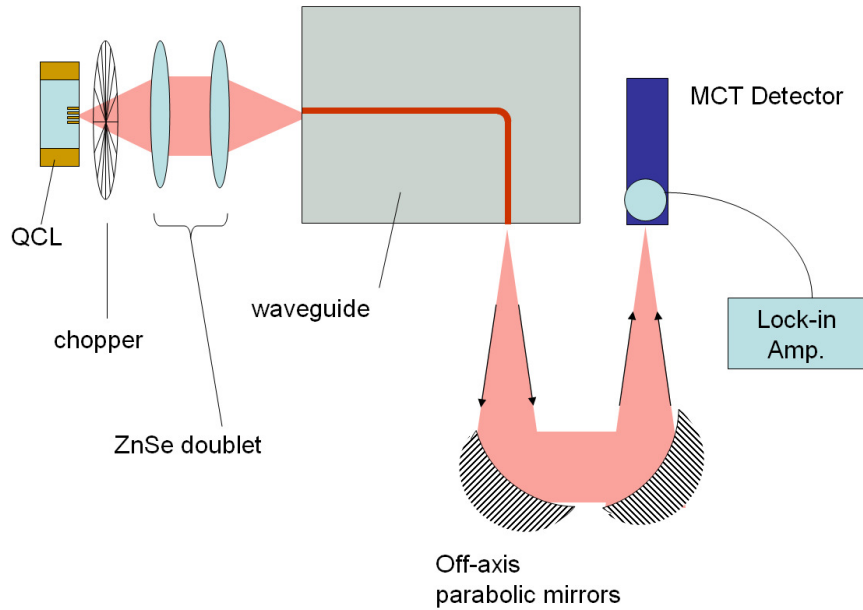


Figure 3.13 Setup for optical characterization: The waveguide was coupled to the QCL with two ZnSe lenses from one facet. The other facet was imaged to the MCT detector with two off-axis parabolic mirrors. The chopper and the Lock-in amplifier allowed the measurement with a correlation technique and a lower noise.

The light source was a QCL (quantum cascade laser) emitting at $5.8\text{ }\mu\text{m}$. It was a DFB (distributed feedback) laser and provided a very sharp spectrum when it was driven in a CW (continuous wave) mode. The QCL was working at $-25\text{ }^{\circ}\text{C}$ and sat in a hermetic housing, which was LLH-100 from Alps Lasers SA. The light emission was through a ZnSe window with anti-reflection coatings for the wavelength of $3.5\text{--}12\text{ }\mu\text{m}$. In the laser housing, a NTC (negative temperature coefficient) thermistor and a Peltier thermo-electric element controlled the temperature of the laser, which was important for maintaining the laser wavelength and a stable output power. Here the QCL was driven at 7.5V DC with the current of 225mA , while the laser output power was 2mW . Due to the fact that most injected electric power was converted into heat, water cooling in the base plate of LLH-100 was necessary to keep a sufficient thermal dissipation.

In front of the output window of the laser housing, a rotating chopper mechanically modulated the light intensity at the frequency of 1025 Hz with the duty cycle of 50% . The correlation technique using a lock-in amplifier had been used to improve the signal to noise ratio. The correlation technique was especially important for detection of light in the mid-IR, because thermal radiation of matters in a room temperature has the spectrum with the peak value in the mid-IR. While we used the MCT detector which responds to a wide spectrum from 2 to $16.6\text{ }\mu\text{m}$, moving objects (particularly human bodies) in its viewing cone became the noise sources.

After the two ZnSe lenses, the light was coupled into the waveguide. At the same time, a part of the laser went through the free space above the sample or through the Si substrate under the Ge waveguide, and became the undesired stray

light. Because it was also modulated by the chopper, it became a large noise source. The 90° bend allowed the measurement from the side and avoided the strong stray light on the emission axis of the QCL. Here, the bend had the function as a spatial filter, which allowed only the light propagating in the waveguide going into the detector, since most of the stray light was on the emission axis of the QCL.

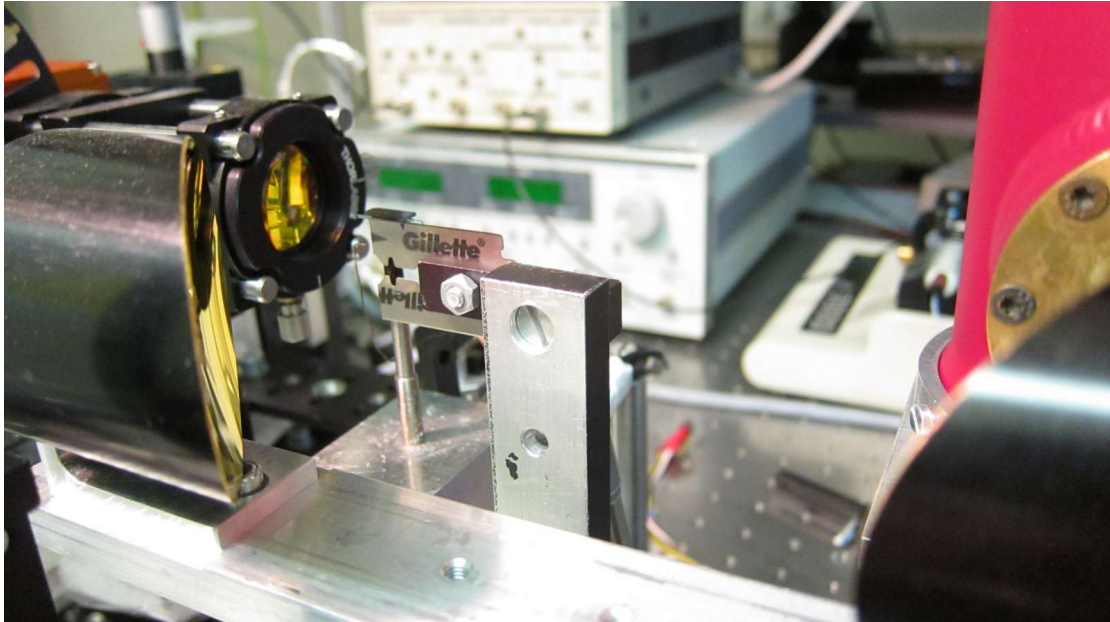


Figure 3.14 Photo image of the setup for optical measurement: A razor blade in front of the sample reduced stray light from the substrate and from the free space.

The output port of the QCL had the width of $15\text{ }\mu\text{m}$ and the thickness of $2\text{ }\mu\text{m}$. Because of the small dimensions of the QCL, the waveguide end facets, and the MCT detector element, the optimum coupling needed a precise alignment in the order of a wavelength. By scanning of the laser spot over the neighborhood of the waveguide facet, one can find a best aligned position which gives the maximum transmission measured by the detector. For a $2.9\text{ }\mu\text{m}$ -wide, $2\text{ }\mu\text{m}$ -thick, and 10 mm -long waveguide, at the maximum point the total transmission was approximately 3%, which included the coupling loss, the Fresnel reflection, and the propagation loss. Figure 3.14 shows the picture of the setup for the end-fire coupling. To avoid possible noise coming from the substrate, a razor blade was placed closely in front of the sample edge of the waveguide output with a gap of $100\text{ }\mu\text{m}$. With a 3-dimensional translation stage, the knife edge was positioned about $100\text{ }\mu\text{m}$ below the output facet of the waveguide. This allowed light from the waveguide going to the detector and prevented possible light from the Si substrate, which is also transparent at the wavelength of $5.8\text{ }\mu\text{m}$.

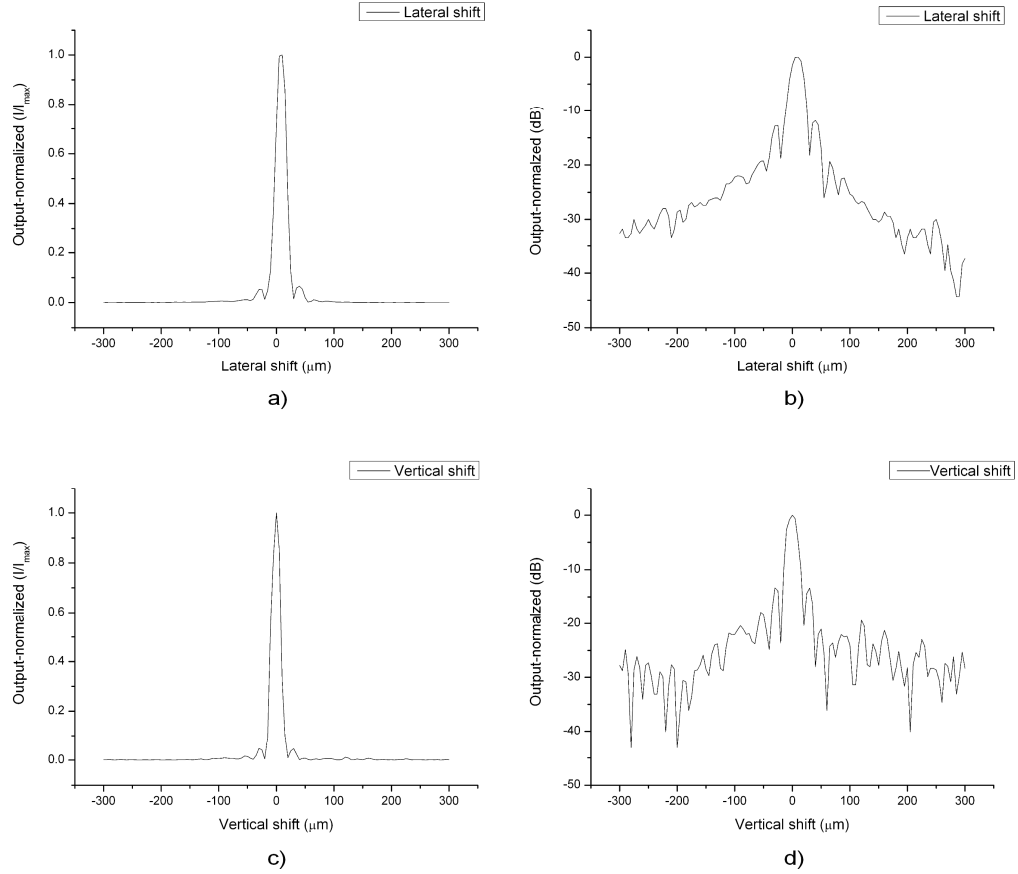


Figure 3.15 Waveguide output intensity when the QCL was shifted from the optimum alignment position: a) & b) The QCL shifted laterally and the normalized output from the waveguide is plotted in a linear scale and a logarithm scale. The signal to noise ratio was about 30dB when considering the noise floor is around $\pm 300 \mu\text{m}$. c) & d) The QCL was shifted vertically. The output of the waveguide is more sensitive to the vertical shift.

The waveguide output intensity reached the maximum value at the best coupling position which was the point where the focused laser beam had the largest overlap with the waveguide mode. When we shifted the focus spot of the laser from this position, the transmitted light intensity dropped rapidly. Figure 3.15 shows the normalized waveguide output intensity while the laser spot was shifted for 300 μm laterally and vertically. In figure 3.16 a) & c), the output intensity was in linear scale. Beside the central focus spot, several side lobes were due to the limited aperture size of the lenses. Since the waveguide facet was 15 μm wide and 2 μm thick, the measured central lobe was wider in the lateral direction than in the vertical direction for approximately 10 μm . In figure 3.16 b) & d), the output intensity was plotted in logarithm scale. When we moved the laser spot laterally away from the waveguide facet for 300 μm , the detector reading dropped to a low level, and we could determine the signal to noise ratio to about 30dB.

3.4.2 Butt coupling method

The other way of coupling we tested here was the butt-coupling between the QCL and the waveguides. This method is commonly used in the visible and near infrared range for light wave transfer between two fibers, a fiber and a waveguide, a fiber and a semiconductor laser, or between a waveguide and a semiconductor laser. It is simply to put the facets of two optical devices as close as possible until they are in contact. Without additional lenses or prisms, this method is simple and practical. For the coupling between a fiber and a semiconductor laser, the mode shape of the laser is usually elliptic and does not match well to the fiber modes. However, when the two connected devices have similar mode shapes of electromagnetic waves, the theoretical coupling efficiency can be nearly 100% [53]. In our case of coupling of the waveguide and the QCL, both of them had similar elliptic shapes of the modes. They had similar dimensions for the waveguide facet and the laser emission facet. The simulated coupling efficiency was approximately 70-80% when they were in contact by the facets. To achieve a high efficiency with the butt-coupling method, it was critical to build and maintain a good alignment with the precision in the order of a wavelength.

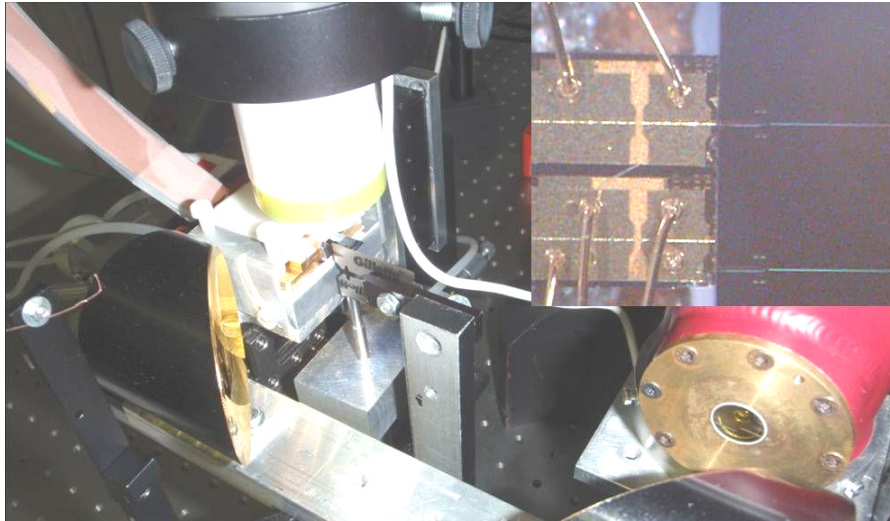


Figure 3.16 Photo image of the setup for butt-coupling of the QCL and the waveguide: The room-temperature QCL was butt coupled to a Ge-on-Si waveguide. The inset was a microscope image which shows that the laser was in contact with the waveguide.

Because most QCLs need a low working temperature in the range from -30°C to 0°C, they often stay in an air-tight housing to prevent the condensation of water vapor from the air. These QCLs emit laser through a window, which prohibits the butt-coupling to the waveguide. Therefore, a room-temperature QCL is necessary for this coupling method. Here we used with a QCL working at 20°C (from Quantum Optoelectronics group, ETHZ), which emitted light at 4.3 μm and was driven by pulses of 17.5 volt with the frequency of 90K Hz and the width of 200 ns. As shown in figure 3.16, the QCL was mounted on a stage

without housing, and there was no need of refocusing lenses between the laser and the waveguide. Here we removed the rotating chopper in front of the laser since the QCL was in the pulse-driving mode and the pulse frequency provided the reference signal for the lock-in amplifier. With the help of a microscope, one can easily align the laser to the waveguide facet, as shown in the inset of figure 3.16.

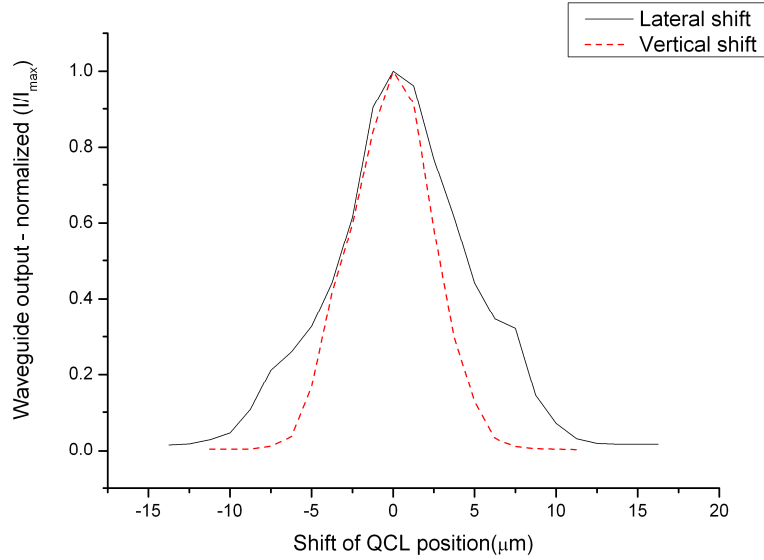


Figure 3.17 Waveguide output intensity for butt-coupling with the shift of QCL laterally and vertically from the best coupling point: The coupling was more sensitive to the misalignment in the vertical direction.

To assess the influence of misalignment of the QCL for butt-coupling, we shifted the QCL from the optimum alignment position and recorded the waveguide output intensity. As shown in figure 3.17, the coupling was sensitive to both lateral and vertical shifts, especially in the vertical direction since the thicknesses of the waveguide and the laser were around 2 μm only. As compared with the end-fire method we have previously tested, it was approximately 3 times more sensitive to the misalignment and more susceptible to mechanical vibrations in the system.

Figure 3.18 shows the effect of increasing the gap between the QCL and the waveguide where 0 μm is the point of the maximum coupling. When we move the laser and enlarge the gap, there was not only the quadratic drop of the waveguide output intensity, but also several interference fringes at the beginning of the shift, corresponding to the Fabry-Perot resonance of the varied air gap between the laser and the waveguide. Due to the high refractive index of the materials for the QCL and the waveguide, the reflections at their interfaces with the air were high, and therefore the modulation depth of the fringes could be more than 50% of the intensity. These fringes can become an issue for the stability and the efficiency of the coupling, because they were very sensitive to the thickness of the air gap and needed a sub-micron precision of alignment. In

the visible and near infrared wavelength range, they are often suppressed by using an index-matching liquid which has a similar refractive index as the materials for the waveguide and the laser [53].

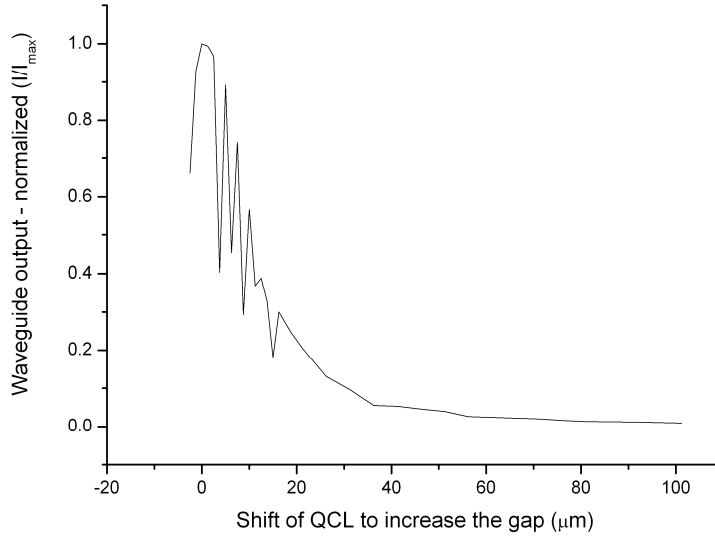


Figure 3.18 Waveguide output intensity with the gap in the QCL and the waveguide: The signal dropped with the distance while the air gap formed a cavity and produced the interference fringes in the beginning of the curve.

3.5 Propagation loss measurement

One important parameter for an optical waveguide is the propagation loss, which means the rate of energy attenuation when light waves travel in the waveguides for a unit length. This loss is usually attributed to the scattering of light at the rough surfaces of the waveguide, and the scattering inside the waveguide due to imperfections of the materials. In the spectrum of mid-IR, the absorption from the materials of the waveguide core and claddings becomes important.

Cut-back method is the simplest way to measure the propagation loss of an optical waveguide or a fiber [53]. The total transmission is measured when the waveguide is shortened by one or several cuts. By assuming the coupling efficiency keeps the same before and after each cut, one can calculate the propagation loss α as

$$\alpha = \frac{\log(I_1/I_0)}{L} \quad (eq.3.1)$$

where I_0 and I_1 are the waveguide total transmission (or output intensity) before and after the cut respectively. L is the difference of the waveguide length. This method is simple and suitable for optical fibers since the process of cutting usually do not disturb the coupling of fibers when the fibers are long. A planar

waveguide or a strip waveguide, however, often need a re-alignment to the source after cutting, which makes the measurement dependent on the alignment repeatability.

3.5.1 Fabry-Perot resonance method

In this study, we used a method utilizing the Fabry-Perot resonance fringes of the cavity formed by the waveguide itself [54]. When light waves in the waveguide traveled to the two end facets, both transmission and reflection happen at the interfaces of the air and the waveguide. The reflected light waves bounced back and forth between the two end facets and interfered with each other. The waveguide behaved as a resonator and the transmitted light intensity had the interference fringes. These Fabry-Perot resonance fringes were determined by parameters including the reflectivity at the end facets and the propagation loss of the waveguide. By measuring the modulation depths of these fringes, we could know the propagation loss of each waveguide. This is a non-destructive method. In addition, this method is insensitive to the coupling efficiency because the propagation loss is determined from the modulation depth of the fringes but not the total transmission.

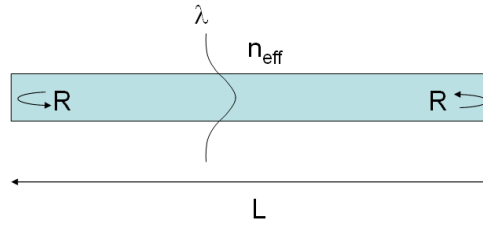


Figure 3.19 Illustration for a waveguide as a Fabry-Perot resonator

In the Fabry-Perot resonator formed by the waveguide, as shown in figure 3.19, a reflected light wave traveling back and forth to the same point has a phase difference δ , which is determined by the waveguide length L , the wavelength λ of the light source, and the effective index n_{eff} of the propagation mode, by the following relation.

$$\delta = \frac{2\pi}{\lambda} \cdot 2L \cdot n_{eff} \quad (eq.3.2)$$

Consider a coherent light source, when there is no loss during the propagation and reflections in the waveguide, the transmitted light intensity I is given by

$$I = I_0 \frac{(1 - R)^2}{1 - 2R\cos\delta + R^2} \quad (eq.3.3)$$

where I_0 is the intensity before the waveguide, R is the reflectivity at the end facets of the waveguide. Here the coupling coefficient is assumed to be unity for

the convenience of analysis. Thus the transmittance I/I_0 is determined only by R and δ . Figure 3.20 shows the calculated transmittance against the phase difference. When the phase difference equals to integer multiples of 2π , the reflected waves are in phase with each other and the transmittance reaches maximum, which can be 100% when there is no loss. When the end facets have a high reflectivity (e.g. $R=0.9$), it behaves as a good resonator with sharp peaks at each phase-matching positions. For a waveguide without additional coating at the end facets, the reflectivity is normally smaller than 0.5, and the Fabry-Perot fringes become closer to a sinusoidal shape. The peaks are less sharp and the resonator allows more transmission of light even when the phase matching condition is not satisfied. For example, the dashed curve in figure 3.20 is the calculated transmittance when the reflectivity R is 0.342.

When we consider a waveguide with a propagation loss α , the transmitted light intensity I is given by

$$I = I_0 \frac{(1 - R)^2 \cdot 10^{-\alpha L}}{1 - 2R \cos \delta \cdot 10^{-\alpha L} + R^2 \cdot 10^{-2\alpha L}} \quad (eq.3.4)$$

while the reflection at the two end facets is assumed to have no loss. The transmittance of the waveguide is plotted as the solid curve in figure 3.21, in which the propagation loss is 3dB after the light waves travel for the length of L in the waveguide. In the system with losses, the maximum transmittance is no longer 100% at the phase matching positions.

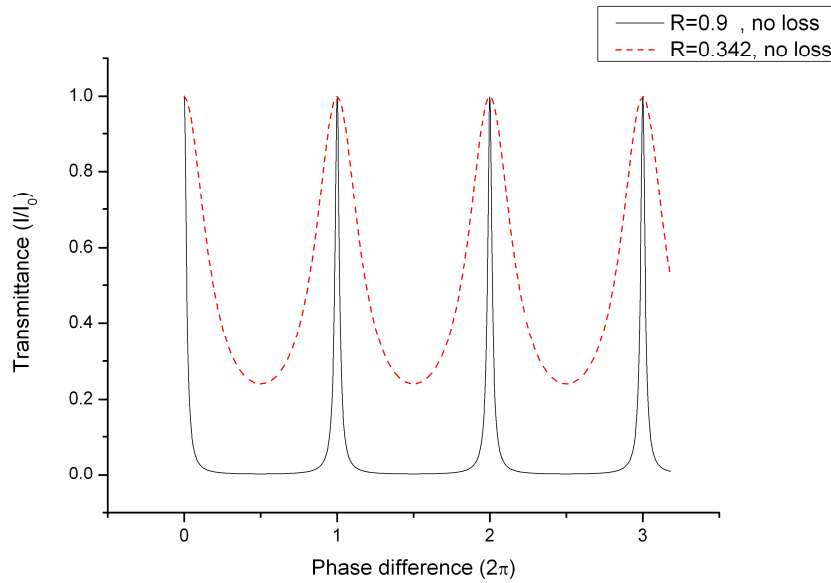


Figure 3.20 Calculated transmittance against the phase difference: When there is no loss, the maximum transmittance can be 100%. The dashed curve is the Fabry-Perot fringe while the reflectivity R is 0.342.

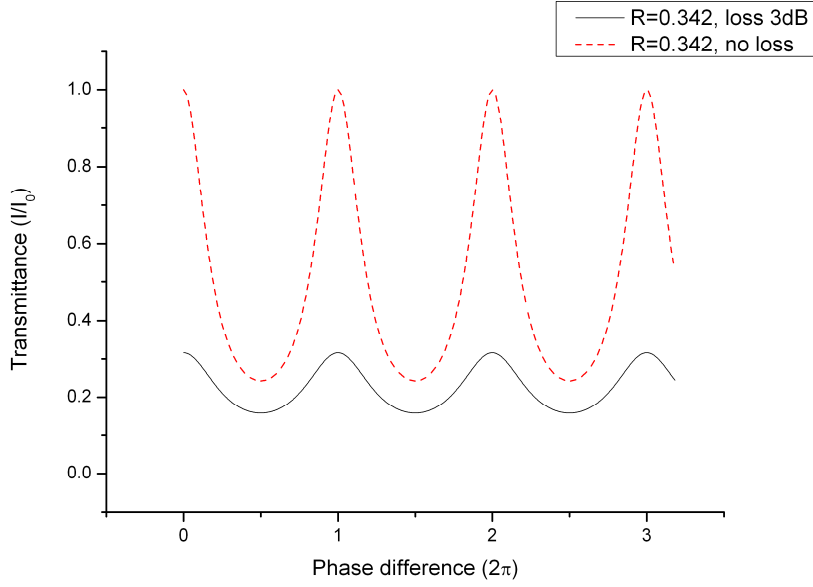


Figure 3.21 Calculated transmittance with different losses: The solid curve is the fringes of waveguide with loss of 3dB after the propagation of the length L .

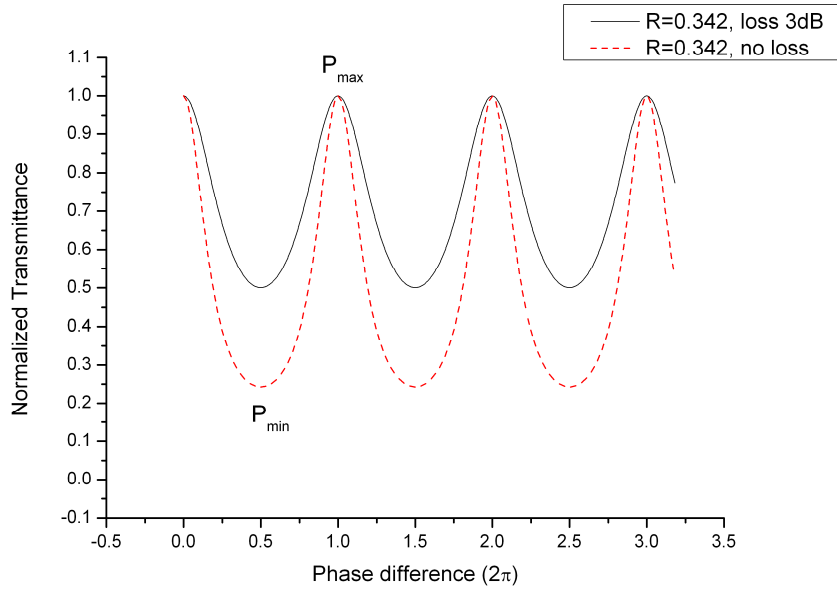


Figure 3.22 Normalized transmittance for curves with and without losses: The solid curve is calculated from waveguide with the loss of 3dB and P_{min}/P_{max} is larger.

When we normalized the two curves in figure 3.21 by dividing them with the maximum value of each curve, we could compare the Fabry-Perot resonance fringes of waveguides with and without losses in figure 3.22. The two curves were calculated from the same reflectivity $R=0.342$, but the dashed curve had no loss and the solid one had a propagation loss of 3 dB over the waveguide length L .

For the waveguide without loss, the resonant peaks are sharper and the modulation depth is larger, which means P_{min}/P_{max} is smaller.

P_{max} is the output intensity at the maximum where $\cos(\delta)$ is 1, and P_{min} is at the minimum where $\cos(\delta)$ is -1. Therefore, P_{min}/P_{max} can be written as

$$\frac{P_{min}}{P_{max}} = \frac{1 - 2R \cdot 10^{-\alpha L} + R^2 \cdot 10^{-2\alpha L}}{1 + 2R \cdot 10^{-\alpha L} + R^2 \cdot 10^{-2\alpha L}} \quad (eq.3.5)$$

, the term of propagation loss, αL can then be obtained from

$$\alpha L = \log\left(R \frac{1 + \sqrt{P_{min}/P_{max}}}{1 - \sqrt{P_{min}/P_{max}}}\right) \quad (eq.3.6)$$

From this equation, one can determine the propagation loss α of a waveguide with the length L and the reflectivity R of the end facets, by measuring the ratio of P_{min} and P_{max} from the Fabry-Perot fringes.

Since this method is based on the shape of the fringes which is determined by R and α , a reliable reflectivity R is necessary for an accurate measurement of α . In general, R is given by numerical simulation or approximate calculations [55]. In our case, the reflectivity of the end facets of the Ge waveguides is simulated by FDTD (finite-difference time-domain) method to be 0.342 for a 15 μm -wide and 2 μm -thick Ge facet on a Si substrate in the air environment. For a facet which is perpendicular to the waveguide, it can also be calculated from

$$R = \left(\frac{1 - n_{eff}}{1 + n_{eff}}\right)^2 \quad (eq.3.7)$$

where 1 is the refractive index in the air and n_{eff} is the effective refractive index of the waveguide mode.

Based on the Fabry-Perot resonance, the propagation loss measurement has a better accuracy when the waveguide has high facet reflectivity and low total transmission loss [54].

3.5.2 Measurement results

To obtain experimentally the Fabry-Perot fringes from the waveguide of interest, one needs to vary the phase difference δ and measure the corresponding transmitted light intensity. One of the two ways to do so is to change the wavelength of the incident light. This normally needs a tunable laser emitting light in a spectral range which is large enough to read one maximum and one minimum of the output intensity. The other way is to vary the optical path $2n_{eff}L$ of the waveguide.

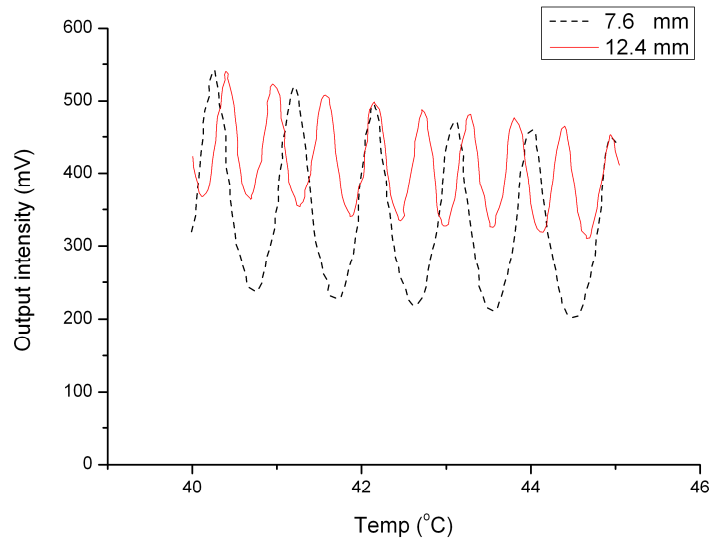


Figure 3.23 Measured Fabry-Perot fringes of two waveguide with different lengths: The longer waveguide showed a faster modulation with temperature.

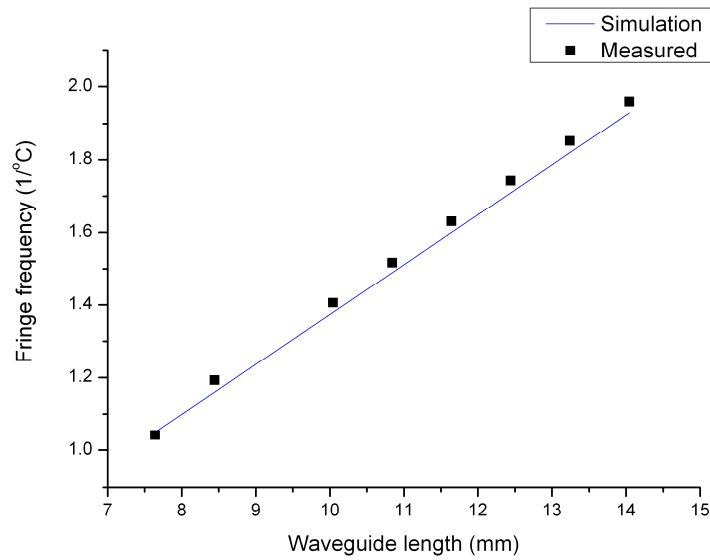


Figure 3.24 Modulation frequency with temperature: The measurement was in a good agreement with the simulation result.

Here we changed the optical path by heating up and cooling down the material of the waveguide. With the setup of end-fire configuration, we added an additional tungsten coil close to the waveguide to control the temperature. When the temperature of Ge became higher, the refractive index increased [56] and the transmittance was modulated by the varying optical path. For waveguides with different lengths, the phase difference varied with the temperature by different speeds. Figure 3.23 shows the measurement result from two waveguides of

different lengths. The longer one had a faster modulation with the temperature, and also a smaller modulation depth due to a larger total loss in the full length of the waveguide. The average value of transmission decreased slowly with the temperature because of the misalignment induced by thermal expansions of the mechanical elements in the setup.

The modulation frequencies with temperature can be simulated by taking into account the thermal optical coefficient $dn/dt=0.000416 \text{ K}^{-1}$, and the linear thermal expansion coefficient $\alpha_L=6\text{E-}6 \text{ K}^{-1}$ of Ge. As shown in figure 3.24, the calculated frequencies were in good agreement with the measurement results, where waveguides of 8 different lengths were measured.

In the method of Fabry-Perot resonance, a larger modulation depth represented a lower propagation loss when the waveguide lengths and the reflectivity were the same. Here the lowest loss we achieved was 2.4 dB/cm, where the P_{min}/P_{max} was 0.51 and the waveguide length was 13.24 mm. The waveguide was 2- μm thick and 2.9- μm wide. The measured Fabry-Perot fringes were shown in figure 3.25, where P_{min} was the average of P_{min1} and P_{min2} in order to reduce the effect of decreasing average intensity when we calculated the loss. When we took into account the bending loss in the waveguide, the propagation loss was actually smaller than 2.4 dB/cm. Next section presents that the bending loss was measured to be 0.12 dB for a 90° bend with a radius of 115 μm .

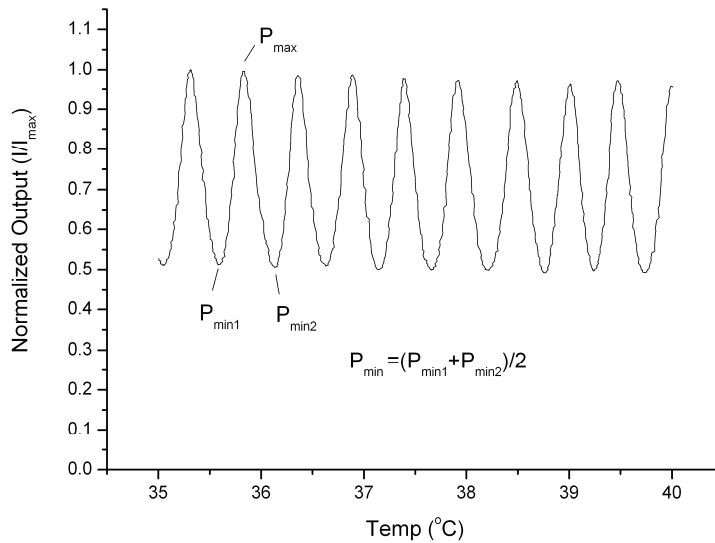


Figure 3.25 The measured Fabry-Perot fringes of the waveguide with the lowest propagation loss we achieved: The propagation loss was smaller than 2.4dB/cm when we took into account the bending loss in the waveguide.

The measurement result of the Fabry-Perot resonance method was reconfirmed by a length-variant method which compared the output intensity of waveguides with different lengths. Like the cut-back measurement, this method assumed that the coupling efficiency was the same in each time for each

waveguide. These waveguides were first measured with Fabry-Perot method and the propagation losses were in the range from 2.9 to 4 dB/cm, while the average value is 3.5 dB/cm as shown in figure 3.26. The transmission of each waveguide was then compared against the waveguide length. As plotted in figure 3.27, the slope of the linear fit was 3.6 dB/cm, which had a good agreement with the result of the Fabry-Perot resonance method.

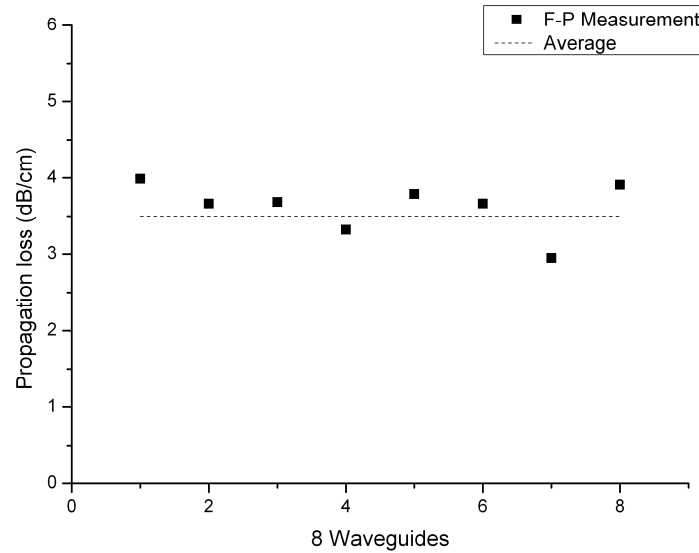


Figure 3.26 Propagation loss of 8 waveguides with Fabry-Perot method: The 8 waveguides were fabricated on the same substrate and had different lengths from each other. The average value of their propagation losses was 3.5 dB/cm.

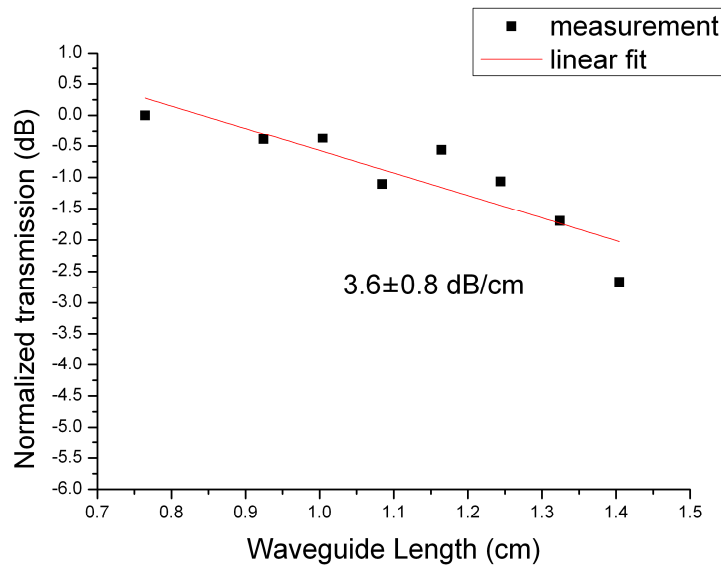


Figure 3.27 Transmission of the 8 waveguides of different lengths: The slope of the linear fit was 3.6 dB/cm and showed a good agreement with the measurement result from the Fabry-Perot resonance method shown in figure 3.26.

Intrinsic crystal Ge and Si have low absorption at $5.8\ \mu\text{m}$ which was the wavelength of the QCL we used for measurement. The expected propagation loss was $< 1\text{dB/cm}$ [33]. Here the propagation loss could be partly attributed to the roughness of the side walls of the waveguides. Besides, the first several-hundred nanometers of Ge contain misfit dislocations and contributed a part of the propagation loss [49].

3.6 Bending loss measurement

The 90° bend in each waveguide had the advantage to reduce the undesired stray light. However, it also added a bending loss to each measurement. The bending loss is very much related to the radius of the bend and the wavelength. From the previous simulation result, the bending loss should be near 2% (0.09 dB) for the fundamental mode of TM polarization at the wavelength of $5.8\ \mu\text{m}$, while the bend radius was $115\ \mu\text{m}$.

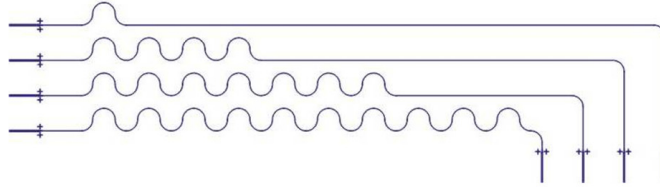


Figure 3.28 Waveguide design for the measurement of bending loss: The 4 designs had the same total waveguide length but different numbers of bends.

To measure the bending loss, we compared the transmission loss of waveguides with different numbers of bend. Here the transmission loss included the total propagation loss and the total bending loss. As shown in figure 3.28, the 4 designs had the same total waveguide length, but the numbers of 90° bends for each design were 5, 17, 29, and 41 separately. The transmission loss of each waveguide was measured with the Fabry-Perot resonance method described in section 3.5. Figure 3.29 shows the result from 16 waveguides of the 4 designs. The slope of the linear fit gave the bending loss of 0.12 dB for a 90° bend with the radius of $115\ \mu\text{m}$.

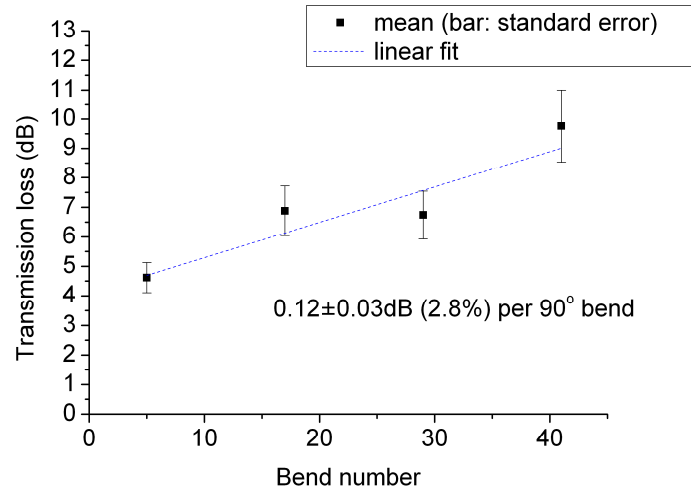


Figure 3.29 The measurement of bending loss: Transmission loss of 16 waveguides with the same waveguide length but 4 different numbers of bends were measured.

Chapter 4

Cocaine detection in liquids with a Ge-on-Si strip waveguide

Mid infrared spectroscopy has been extensively used for detection and identification of chemicals. In the solid and liquid phases, ATR-FTIR (Attenuated Total Reflection Fourier Transform Infrared Spectroscopy) exhibits advantages over transmissive FTIR because of its high reproducibility and simple steps of sample preparation [16,17]. In the evanescent field near the interface of the sample and the ATR crystal, mid-IR light waves penetrate into the sample and the absorption spectra can be obtained. Instead of using an ATR crystal, mid-IR waveguide spectroscopy has a similar sensing principle based light absorption in the evanescent field, and also a great potential for the development of a compact and integrated device for bio-chemical sensing applications [5,6,28].

In this chapter, we demonstrated the integration of a Ge-on-Si waveguide with a microfluidic chip and its sensing applications in liquid environments. Cocaine detection was a pilot example to prove this technology. The light source was a QCL with the wavelength of 5.8 μm , which overlapped with one absorption peak of cocaine molecules. We dissolved cocaine in tetrachloroethylene (PCE), which is an organic solvent with high transmittance in a wide spectrum of mid-IR. Cocaine solutions of different concentrations flowed through the microfluidic channel and covered a certain length of the waveguide. The absorption in the evanescent field of the waveguide could be detected by measuring the waveguide transmission. By using an integrated splitter and a reference waveguide, the limit of detection can be calculated to be 5 $\mu\text{g/ml}$.

One potential application for this device is the detection of cocaine in human saliva, which would need an extraction of cocaine from saliva to PCE. While the typical concentration of cocaine in saliva is in the range of 1 $\mu\text{g/ml}$ (30 minutes after smoking cocaine) [4,82], further improvement of the sensitivity is necessary for this task.

4.1 Sensing scheme and the selection of wavelength

The sensing scheme is illustrated in figure 4.1, where the liquid sample covers a certain length of the Ge waveguide. The light from a QCL is injected from one facet of the waveguide and the output intensity is measured from the other facet.

In the evanescent field of the waveguide, the light wave penetrates into the liquids and decays exponentially with the distance. The analytes near the waveguide can absorb the light and reduce the total transmission of the waveguide, and the concentration of the analytes can be determined by monitoring the output intensity.

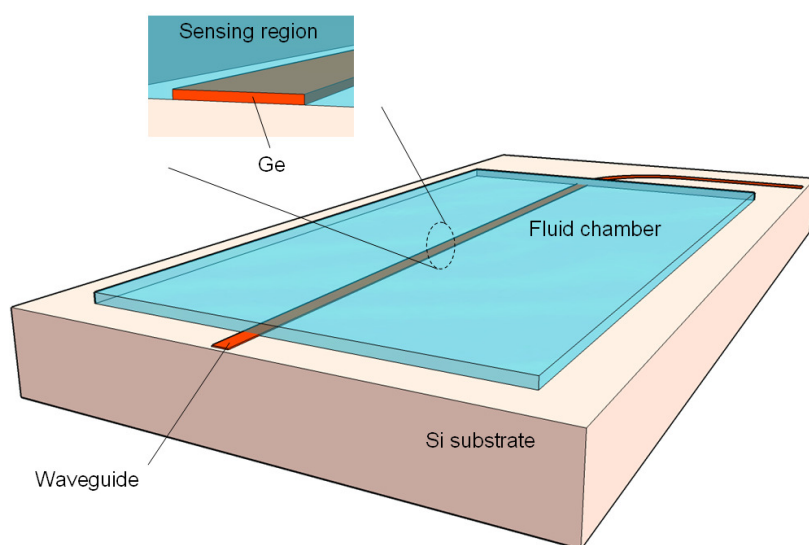


Figure 4.1 Sensing scheme: Molecules of the analytes in the fluidic chamber absorb light in the evanescent field of the waveguide. The concentration of analytes can be determined by monitoring the waveguide transmission.

When the sensing is based on the absorption of mid-IR radiations, which are in the wavelength of the fundamental molecular vibration frequencies, the selectivity of target molecules is achieved by the detection of specific absorption spectrum. While other optical methods (e.g. surface plasmon resonances or optical resonators) often need labeling molecules or functionalized layers, this method needs no additional intermediate medium for the detection of specific molecules.

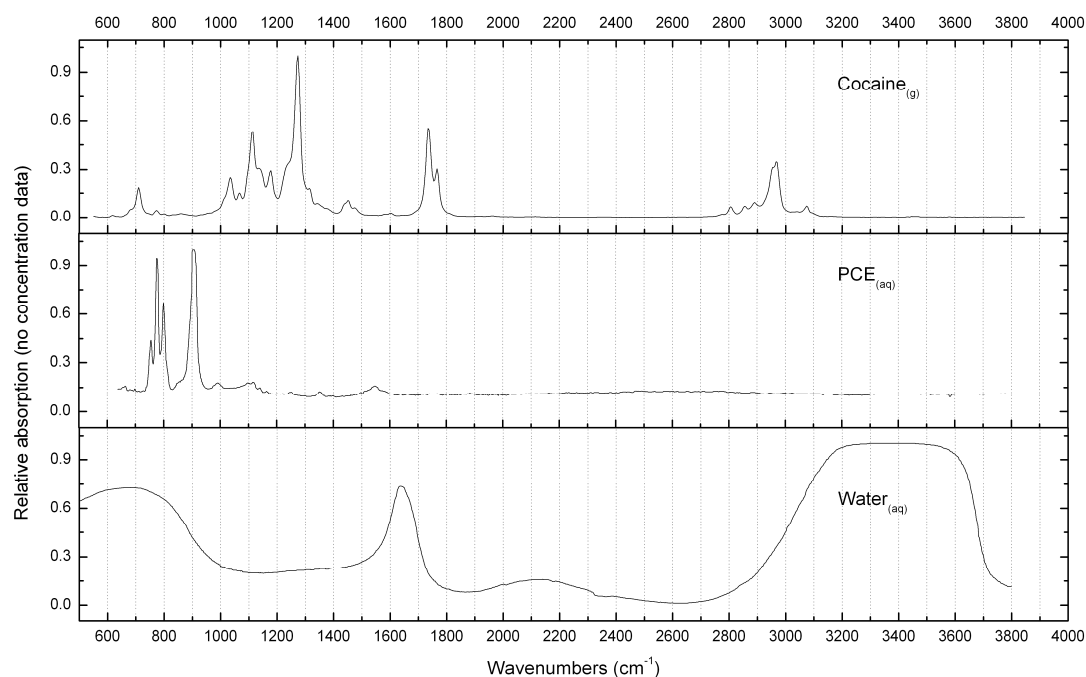


Figure 4.2 Absorption spectrum of cocaine, PCE, and water: The characteristic absorption peak of cocaine near $5.8 \mu\text{m}$ ($1720\text{-}1750 \text{ cm}^{-1}$) was chosen as the working wavelength. PCE has low absorption in a broad mid-IR band. [32] NIST Chemistry WebBook.

Cocaine is an addictive stimulant drug for forensic analysis, and here it is used to demonstrate mid-IR spectroscopy in liquids. As shown in figure 4.2, cocaine has absorption peaks in the fingerprint region from 500 cm^{-1} to 1500 cm^{-1} , and also peaks near $1720\text{-}1750 \text{ cm}^{-1}$ [4,32] from its carbonyl functional group, which is a carbon atom double bonded to an oxygen atom. The absorption spectrum of water in figure 4.2 shows strong absorption in the mid-IR. Since water is the main constituent of human fluids (eg. saliva or plasma), its strong absorption often hinders the sensitivity and the application of mid-IR spectroscopy for biological samples. To deal with the strong absorption of water, one can remove the water by drying the liquid samples before measurements, or extract the cocaine from human fluids to some mid IR transparent solvents. The spectrum of PCE (tetrachloroethylene) in figure 4.2 shows a wide window of low absorption in the mid-IR and is suitable for the extraction of cocaine for the measurement with mid IR spectroscopy [4]. In this study, we demonstrated the detection of cocaine molecules which was dissolved in PCE.

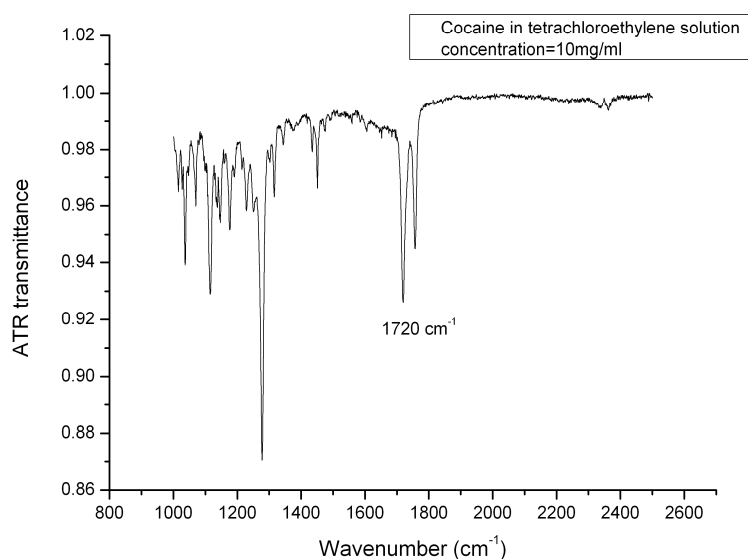


Figure 4.3 ATR transmittance spectrum of cocaine dissolved in PCE: It is measured with the cocaine concentration of 10mg/ml with ATR-FTIR.

Because QCLs has a high flexibility of the wavelength range covering almost the entire mid-IR, we were able to choose the working wavelength for an optimized device performance. Figure 4.3 is the ATR-FTIR transmission spectrum of cocaine dissolved in PCE with the concentration of 10 mg/ml. If we consider the highest absorption, the peak near 1278 cm^{-1} was strongest and could give a highest signal contrast. However, the absorption peaks near $1720\text{--}1750\text{ cm}^{-1}$ were found to be less influenced by some masking substances like sugar, milk powder, and Coca-Cola-Zero rather than the peak near 1278 cm^{-1} [4]. Therefore, the wavelength of the QCL was chosen to be near $5.8\text{ }\mu\text{m}$.

4.2 Integrated microfluidic chip

Microfluidic systems have been used together with infrared analysis. In combination with chromatography or electrophoresis, separated microfluidic chips have the functions of sample preparation or pre-concentration before the conventional IR-detection [25-27,57-59]. A microfluidic device integrated with a planar chalcogenide glass waveguide on a silicon substrate has been presented for the detection of N-methylaniline at the wavelength of $1.55\text{ }\mu\text{m}$ [28]. Commercial products combining QCLs and flow cells for the detection of oil in water are also available from the company, QuantaRed Technologies [60].

In this study, a microfluidic chip was integrated with the Ge-on-Si strip waveguide. In this device, the microfluidic chip had the function to control and deliver liquid samples to the sensing area, which was the evanescent field of the waveguide. Especially for liquids with high volatility, a closed microfluidic chamber was necessary to prevent the evaporation of solvents and to ensure stable compositions and concentrations of the liquid samples. In the sensing

chamber, the liquid samples could cover the Ge waveguide, and the flow speed is controlled by a syringe pump. Samples with different composition and concentration could be switched conveniently via a valve. In a further study, the integrated microfluidic system can be extended to have more functions like pre-concentration or liquid-liquid extraction [31].

PDMS (poly-dimethyl-siloxane) is the most widely used material for microfluidic devices because micro-sized channels can be easily fabricated through replica molding [61]. However, it is not compatible with many organic solvents because of the problems of swelling and delaminating from the substrate [62]. Here, we used a low-cost UV-curable adhesive NOA81 (Norland Optical Adhesive 81, Norland Product Inc., Cranbury, NJ, USA) as the material of the microfluidic chip. Compared with PDMS, NOA81 has better chemical resistance, is impermeable to air and water vapor, and is less prone to swell during the contact with some organic solvents which has low absorption in the mid-IR (including PCE) [63,64]. In addition, it has been shown to have low adsorption of cocaine (in aqueous or organic solvents), and of proteins (interleukins from blood) [65,66]. The stiffness of cured NOA81 is about 1 GPa [67], which allows the building of wide microfluidic channels which do not collapse under the negative pressure used to suck the liquids through the device.

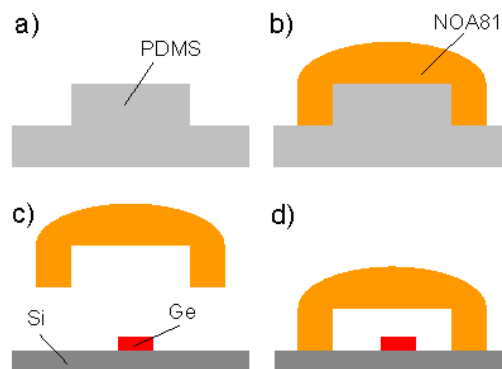


Figure 4.4 Fabrication flow of the microfluidic chip: a) PDMS master for rapid prototyping, b) NOA81 cast on PDMS, c) Ge-on-Si waveguide and un-molded microfluidic chip, d) final device: the microfluidic system was bonded on the Si substrate and formed the chamber for light-liquid interactions.

The microfluidic chips were fabricated by Philip Wagli of SAMLAB (The Sensors, Actuators and Microsystems Laboratory), with NOA81 by using the method of rapid prototyping [63]. As shown in figure 4.4, the microstructures of the channels were first defined on a PDMS master. NOA81 was then cast and cured on top of the PDMS. After separation from the master, the microfluidic device was bonded to the Si substrate of the Ge waveguide with oxygen plasma treatment. After bonding, NOA81 was cured further under a UV lamp. A high temperature treatment at 130 °C for 1 hour enhanced the adhesion to the Si substrate.

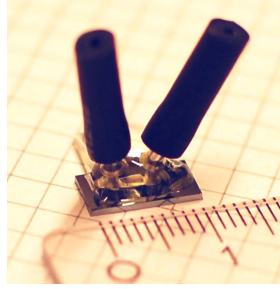


Figure 4.5 Photo of a Ge-on-Si waveguide bonded with a microfluidic chip: The microfluidic channel was 1mm wide, 7 mm long, and 50 μm deep.

Figure 4.5 shows a photo image of a microfluidic chip integrated with a Ge-on-Si waveguide. The microfluidic design was a simple straight channel with one inlet and one outlet for liquid samples. The fluidic channel was 1mm-wide, 7mm-long, and 50 μm -deep. It was on top of the Ge waveguide and formed the sensing chamber for light-liquid interactions. The inlet and outlet of the channel were designed on top of the device and connected to the tubing of the fluidic driving system.

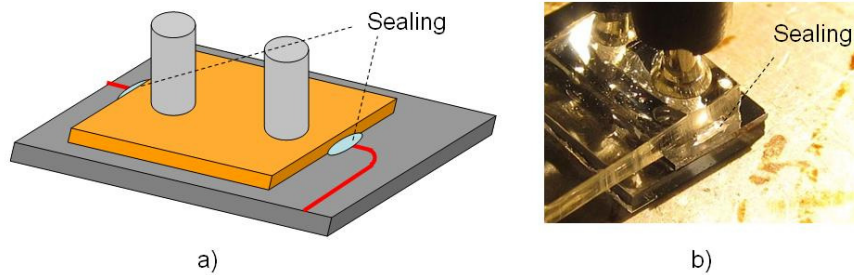


Figure 4.6 The sealing at the waveguide interface: a) the illustration of the sealing at the interface of the waveguide and the microfluidic device, b) a photo image of the sealing

At the interface of the Ge strip waveguide and the microfluidic channel, the waveguide crossed over the wall of the fluidic chamber and reached the edges of the Si substrate. Due to the high stiffness of NOA81, the chamber walls could not be deformed to adapt the rectangular shape of the waveguide, and liquids could leak through this opening. As shown in figure 4.6, we sealed up the opening at the waveguide interface with an additional gluing process. Because this glue stayed in a close contact with the Ge waveguide in the evanescent field, the material of the glue should have low absorption in the working wavelength to avoid additional light absorption and the reduction of the device performance. Instead of using conventional UV-curable adhesives which usually have strong absorption in the mid-IR, we sealed the opening with a piece of heated PE (polyethylene). At the temperature near 120 $^{\circ}\text{C}$, a piece of PE was placed at the

interface of the waveguide and the wall of the fluidic chamber. Near this temperature, it started to become soft and able to flow around to cover the opening.

4.3 Static measurement of cocaine with changes of propagation loss

The measurement setup is shown in figure 4.7. It consisted of an optical system for measuring the waveguide output light intensity, and a syringe pump system to drive the fluidic flow in the micro channels. The optical system was based on the end-fire coupling method described in section 3.4.1. The light from the QCL was injected into the waveguide via 2 lenses made from ZnSe. After interaction with the liquid sample in the fluidic chamber, the light went through a 90° bend to the right, and was collected to the MCT detector with two off-axis parabolic mirrors.

The outlet of the microfluidic device was connected to a syringe pump, which sucked the liquid sample through the fluidic channel. With a negative-pressure driving, the microfluidic chip was less prone to detach from the Si substrate. By changing the speed of the syringe pump, one could control the flow rate of the microfluidic channel or keep the liquid sample in a static state. The inlet of the microfluidic device was connected to a multi-selection valve, which was able to switch the samples with different concentrations of cocaine dissolved in PCE in different reservoirs.

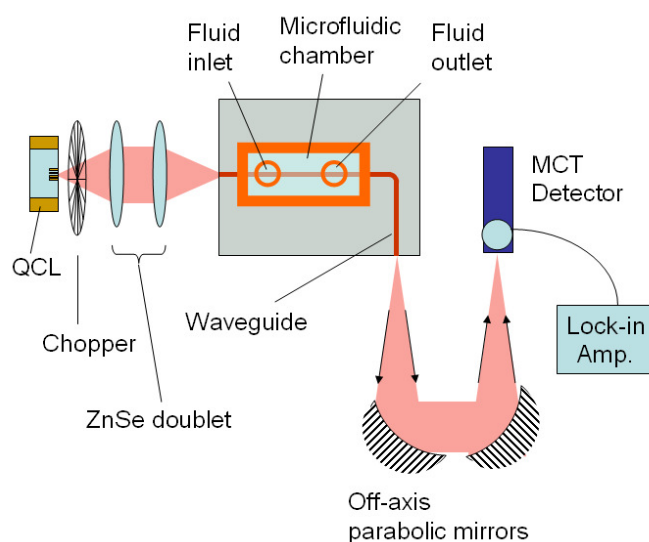


Figure 4.7 Setup for cocaine measurement: With the configuration of end-fire coupling method, the waveguide output intensity was measured while the microfluidic chamber was filled with cocaine in PCE solutions.

At first, the measurement was done in a static state, in which the flow in the microfluidic channel was blocked during the data acquisition. Samples with different concentrations were sucked into the sensing chamber and measured separately. The cocaine we used has the purity >98 %, and was purchased from Lipomed AG Switzerland with the permission of the Cantonal Drug

Administration of Neuchatel. We dissolved the cocaine into PCE with concentrations of 10mg/ml, 5mg/ml, 1mg/ml, 100 μ g/ml, 10 μ g/ml, and pure PCE.

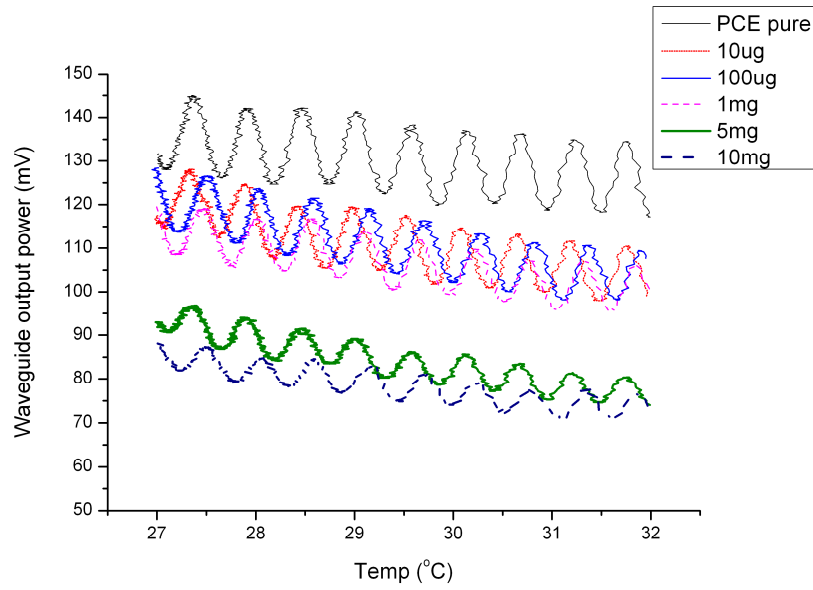


Figure 4.8 Fabry-Perot resonance fringes with different cocaine concentrations: When the concentration of cocaine was higher, the modulation depth became smaller.

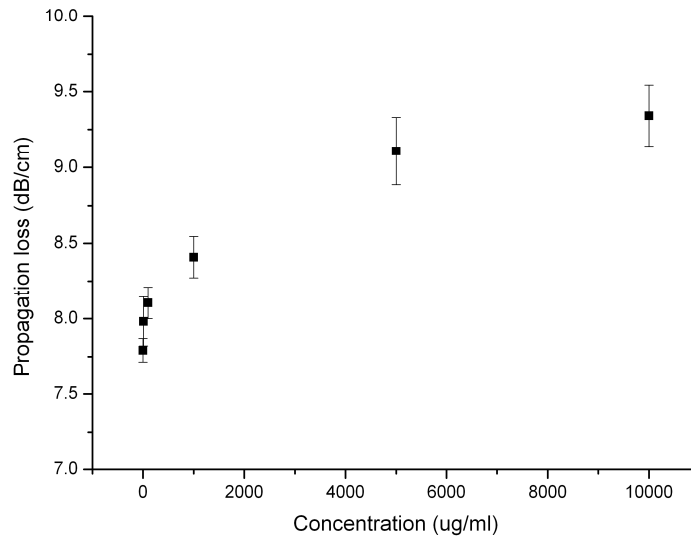


Figure 4.9 Propagation loss with different cocaine concentrations (error bar is the standard deviation): The propagation loss increased with the cocaine concentration. In high concentration region, the relationship was not linear, which might be induced by the residue of sample in a previous measurement.

In the static measurement of cocaine, the Fabry-Perot resonance fringes were recorded by varying the temperature of the device in a small range from 27 $^{\circ}$ C to 32 $^{\circ}$ C. For the same Ge strip waveguide, we filled the microfluidic channel

with cocaine solutions of different concentrations, and performed the measurements. As shown in figure 4.8, when the concentration of cocaine increased, both the average transmitted power and the modulation depth of the fringes decreased. It showed that the cocaine molecules in the evanescent field of the waveguide absorbed a part of the light, reduced the transmitted light, and increased the propagation loss.

See section 3.5.1, according to equation 3.6, the propagation losses were calculated from the Fabry-Perot resonance fringes and plotted in figure 4.9. For the same waveguide, the propagation loss increased while the concentration of cocaine increased. In the region of lower concentrations, the change of the propagation loss was small and masked by the measurement errors. The accuracy of measured propagation loss determined the detection limit to a high level of approximately 500 μ g/ml. According to the Beer-Lambert law, the propagation loss should be linearly proportional to the concentration of cocaine. However, in the high concentration region in figure 4.9, the propagation loss started to become non-linear when it was near 5mg/ml. One possible reason for this phenomenon is that the measurement of each concentration is influenced by the residue of an earlier concentration.

4.4 Dynamic measurement of cocaine

The detection of cocaine with static measurement was limited by the accuracy of the measured propagation losses. Due to the nature of the measurement method based on Fabry-Perot resonance fringes, the measured propagation loss had a larger error, when the total attenuation of the waveguide became larger [54]. This meant that the loss measurement result of a longer waveguide was less accurate than a short waveguide, provided they have the same propagation loss for a unit length. For the static measurement based on the relationship of the propagation loss and the analytes concentration, this property was a dilemma for the detection of low concentrations of analytes. On one hand we would like to minimize the error of the measured propagation loss, by shortening the length of the waveguide to reduce the total attenuation. On the other hand we would like to enhance the interaction volume of the light and the molecules, by increasing the waveguide length. Since the propagation loss of a unit length was not a number close to zero, the error of the loss measurement would increase with the length of the waveguide.

To overcome the limit of detection appeared in the static measurement. In this section, we studied the detection of cocaine with a dynamic measurement, where the liquid in the microfluidic channel kept a constant flow. With the same experiment setup as in the static measurement, here the syringe pump kept sucking the liquid with a constant rate. A syringe pump was a mechanical device which pulls the plunger of a fixed syringe with a controlled and accurate speed. The inner diameter of the syringe was 15mm and the flow rate was set to be 50 μ L/min.

Instead of measuring the propagation loss of the waveguide, we monitored the output light intensity in real time, while the flow rate of the liquid was kept constant. In this dynamic measurement, the readings of the light were recorded and compared with each other continuously during the measurement. The output light intensity indicated the amount of cocaine molecules in the evanescent field through the Beer-Lambert law. Here the reference signal was from a flow of pure PCE in the microfluidic channel. Before the inlet of the channel, the multi-selection valve switched the liquid samples of different concentrations during the measurement. These concentrations were 10mg/ml, 5mg/ml, 1mg/ml, 100 μ g/ml.

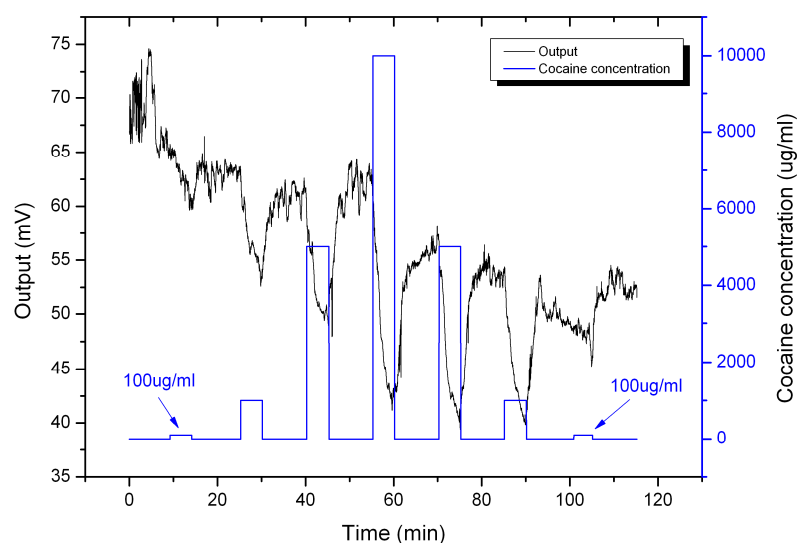


Figure 4.10 Output light intensity and cocaine concentration with time: The output light intensity responded well to each switch of concentrations. The lowest measured concentration was 100 μ g/ml.

Figure 4.10 plotted a measurement result of the output light intensity during the flow with cocaine solutions of different concentrations. First the microfluidic channel was filled with pure PCE, and then it was followed by a sequence of cocaine in PCE solutions. Between each cocaine solutions, we added flows of pure PCE for 10 minutes. The output light intensity responded well to each switch of concentrations. When we compared the intensity drop of each concentration, we did not see a logarithmic relationship. The peak of each concentration did not reach a saturated and stable level, and it was probably due to the mixing of liquids in the channels. At the mean time, the absorption of cocaine molecules at the concentration of 100 μ g/ml could be barely recognized, because of the noises in the optical system. These fluctuations could be attributed to many factors in the laboratory and in the setup of experiments. They included temperature fluctuations, mechanical vibrations, the air humidity, the coupling stability, the laser stability, and also the mixing of liquids in the microfluidic channels.

4.4.1 Thermal fluctuations due to Fabry-Perot fringes

In a Ge-on-Si strip waveguide, the two end facets had high reflectivity and formed a resonant cavity, which resulted in the Fabry-Perot fringes on the transmittance when the waveguide temperature was varied. In section 3.5.1, we used this phenomenon to determine the propagation loss of each waveguide. However, when we used the waveguide in the device for cocaine detection, these resonance fringes became one major source of noises. The transmittance of the waveguide fluctuated together with small variations of the device temperature. These fluctuations were related to the modulation depths of the Fabry-Perot fringes. Figure 4.11 shows the output intensities of two waveguide with different modulations depths, and the waveguide temperature changed slightly with time. For the waveguide with a larger modulation depth, its output light intensity could fluctuate in a larger range than a waveguide with a low modulation depth. The range of the fluctuation approximately equaled to the modulation depth of the Fabry-Perot fringes of each waveguide.

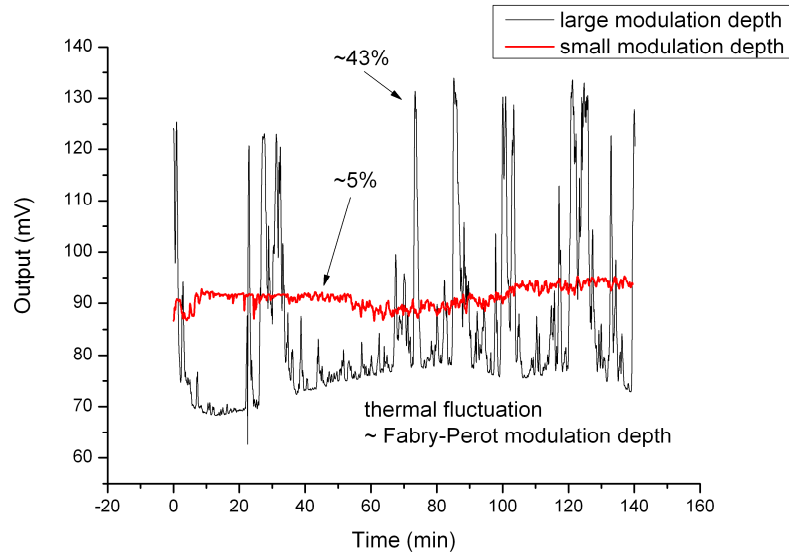


Figure 4.11 Fluctuation due to Fabry-Perot fringes: The waveguide output light intensity fluctuated together with the temperature of the device. The waveguide of higher finesse had a larger modulation depth in the fringes, and therefore fluctuated in a larger range.

The fluctuation of the waveguide transmittance was caused by small variations of the device temperature. See section 3.5.1, from equation 3.4, the transmittance of a waveguide can be written as

$$t = \frac{I}{I_0} = \frac{(1 - R)^2 A}{1 - 2RA \cos \delta + R^2 A^2}, \quad A = 10^{-\alpha L} \quad (eq.4.1)$$

where A is the attenuation of the light traveling through the total waveguide length, and it is a number between 0 and 1. When t is divided by its maximum value, the normalized transmittance is

$$t_n = \frac{(1 - RA)^2}{1 - 2RA\cos\delta + R^2A^2} \quad (eq.4.2)$$

Here δ is the phase difference of a full round trip of light inside the waveguide, and is dependent on the temperature. For Ge waveguides, thermal expansion in the length L makes only a small effect on the phase difference, when it is compared with the refractive index changes caused by the thermal optical effect. If we neglect the thermal expansion of L , the derivative of t_n with respect of the temperature T is

$$\frac{dt_n}{dT} = \frac{-4RA(1 - RA)^2}{(1 - 2RA\cos\delta + R^2A^2)^2} \cdot \frac{2\pi}{\lambda} \sin\delta \cdot L \cdot \frac{dn_{eff}}{dT} \quad (eq.4.3)$$

During a temperature variation, the transmittance of the waveguide fluctuates with a slope as in the function above. It is zero when the phase difference δ is an integer multiples of π , where the transmittance is at the maximum or the minimum.

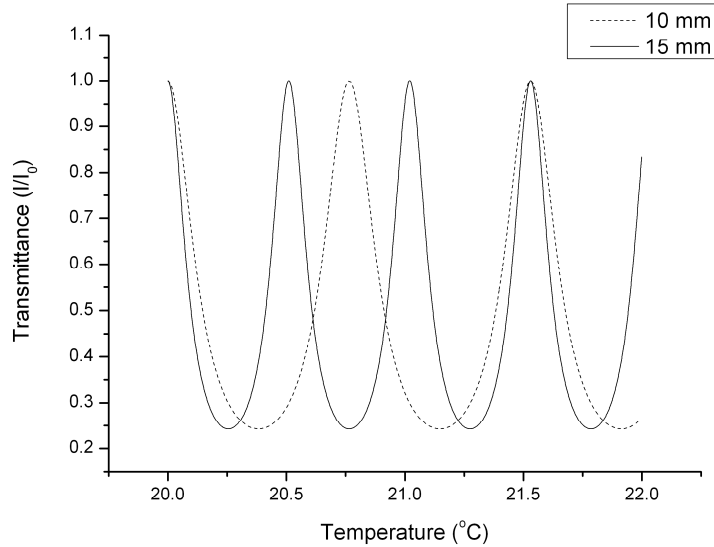


Figure 4.12 Simulated transmittance of waveguide with no loss: When there was no propagation loss, the 15mm long waveguide was more sensitive to temperature variations.

If the waveguide has no propagation loss, which means A equals unity, the maximum slope is linearly proportional to the waveguide length L . In this case, a longer waveguide is more sensitive to temperature fluctuations. As the simulation shown in figure 4.12, the 15 mm waveguide was longer and its transmittance was

more sensitive to temperature variations. For a temperature variation of 0.02°C , the transmittance of the 10mm waveguide could have a maximum change of 8.5% while the 15mm waveguide could have a maximum change of 13%.

However, the propagation losses in real waveguides actually prevent the increase of the sensitivity to temperature variations when the waveguides are made longer. In fact, the maximum slope starts to decrease when the total attenuation is approximately 5dB.

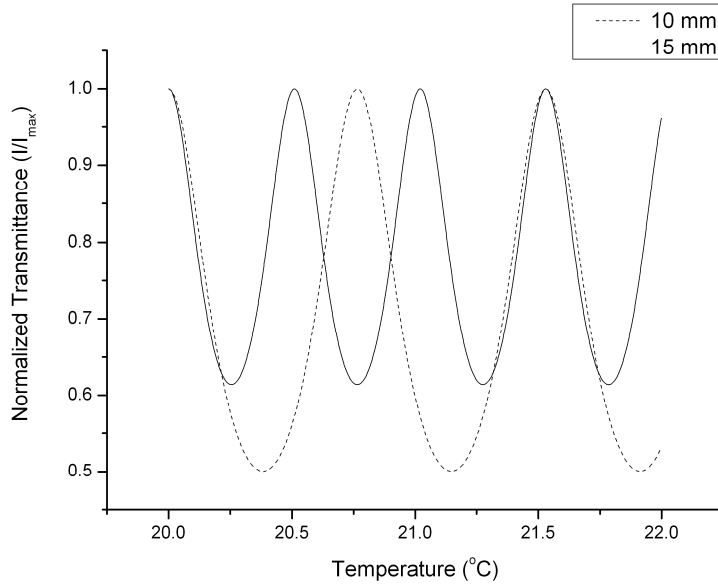


Figure 4.13 Simulation of normalized transmittance for waveguide with the propagation loss of 3 dB/cm: The 15mm and 10mm waveguides had similar sensitivities to temperature variations.

For example, fig 4.13 shows the simulation of the normalized transmittance of two waveguides with the same propagation loss of 3 dB/cm but different total lengths. The 15mm waveguide had a faster oscillation of transmittance with varying temperature, but also a smaller modulation depth due to the larger total attenuation. It resulted in a similar sensitivity to variations of the device temperature for both the 10mm and the 15mm waveguides. At the positions of maximum slopes, a temperature fluctuation of 0.02°C could introduce a change of nearly 5% in the waveguide transmittance. This noise is destructive for a sensing device based on the measurement of the output light intensity. To deal with this noise, several approaches will be presented in section 4.5.

4.4.2 Noise due to misalignment of the coupling

Another main source of noises was the stability of the coupling between the QCL and the waveguide. The coupling efficiency decreased when the QCL or the waveguide did not stay in the best aligned position. The end facet of the waveguide was $15\mu\text{m}$ wide and $2\mu\text{m}$ thick, while the emission facet of the QCL

had similar dimensions. Because both of the two facets were very small, the coupling efficiency was sensitive to mechanical fluctuations in the range of a micro meter. These positional fluctuations of the QCL and the waveguide can come from mechanical vibrations of the stages, or from thermal expansions of the elements in the measurement setup.

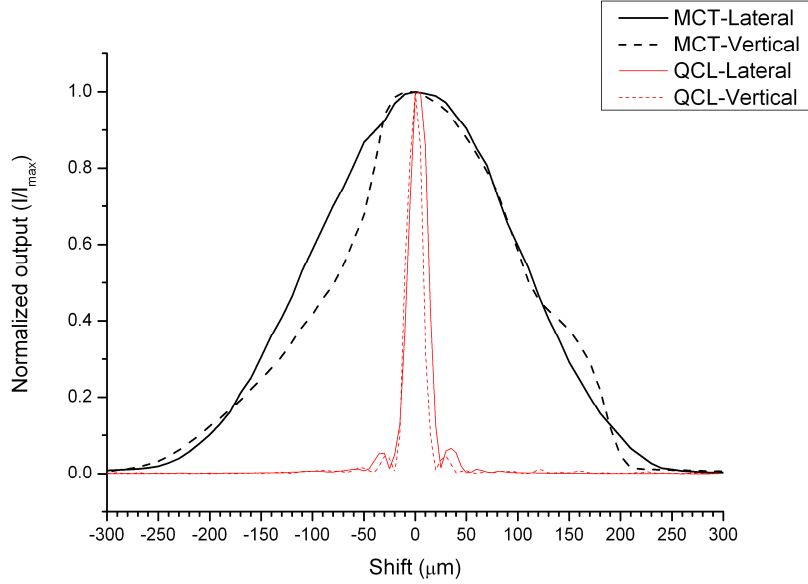


Figure 4.14 Measured output with the shift of QCL and MCT: The output light intensity is more sensitive on the shift of the QCL. The FWHM were about 20 μm and 210 μm for the shifts of QCL and MCT detector respectively.

The coupling between the waveguide and the MCT detector, on the contrary, was less sensitive to the fluctuation of positions. This was because the active element of the MCT detector had the size of 0.25mm x 0.25mm, which was able to collect the light from the waveguide output with a better stability. The output facet of the waveguide was 15 μm wide and 2 μm thick. After the two off-axis parabolic mirrors, the image of the waveguide facet on the detector was approximately a spot with the dimension of several tens micro meters. As shown in figure 4.14, we measured the output light intensity while the QCL and the MCT detector were shifted laterally and vertically. The reading dropped rapidly when the QCL was shifted, while it was relatively stable on the shifts of the detector. The FWHM (Full width at half maximum) of the shift of QCL was approximately 20 μm , while it was about 210 μm for the shift of the MCT detector.

4.5 Reduction of thermal fluctuations due to Fabry-Perot fringes

During the dynamic measurement of cocaine concentrations in the microfluidic channel, the output light intensity indicates the cocaine absorption in the evanescent field. However, the transmittance of the waveguide was strongly

dependent to the device temperature, because the Fabry-Perot resonance fringes could be shifted when the temperature variations change the phase difference δ . It was a main source of noises and limited the sensitivity of the device. Here we discussed some methods to reduce this noise and had employed them in our further measurements.

4.5.1 Temperature control of the device

The most simple and direct way to decrease this thermal fluctuation of transmittance is to maintain a good stability of the device temperature. This is normally done with an active temperature control, with a feed back of the actual temperature. Here we made a thermostat stage holding the device by mechanically clamping the Si substrate. As shown in figure 4.15, the Ge-on-Si waveguide was integrated with a microfluidic chip and sat on a metal stage. The stage was made from aluminum and connected to a Peltier thermo-electrical element. The other side of the Peltier element was attached to an aluminum thermal capacitor which exchanged heat with the stage. The stage was attached with a NTC thermistor, whose resistance was dependent on the temperature. A temperature controller measured the resistance, and determined the flow of the electrical current in the Peltier element, which could cool down or heat up the stage. One could set the desired resistance, and the stage temperature could be controlled in a range of 0.02 K.

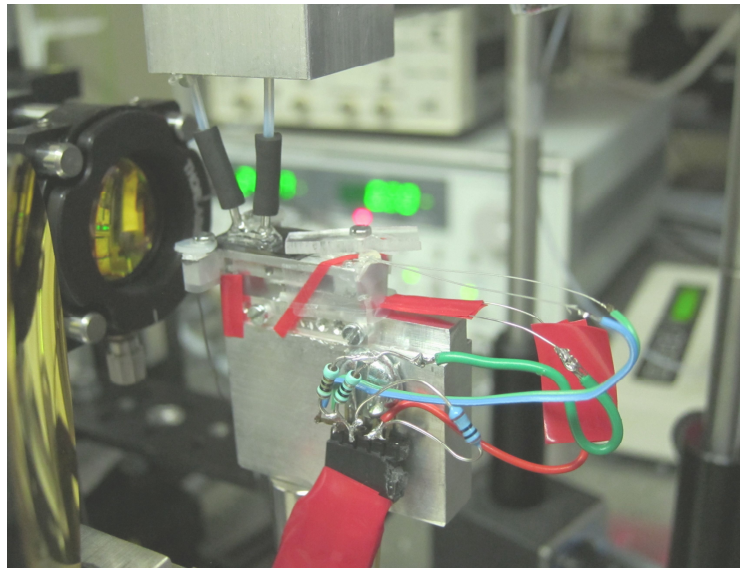


Figure 4.15 Photo of the temperature control of the device: The stage temperature was controlled by a Peltier thermal-electrical element and a NTC thermistor. The stage temperature was maintained in a range of 0.02 K.

Without using the thermal control system, the device temperature fluctuated easily with the ambient environment. The Si substrate had a large surface in contact with the air surrounding the measurement setup. Due to the

high thermal conductivity of crystalline silicon, the device temperature could change quickly with the air flow in the laboratory. Even in a closed room, the temperature of the waveguide could vary in a range more than 0.5 K because of the running machines and computers in the laboratory. For a 10mm-long Ge-on-Si waveguide with a propagation loss of 3 dB/cm, this could induce a transmittance change of nearly 50% in the maximum case. Moreover, the average ambient temperature in the laboratory could drift slowly because the air temperature changes during a day.

With the thermostat stage shown in figure 4.15, the temperature fluctuation was limited in a smaller range of 0.02 K. If we considered a 10mm-long Ge-on-Si waveguide which had a propagation loss of 3 dB/cm, the 0.02 K temperature shift could still induce a transmittance change around 5% in the extreme case. Therefore, to minimize this thermal fluctuation, it was important to work in the positions where the transmittance is the minimums or the maximums of the Fabry-Perot fringes. At these points, the slope of transmittance varying with temperature was close to zero. For the same 10mm-long waveguide, the transmittance change due to a temperature shift of 0.02 K could be limited to 0.1%, when the working temperature was set to the minimums of the fringes. Especially at the minimum positions, the transmittance was more stable than in the maximum positions. Although the total transmitted light could be smaller, these minimum positions could be useful when the laser source can provide enough power.

4.5.2 Reduction of the Fabry-Perot fringe contrast

Beside a temperature control system, another method to reduce this noise is to lower the modulation depth of the Fabry-Perot fringes. See section 3.5.1, from equation 3.5, the modulation depth h can be obtained by

$$h = \frac{P_{max} - P_{min}}{P_{max}} = \frac{4R \cdot 10^{-\alpha L}}{1 + 2R \cdot 10^{-\alpha L} + R^2 \cdot 10^{-2\alpha L}} \quad (eq.4.4)$$

Here, R is the reflectivity at the two waveguide end facets and is approximately linearly proportional to the modulation depth h , when the attenuation of light over the total waveguide is large. Therefore, anti-reflection treatment on the two end facets is an effective passive method for the noise reduction. In our case, the Ge-on-Si waveguide had the reflectivity of 0.34 at the two end facets. At the interface of the Ge facet and the air, the reflection can be diminished by adding dielectric multilayer coatings or anti-reflection subwavelength structures on the waveguide ends. In theory, these treatments are possible to reduce the reflection to a level less than 1%, which is an improvement of more than 30 times for the noise of Fabry-Perot fringes. Moreover, the total transmittance of the Ge waveguide can also increase by a factor of 1.5-2, which allows more light to be used for the sensing purpose. Section 5.2 will present more details about the anti-reflection treatment of Ge-on-Si waveguides.

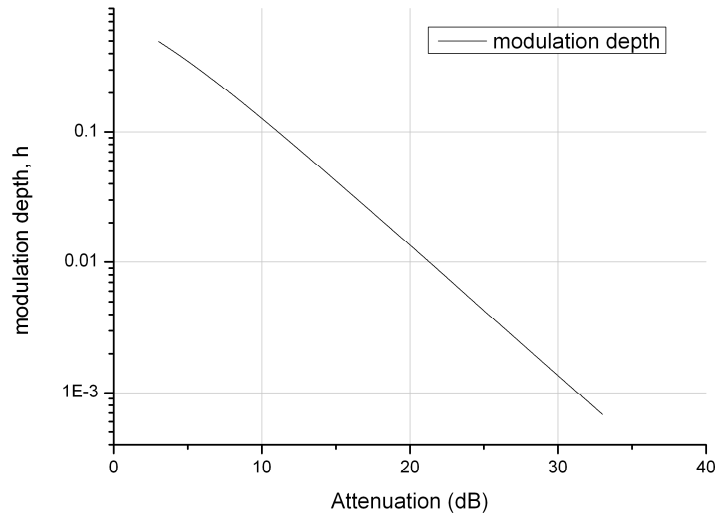


Figure 4.16 Simulated modulation depth with varied attenuation: The reflectivity was 0.34. With higher transmission losses, the modulation depth was approximately linear to the attenuation $10^{-\alpha L}$. When the attenuation was 30dB, the modulation depth h was around 0.14%.

The other way to reduce the modulation depth is to increase the total attenuation of light during the propagation in the waveguide. For a waveguide with a large transmission loss, the modulation depth approximately linearly decreases with an increasing attenuation. Figure 4.16 shows the simulation of the modulation depth of the Fabry-Perot fringes with varied attenuation of the waveguide. For a Ge-on-Si waveguide which had two end facets with the size of $15\mu\text{m} \times 2\mu\text{m}$, the reflectivity was 0.34 in the air environment. When the attenuation increased to 30dB, the modulation depth was about 0.14%, which is the fluctuation range for the noise from the Fabry-Perot fringes.

To increase the attenuation of the waveguide, one can enlarge the propagation loss of a unit length, or increase the total length of the waveguide. When we considered only the reduction of the noise induced by the Fabry-Perot fringes, enlarged propagation loss seemed a better solution. Because when we increased the total length of the waveguide, the fringes also increased the oscillating frequency with varying temperature, as described in equation 4.3. If the waveguide attenuation was low, the maximum slope of the fringes increased with the waveguide length. However, if we considered the waveguide as a sensing device, a longer waveguide also meant a larger interaction volume with the liquid samples. The light waves could travel through a longer distance, where the absorption in the evanescent field by the cocaine molecules could be larger.

Figure 4.17 shows the slope described in equation 4.3, the contour of the curve was the maximum slope of the transmittance with varied temperature. Here we assumed the waveguide had a propagation loss of 3dB/cm, and the reflectivity of the end facets was 0.34. When the waveguide length was about 17 mm and the total attenuation was around 5 dB, the maximum slope started to decrease with

the increasing waveguide length. When the length reached 67 mm, where the attenuation was 20dB, the maximum slope was approximately 0.357. In this case, a thermal fluctuation of 0.02 K could produce a maximum change of 0.714% for the waveguide transmittance. Here the noise was reduced by a longer waveguide length and enlarged attenuation.

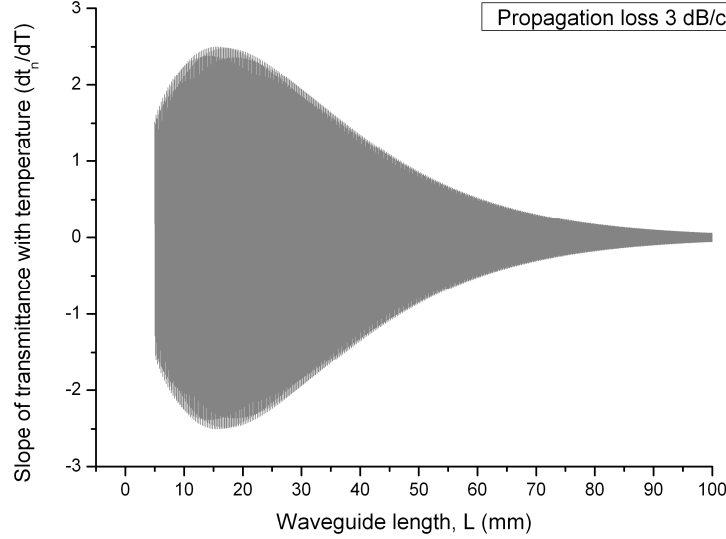


Figure 4.17 Simulated slope of the transmittance with varied temperature: The contour of the curve shows the maximum slope of the Fabry-Perot fringes with different waveguide length. The propagation loss was assumed to be 3 dB/cm and the reflectivity was 0.34.

This noise due to the resonance fringes could be suppressed largely with the increased attenuation. However, the total transmission of the waveguide was also reduced to a very low level, which challenges the sensitivity of mid-IR detectors. When the output light intensity from the waveguide decreased to a certain level, the noise from the detector itself started to become the bottle neck of the sensitivity of the device. In the case of using high power QCLs, increasing the attenuation of the waveguide could be a good choice for noise reduction.

4.5.3 Noise reduction with a pulse-driving QCL

Another method to reduce the noise from the resonant fringes is to compensate the fringes with each other by using a light source with a wider linewidth. Consider two lasers of different wavelengths where their Fabry-Perot fringes have a phase shift of π from each other. While the waveguide temperature changes, the transmittance of the two wavelengths would shift in opposite directions. If the responses of the photo-detector are the same to the two wavelengths, the transmittance shifts can be compensated with each other and the fluctuation is reduced.

The basic idea of this method is shown in figure 4.18. The transmittance of the waveguide is dependent on the wavelength of the light, and shows the

Fabry-Perot resonance fringes. When the light source is a laser with a sharp spectrum, as shown in figure 4.18a, one can obtain the resonance fringes by measuring the transmittance during a shift of the laser wavelength or the Fabry-Perot fringes. In section 3.5.2, we shifted the fringes by changing the temperature of the waveguide.

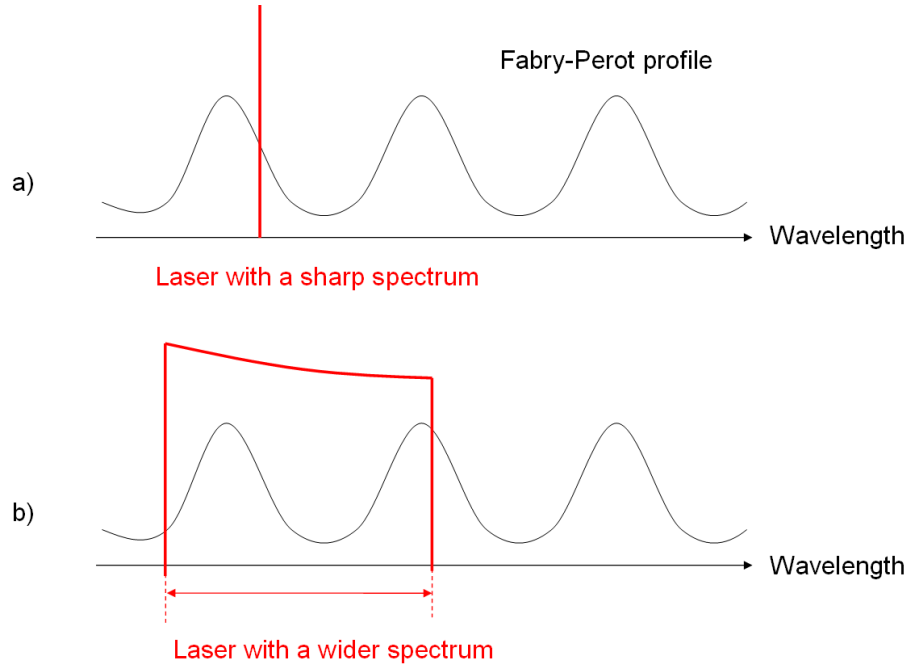


Figure 4.18 Scheme of noise compensation of Fabry-Perot fringes: A light source with a wider spectrum can cover more than half a period in the resonance fringes. The peaks and valleys compensate with each other, and the waveguide transmittance is less sensitive to temperature variations.

In figure 4.18a, the output light intensity was the laser power multiplied with the waveguide transmittance at the laser wavelength. In consequence, small temperature fluctuations could shift the fringes and induce a large noise on the output light intensity. If a light source with a wider spectrum is used, as shown in figure 4.18b, the spectrum of the light can cover more than a half period of the Fabry-Perot fringes. The transmittance of the waveguide is then the integration over the spectrum of the light source. The peaks and valleys of the fringes compensate with each other, and make a stable output light intensity during temperature variations. Note that the response of the photo-detector to different wavelengths should be relative flat in this range.

To compensate the thermal fluctuation, the required spectral distribution of the light source depends on the resonance fringes of the waveguides. The linewidth of the laser should be broad enough to cover more than a half period of the fringes. Between two adjacent resonance peaks of the fringes, the wavelength difference is the free spectral range (FSR) for the waveguide cavity. See section 3.5.1, from equation 3.2, FSR approximates to

$$\Delta\lambda = \frac{\lambda^2}{2n_{eff}L} \quad (eq.4.5)$$

For a Ge-on-Si strip waveguide which was 2 μm thick and 2.9 μm wide, the effective index was simulated to be 3.73 by using a FDTD method. When the waveguide was made to 10mm long, the FSR was 0.45 nm (0.134 cm^{-1}) for the wavelength of 5.8 μm . Figure 4.19 shows the simulated transmittance of a 10mm-long waveguide with a propagation loss of 3 dB/cm.

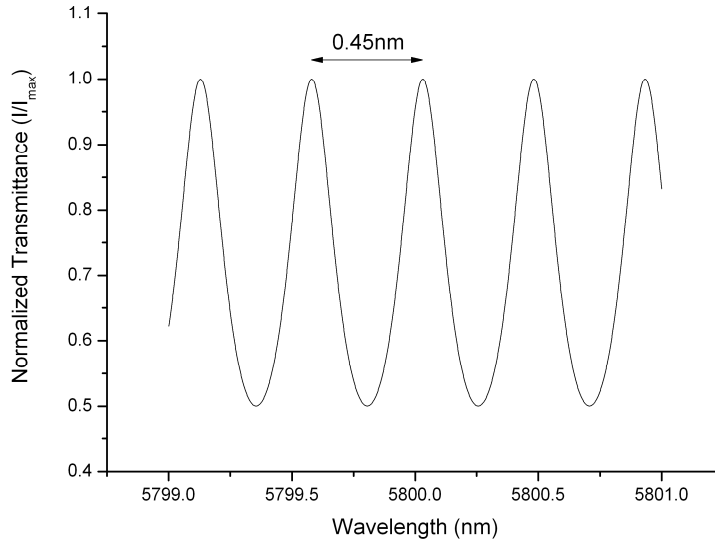


Figure 4.19 Simulated free spectral range: The FSR was 0.45 for a 10mm-long Ge-on-Si strip waveguide which had an effective index of 3.73 when the wavelength was 5.8 μm .

The FSR was inversely proportional to the waveguide length L . When the waveguide was made longer for a smaller FSR, the same light source could cover more periods of the resonance fringes. This was desirable for the reduction of this type of noise, because when we convolved the resonance fringes with the spectrum of the light, the result was smoother with a larger number of fringes in the spectrum of the light.

In our measurement setup shown in figure 4.7, the light source was a DFB-QCL driven in a continuous-wave (CW) mode, which gave a very sharp spectrum near 5.8 μm . The emission spectrum of a DFB-QCL in the CW mode can have a linewidth smaller than 0.001 cm^{-1} (<0.00336 nm) [68], which is important when we want to resolve the resonance fringes of the waveguide. The narrow linewidths of these lasers are also important for the sensing applications of gases, because most absorption spectra of gases have characteristic fine structures. On the contrary in the spectroscopy of liquid samples, absorption peaks are usually broadened and wider than several cm^{-1} [22,23]. Therefore, a

narrow linewidth of the light source is not necessary for this cocaine detection in a liquid phase. A wider spectrum about 1 cm^{-1} does not change much the amount of light absorption, but can very well compensate the noise from the resonance fringes of the waveguide.

The spectrum of the QCL could be broadened in several ways, including varied temperature of the QCL, and varied driving current. Here we used the pulsed driving method. Instead of a continuous DC source, we sent pulses with the duration of several hundred nanoseconds, while the frequency was 90K Hz. In the duration of a single pulse, the temperature of the QCL rose up with time because of a large amount of heat was generated [69,70]. The refractive index of the laser material varied with the temperature, and changed the cavity length of the laser resonance. The emission wavelength of the QCL drifted from a shorter wavelength to a longer one, and the linewidth of QCL expanded. This expansion depended on the duration of a single pulse. For a pulse in the range from 0 to several hundreds of nanoseconds, a longer pulse gave a wider linewidth. When the pulses were sufficient long or in a CW driving mode, the QCL established a thermal equilibrium, and the linewidth become narrower.

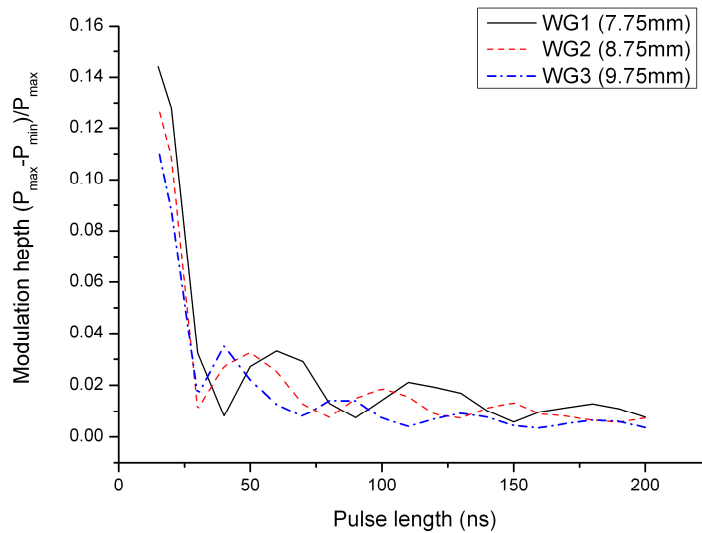


Figure 4.20 Measured modulation depth with varied pulse lengths: The QCL was in a pulse driving mode with different lengths of a single pulse. The modulation depth was reduced with an increasing linewidth of the QCL, while the pulse length increased. It reached local minimums when the linewidth covered odd numbers of a half FSR of the waveguide cavities.

The broadening of the linewidth could be seen from the Fabry-Perot fringes of the waveguide transmittance during a temperature scanning. As shown in figure 4.20, we drove the QCL with pulses of different durations from 15 ns to 200 ns. The temperature of the waveguide was varied to observe the Fabry-Perot fringes. The modulation depths of the fringes were plotted with varied pulse durations. The 3 curves were measurements from 3 waveguides of different

lengths. When the pulse was 15 ns, the modulation depth was large and close to the depth measured with a QCL in CW mode. The rapid drop from 15 ns to 20 ns represented that the linewidth of the QCL started to cover more than a half fringe of the Fabry-Perot curve. For the 9.75mm-long Ge-on-Si waveguide, a half of the FSR was 0.23 nm (0.069 cm^{-1}). As the pulses became longer, the modulation depth dropped slowly with some periodic oscillations. This was because the periodic shape of the Fabry-Perot fringes. When the spectrum of the QCL covered an integer multiples of a half FSR, the modulation depth reached local maximums or minimums. It can be written as

$$\text{linewidth} \sim \frac{1}{2} \cdot m \cdot \text{FSR} \quad , \quad \begin{cases} m = 1, 3, 5 \dots & \text{at minimums} \\ m = 2, 4, 6 \dots & \text{at maximums} \end{cases}$$

As shown in figure 4.20, the FSR of a longer waveguide was smaller, and the modulation depth oscillated faster with the increasing duration of the pulses. For waveguide WG3, whose FSR was 0.46nm (0.137 cm^{-1}), the oscillating period was around 50ns. This means the linewidth of the QCL increased with a speed of 0.092 nm/ns ($0.00275 \text{ cm}^{-1}/\text{ns}$) when we increased the duration of the pulses.

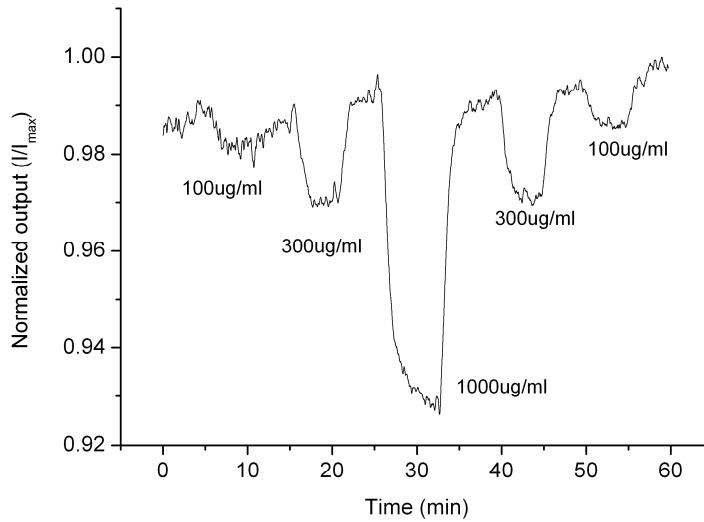


Figure 4.21 Measurement of cocaine with improved stability: The smallest measured concentration is 100 $\mu\text{g}/\text{ml}$. The absorption is approximately linearly proportional to the cocaine concentration.

For cocaine detection with the Ge-on-Si waveguide, we applied some above mentioned methods, including a thermal stabilized stage for the device, and the QCL in the pulse driving mode. As shown in figure 4.21, the absorption of cocaine molecules at the concentration of 100 $\mu\text{g}/\text{ml}$ could be better recognized with a better stability of the device. The absorption ratio was about 0.8% of the injected light for the peaks of 100 $\mu\text{g}/\text{ml}$. When the concentration increased to 300

$\mu\text{g/ml}$ and $1000 \mu\text{g/ml}$, the absorption ratio showed approximately a linear rise, which is in agreement with the Beer-Lambert law in the low absorption condition.

While the noise from the Fabry-Perot fringes was reduced, other noises started to dominate the limit of sensitivity. It was mainly from the mis-alignment between the QCL and the Ge waveguide, as described in section 4.4.2. This mechanical misalignment could cause both short-term fluctuations and long-term drifting of the coupling efficiency. For further improvement, a reference signal to eliminate this noise will be presented in section 4.8.

4.6 Response time of the device

In the detection of cocaine, we found the transition of the output light intensity was slow during the switch of concentrations. One of the reasons was the length of the tubing between the multi-selection valve and the inlet of the device.

We tested this by using a long ($\sim 20 \text{ cm}$) and a short ($\sim 6 \text{ cm}$) tube for the measurement of cocaine. As shown in figure 4.22, the cocaine concentration was switched between pure PCE and $100\mu\text{g/ml}$, and the response for the long tube was slower than the short one. The response time was the interval of 10% and 90% of the transmittance difference between pure PCE and the $100\mu\text{g/ml}$ cocaine solution.

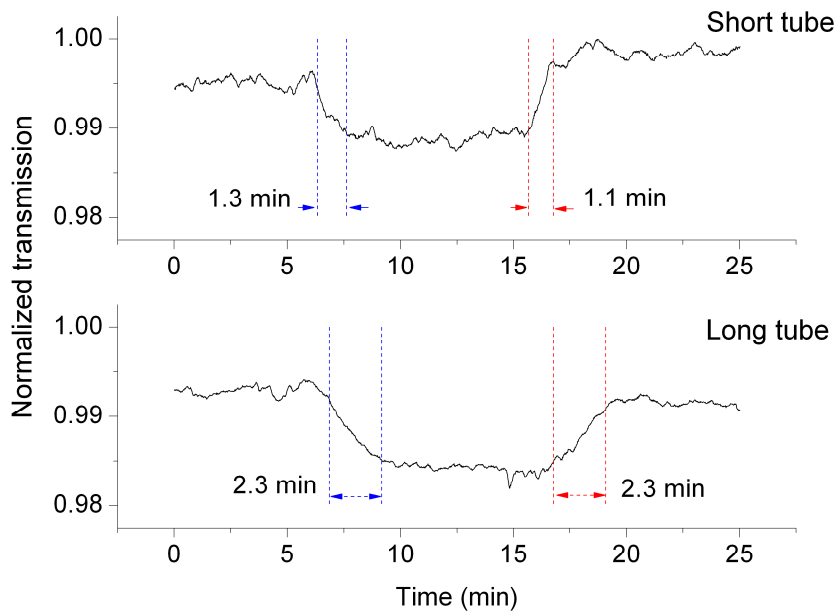


Figure 4.22 Response time of cocaine measurement: The response of the setup with a long ($\sim 20\text{cm}$) tube was slower than a short ($\sim 6\text{cm}$) one. The tube was installed between the device and the multi-selection valve for switching samples.

The slow response of the dynamic measurement was mainly due to the phenomena in the liquid chamber and the tubing. They included the length of the tube before the inlet of the device, and the mixing of two concentrations in the

microfluidic channels and tubes. To assess the response speed of the optical system only, we made a test without a microfluidic system on the waveguide.

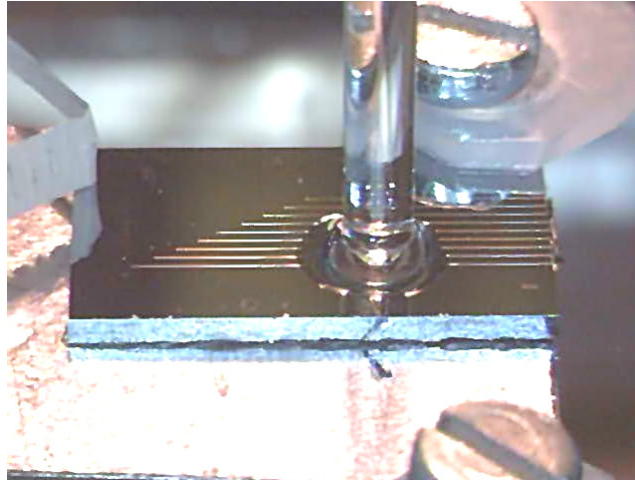


Figure 4.23 Image of the water drop test: A drop of water covered a part of the waveguide. The size of the drop could be controlled by the pipette dipped into the water.

We put a drop of de-ionized water on the Ge waveguide, and it covered a part of the waveguide as shown in figure 4.23. The tip of a glass pipette was immersed into the water drop without touching the waveguide. The size of the water drop could be controlled dynamically by the pipette, which was mechanically fixed on the optical table. Because water has strong absorption in the mid-IR, the transmittance of the waveguide changed while water covered a different length. As shown in figure 4.24, the waveguide output was measured in real time, while the drop size varied among 5 different levels. During each transition of levels, the response time was near 0.5 seconds, which was about the time for the water drop to change the shape and the size. This result demonstrated the fast response of the optical system, and showed the potential of this device to study dynamic phenomena in a microfluidic environment.

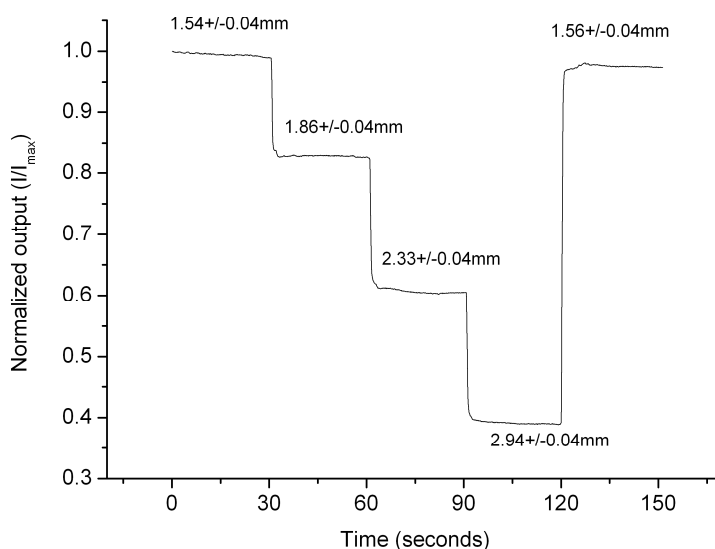


Figure 4.24. Dynamic measurement with a water drop: The waveguide output had a fast response to the water drop coverage. The response time of the switch between levels was only 0.5 seconds.

4.7 Effective path length of the waveguide evanescent field

The change of the transmittance is due to the absorption of water in the evanescent field. Therefore, the waveguide transmittance and the water-covered length follow the Beer-Lambert law. Figure 4.25 shows the normalized waveguide output plotted with the water coverage in a logarithm scale. A nice linear relationship could be found with a slope of -2.89 dB/mm. Because the absorbance of liquid water near 5.8 μm is about 672 cm^{-1} [71], we could determine an effective transmission path length, which has equivalent total absorption. For 1 mm of this Ge waveguide, the effective path length was 9.87 μm . When it was compared with conventional ATR elements, which normally have effective path lengths in the range of 1-30 μm at this wavelength, a Ge-on-Si waveguide could provide more than 10 times interaction volume, when the waveguide length was 30mm. This showed the potential of this device to be more sensitive to low concentration analytes than conventional ATR technologies. Furthermore, with the combination of higher power QCLs, and the development of waveguides with lower losses, the waveguide can be made longer and can reduce the detection limit to a lower level.

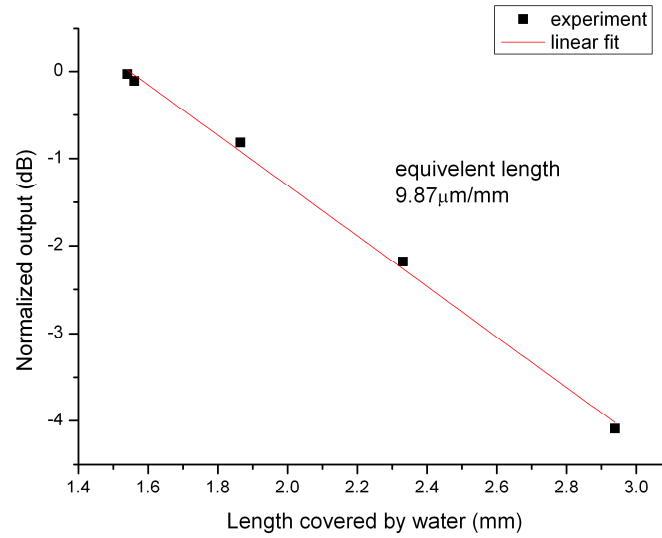


Figure 4.25 Transmittance with varied water coverage: A nice linear relation confirmed the Beer-Lambert law. The equivalent path length for 1mm waveguide is $9.87 \mu\text{m}$ at the wavelength of $5.8 \mu\text{m}$.

4.8 Reference waveguide and integrated Y splitters

For sensing devices based on the measurement of intensities or amplitudes, a reference signal is desirable, because many noises can be eliminated by differential measurements. As described in section 4.4, there are two main sources of noise in our cocaine detection system. The thermal fluctuation caused by Fabry-Perot fringes could be reduced to a low level with the methods described in section 4.5. Therefore, the other one, misalignment of the QCL and the waveguide, became the dominant noise source.

The QCL and the waveguide can shift from the best aligned position by mechanical vibrations or thermal expansions. Vibrations normally had higher frequencies and could be averaged by longer integration time. However, thermal expansions of elements in the measurement setup were dependent to the ambient temperature. It showed short-term fluctuations in the range of several minutes, and long-term drifts in the range of more than hours. The air flow and the temperature in the laboratory become crucial factors of the system stability.

Aluminum and steel are the two common materials for optical setups. They have linear thermal expansion coefficients about 23×10^{-6} and 12×10^{-6} respectively. Between the stage of QCL and the stage of the waveguide, if we consider a 10-cm asymmetry of the aluminum material, the alignment shift can be $2.3 \mu\text{m}$ for the temperature change of 1 degree. From figure 4.14, if the output intensity decreases with the QCL shift in a Gaussian shape, a misalignment of $2.3 \mu\text{m}$ can induce a transmission drop about 3.5%. This high sensitivity to the ambient temperature makes it difficult to maintain a stable measurement. To

improve the performance of our device for cocaine detection, we needed a reference signal to eliminate this noise.

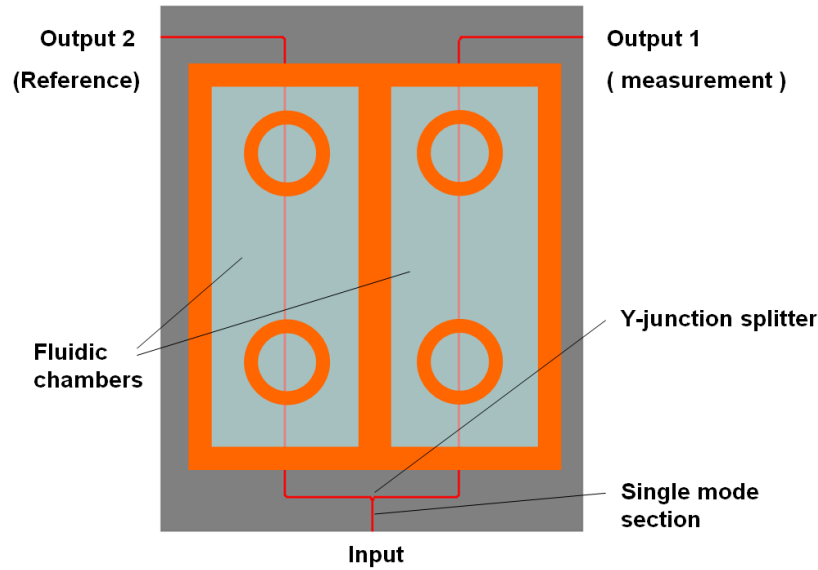


Figure 4.26 Design of a reference waveguide: After the input, the light was split by a Y-junction into two waveguides. The single mode section ensured a constant splitting ratio.

Figure 4.26 shows the design to eliminate the error induced by QCL coupling. The reference signal was from a waveguide, which shares the same input of light with the measuring waveguide. A Y-junction connected the two waveguides, and split the light beam from the input into two parts. Before the Y-junction splitter, it was important to have a section of singlemode waveguide in order to keep a constant splitting ratio. If it was a multimode waveguide, the splitting ratio could change with the coupling condition of the QCL, and the reference waveguide would lose its function. For Ge-on-Si strip waveguides, we made the width to be $2.9\text{ }\mu\text{m}$ to ensure singlemode propagation for the TM polarization at $5.8\text{ }\mu\text{m}$. After the splitter, the two waveguides went through two separate microfluidic chambers, and reached the edges of the substrate. The two output facets were on two opposite edges of the device to be accessible by two detectors.

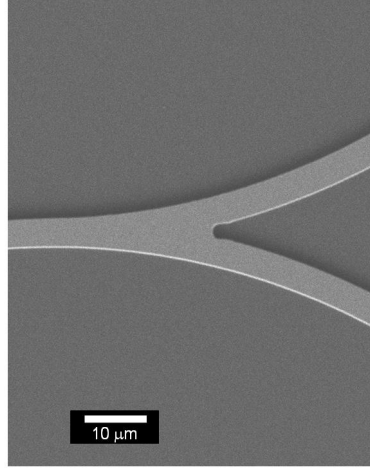


Figure 4.27 Scanning electron microscope image of a Y-junction splitter made from germanium on a silicon substrate.

Several ways can divide the injected light into two parts with a stable splitting ratio. They include directional couplers and multimode interference (MMI) devices. Directional couplers have higher requirement on the smallest feature size [52] of the fabrication technologies. Here we simply used a Y-junction splitter which had two branches after the junction. Figure 4.27 shows a SEM image of a Y-junction splitter made in Ge on Si substrate. The splitting ratio of the Y-junction was measured to be near 50/50, and the excess loss was approximately 3 dB.

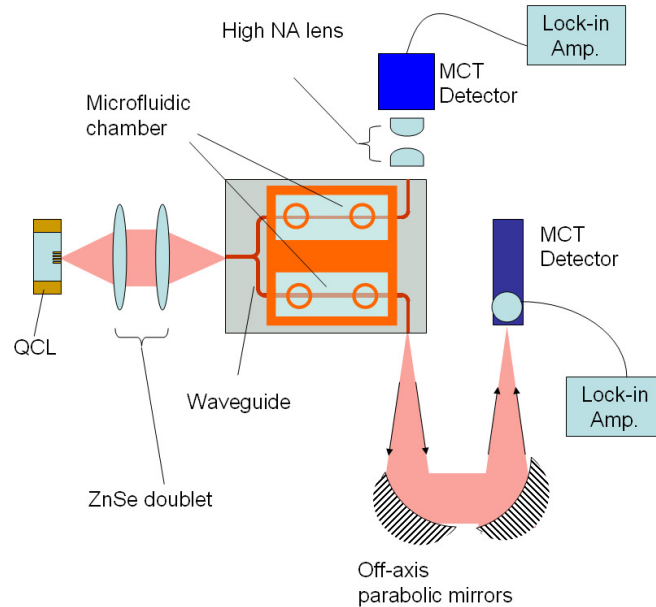


Figure 4.28 Setup for the measurement with a reference waveguide: An additional detector combined with 2 high NA lenses was coupled with the output facet of the reference waveguide.

The measurement setup was modified as figure 4.28 with the end-fire coupling configuration. The mechanical chopper was no longer needed, because the QCL was driven in a pulsed mode which provided modulated signals for the lock-in amplifiers. After the Y-splitter, the light was about equally divided into the two branches, which went through two separated microfluidic chambers. The two branches were bended to two opposite directions with two 90° bends, and coupled to two detectors. One detector was the liquid nitrogen cooled MCT detector with two off-axis parabolic mirrors, and the other was a room-temperature MCT detector from Vigo Systems combined with 2 high NA lenses. Both the two detectors were perpendicular to the emission axis of the QCL to avoid the on-axis noise from the stray light through the free space and the substrate.

The Si substrate was mechanical clamped on the stage with a stable temperature controlled in a 0.02 K range in room temperature. It was combined with a pulsed QCL source to suppress the thermal noise due to the Fabry-Perot fringes.

The performance of the reference waveguide was tested without injecting fluidic samples into the microfluidic channels, where the waveguides stayed in contact with air only. The light intensities of the two waveguide outputs were recorded simultaneously with an automated data acquisition for about 30 minutes. Figure 4.29 shows the normalized output intensities and the ratio of output 1 and output 2. Both the two outputs suffered similar fluctuations of several percents, and the noise could be eliminated by taking the ratio of the two. This test demonstrated the function of the reference waveguide, and the noise was reduced to a level that 3 times of the standard deviation is 0.172%.

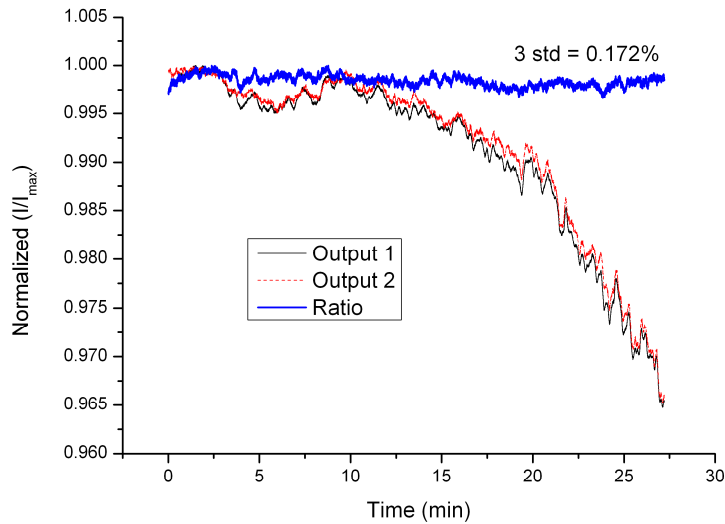


Figure 4.29 Measurement of the stability with a reference waveguide: The noises and drifts caused by QCL mis-alignment could be eliminated. 3 times of the standard deviation was 0.172% after taking the ratio of the two outputs.

4.9 Long waveguide for enhanced interaction

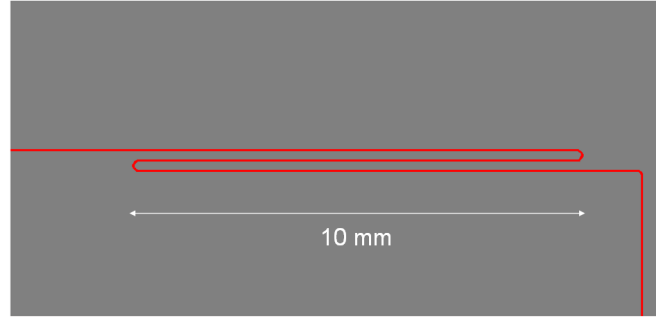


Figure 4.30 Design of a long waveguide: The waveguide had a meander shape and the length in the fluidic chamber for light-liquid interaction was about 30 mm.

Together with the noise reduction, we could enhance the performance of this device by increasing the signal level of cocaine absorption. For the same cocaine concentration in the evanescent field, one can increase the interaction volume with a longer waveguide. Consider a sensing system which has a limit of detection of cocaine at the concentration c , with a waveguide of length L . The contribution of the absorbance from the cocaine can be written as

$$A_l = acL \quad (e.q.4.6)$$

Here A_l is the smallest detectable absorbance difference of the system, and a is the absorbance of a unit concentration and a unit length. Here, a is dependant on the waveguide and the wavelength. When we increase the waveguide length to mL , the new detection limit of this system becomes

$$c_1 = \frac{A_l}{a(mL)} = \frac{c}{m} \quad (e.q.4.7)$$

The lowest detectable concentration decreases linearly with the increase of the waveguide length.

Figure 4.30 shows the design of a Ge-on-Si waveguide with a meander shape, and the length for the light-liquid interaction in the microfluidic chamber was about 30 mm. The meander design was based on the fact that the bending loss was measured to be only 0.12 dB for a 90° bend. It increased the total length of the waveguide, while the dimension of the substrate was kept the same. The radius of the bends was 115 μm , and the distance between two straight sections was 230 μm .

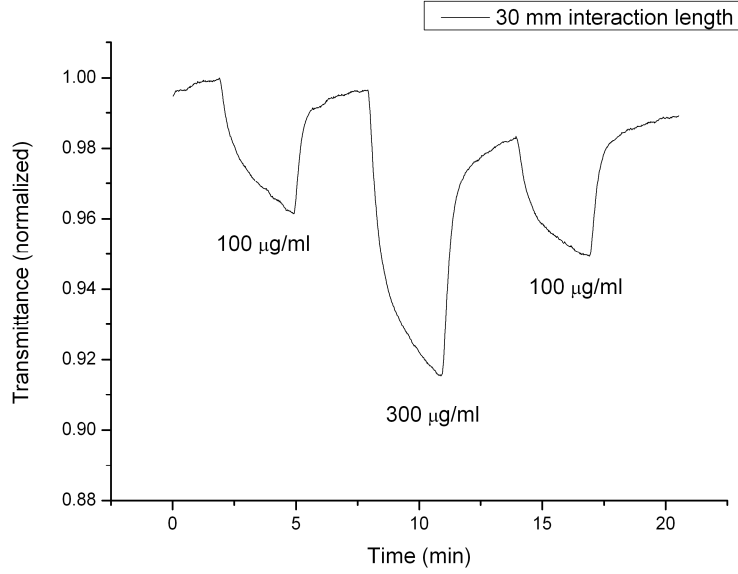


Figure 4.31 Measurement of cocaine with a 30 mm interaction length: The absorption was stronger and the drop of transmission was 3.4% for the cocaine concentration of 100µg/ml.

This long waveguide was used for cocaine detection with the setup in figure 4.28, but without a reference waveguide. We prepared cocaine in PCE solutions with the concentrations of 100 µg/ml and 300 µg/ml. The microfluidic channel was first filled with pure PCE with the flow rate of 50 µl/min. The concentration was then switched with a multi-selection valve, and between each switch we added several minutes of pure PCE as the reference level. As shown in figure 4.31, the transmittance drop during the flow of 100µg/ml was approximately 3.4%, which is the largest absorption we obtained here for this concentration.

If we combine the waveguide with 30 mm interaction length with a reference waveguide demonstrated in section 4.8, the limit of detection for this sensing system can be calculated as following. For the system with a reference waveguide, the noise is reduced to a level that 3 times of the standard deviation is 0.172%. For the waveguide with 30mm interaction length, the concentration of cocaine to absorb 0.172% of light can be calculated from

$$\frac{c_1}{c} = \frac{\log(t_1)}{\log(t)} \quad (e.q.4.8)$$

where c_1 and c are concentrations of cocaine solutions, and t_1 and t are the transmittance of the waveguide with the two concentrations respectively. Here the detection limit was calculated to be ~5 µg/ml, if the waveguide of 30mm interaction length is combined with a reference waveguide.

4.10 Varied waveguide width

Another method to increase the interaction volume is to enhance the evanescent field in a unit length of the waveguide, where the evanescent field contains high portion of light intensity. Here we made waveguides with different width from $1.2\ \mu\text{m}$ to $4.4\ \mu\text{m}$, and measured the effective path length with the water drop test.

Figure 4.32 shows the measured output intensity of waveguides with different widths. When the water drop covered a longer section, the waveguide output decreased with different slopes. For a narrower waveguide, a higher percentage of light was in the evanescent field, and therefore the output intensity decreased faster with increasing water coverage. Note that the data points were shifted vertically for the purpose of clarity. The lines were the linear fittings for each waveguide.

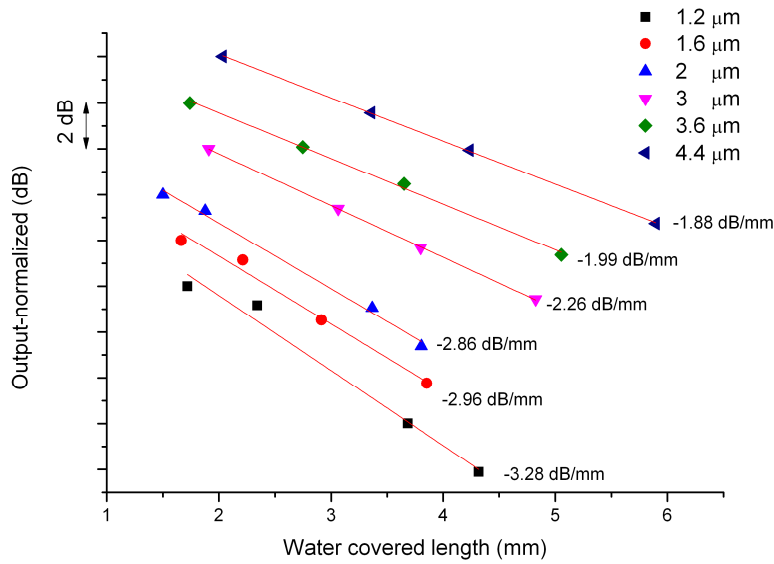


Figure 4.32 Water drop test on waveguides of different widths: Narrower waveguides showed a faster drop when the water coverage increased. The data points were shifted vertically for the purpose of clarity.

While a narrower waveguide showed a stronger evanescent field, the propagation loss also becomes larger. This was due to the increasing effects of the side wall roughness and the defects of the Ge layer near the interface with the Si substrate. We measured the propagation losses of each waveguide with the Fabry-Perot method, and plotted it with the effect path length for a unit length of waveguide, as shown in figure 4.33.

When the waveguide width reduced from $3\ \mu\text{m}$ to $1.2\ \mu\text{m}$, the effective path increased about 45%, while the propagation loss also increased 160%. Because the propagation loss increased 3-4 times faster than the effective path length, a narrower waveguide was not a better solution than a longer waveguide to enhance the interaction volume for this moment. When the propagation loss

can be reduced to a comparable level by using smoother side walls or a Ge layer with less defect, it may become a better method.

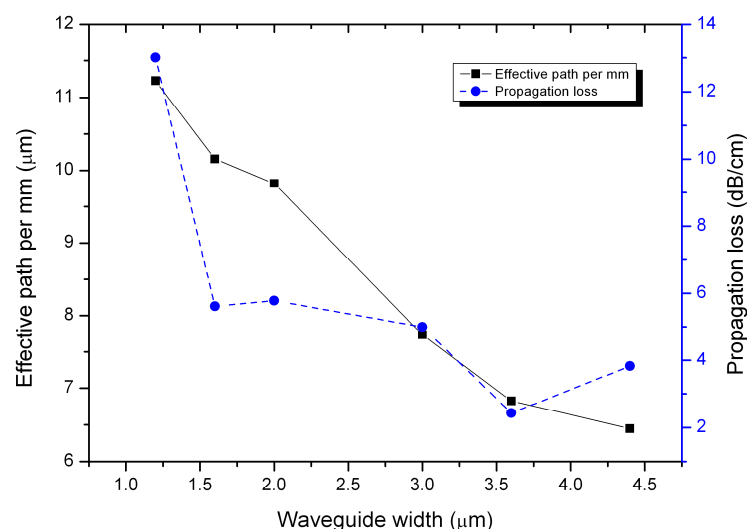


Figure 4.33 Effective path length and the propagation loss for waveguide of different widths: The propagation loss increased 3-4 times faster than the effective path length when the width decreased.

4.11 Outlook of sensitivity improvement

To further improve the sensitivity of this device, several approaches can be tested in the future. For noise reduction, integrated detectors would reduce the alignment fluctuation to the waveguides, and antireflection treatment of the waveguide facets would further reduce the noise from the Fabry-Perot resonance of each waveguide. If the measurement setup is integrated into a compact system, the easier temperature control would reduce the noises from thermal fluctuations.

For signal enhancement, the evanescent field of the waveguide could be enhanced with modifications on the waveguide designs, which include a thinner waveguide or a slot waveguide design [52]. Furthermore, the wavelength of the QCL could be tuned to the center of the absorption peak in order to have a larger absorbance. Besides, liquid-liquid extraction and pre-concentration of cocaine have been demonstrated with microfluidic systems [31]. With the combination of the above mentioned approaches, we could expect the detection limit to be improved to a practical level for the task of cocaine detection in human saliva.

Chapter 5

Outlook of Ge-on-Si mid IR photonics

Further development of Ge-on-Si based mid IR photonics was studied. This chapter presented a Mach-Zehnder interferometer integrated with a microfluidic system, and the investigation of antireflection treatments of the end facets of the waveguides by subwavelength structures.

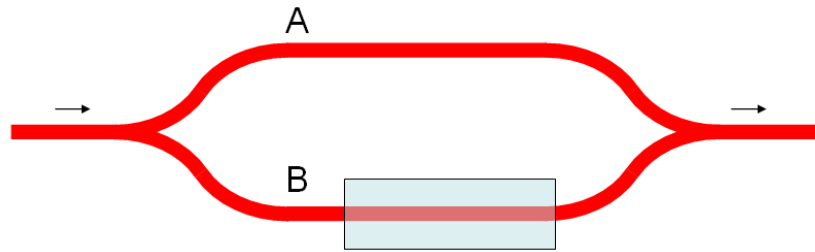
Starting from the needs for sensing applications in liquids, Ge-on-Si waveguides provide a powerful platform for more development of mid IR photonics in silicon. In combination with QCLs, these integrated elements show their potential in various other applications, including environmental monitoring, CMOS optoelectronic systems for spectroscopy [2], and astronomical uses.

5.1 Mach-Zehnder interferometer based on Ge-on-Si waveguide

By transferring the phase information of light waves into light intensity, a Mach-Zehnder interferometer (MZI) can be used as a sensor or a modulator. When a MZI is built with planar waveguides, it can be illustrated as shown in figure 5.1. The light beam is divided into two parts which travel through the two arms A and B. After combination into one waveguide, the output light intensity can be measured and shows the phase difference between them. The equation in figure 5.1 describes the relationship of the output intensity and the phase difference. Here I is the output, I_A and I_B are the intensities in the two arms, and $\Delta\phi$ is the phase difference. Depending on the materials of waveguides, the optical paths of the two arms are sensitive to temperature, electric field, and the refractive index of the cladding. The cladding material can be air, liquids, or solids.

A typical task of a MZI sensor is to measure the refractive index difference of the surrounding medium. In figure 5.1, a part of arm B is exposed to the test samples, which can be liquids containing target substances. While the refractive index of the surrounding medium is shifted by increasing target substance, the transmission spectrum of the MZI is changed. However, the

refractive index of the surrounding medium can be shifted by different substances. Therefore a functionalized layer on the waveguide surface is necessary to distinguish the effect of the target substance from others.



$$I = I_A + I_B + 2\sqrt{I_A I_B} \cdot \cos(\Delta\phi)$$

Figure 5.1 Illustration of a Mach-Zehnder interferometer for sensing applications

A functionalized layer is a recognition medium which can bind specific molecules of interest, and provide selectivity on the target substance over others [14,15]. Therefore a MZI sensor coated with a functionalized layer only responds to the target analytes. Some examples of these recognition medium are antibodies, nucleic acids, and polymers with molecular imprints. Because of the high affinity to the target molecules, these recognition medium usually can enhance the concentration of the molecules near the waveguide surface, and hence increase the phase change in the MZI sensor. In addition, if the test samples contain light absorbing molecules, which can reduce the signal level of the MZI, a functionalized layer can prevent the undesired absorbing molecules from entering the evanescent field and increase the output signal of the MZI.

5.1.1 Temperature actuated Mach-Zehnder interferometers

In the task of chemical sensing in liquid environments, a MZI sensor could be an alternative of the method based on mid IR spectroscopy. It has the potential to have a higher sensitivity with a functionalized layer.

To demonstrate a MZI on a Ge-on-Si platform, we designed the waveguide as presented in figure 5.2. In the 3 designs, 2 MZI had asymmetric arms with length difference of 2 mm and 4 mm separately. The splitters and combiners were simple Y-junctions as presented in section 4.6. The purpose of the asymmetric designs was to allow thermal actuation by varying the substrate temperature. The design of 2 different path differences was to demonstrate the sensitivity to temperature changes. In each MZI, after the combination of the two arms, a 90° bend allowed the detector to measure in the direction perpendicular to the QCL emission axis. This configuration avoided large amount of stray light going through the free space and the Si substrate, and increased the signal to noise ratio.

To maintain singlemode propagation, the width of the waveguides was 2.9 μm, and the thickness is 2 μm. In order to put 3 designs on the same substrate, the

splitters and combiners were designed at different positions in each MZI. Due to the limited chip size, some parts of these MZIs had small spacing from each other. Here the smallest distance between two waveguides was 40 μm , therefore they would not interfere with each other at the wavelength of 5.8 μm .

The asymmetric MZIs were designed to modulate the phase difference by the temperature of the substrate, because of the thermal-optical effect of Ge. With the setup shown in figure 3.13, we measured the output light intensity during temperature scanning. A tungsten coil near the waveguide with a narrow spacing heated up the substrate by increasing the current on the coil. Here the QCL was in continuous wave mode to maintain a sharp emission spectrum.

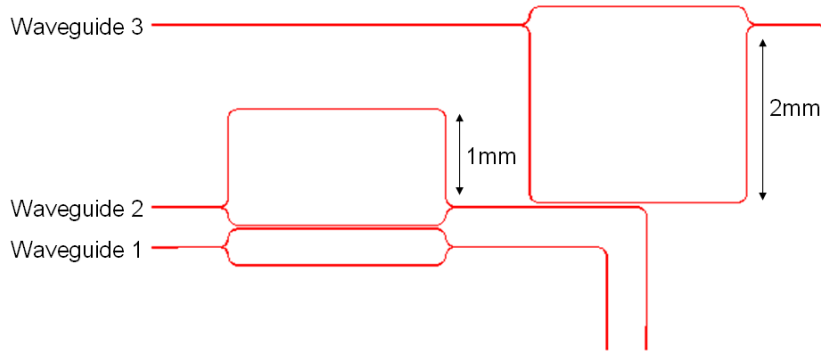


Figure 5.2 Design of asymmetric MZIs: The two arms of waveguide 2 and 3 have asymmetric lengths. Here the splitters and the combiners are Y-junctions. The shapes of the 3 MZIs were designed to fit into a limited size of the substrate.

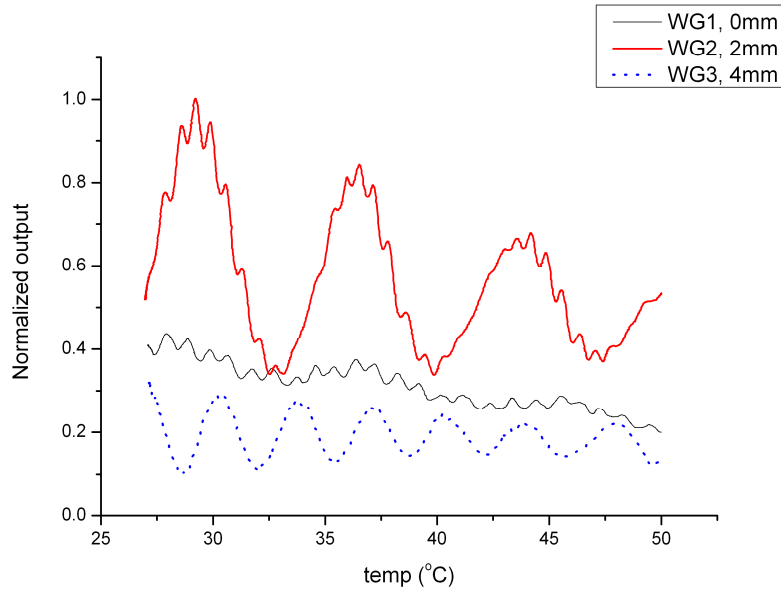


Figure 5.3 Output intensity of asymmetric MZI with temperature scanning: The two asymmetric MZI exhibited oscillating frequencies corresponding to the length differences.

The measurement results were shown in figure 5.3. For the MZIs of waveguide 2 and 3, the output light showed combinations of oscillating fringes from two different frequencies with temperature scanning. In each one of the two curves, there were one frequency corresponding to the Fabry-Perot resonance of the waveguide facets, and the other frequency corresponding to the path difference of the MZI. As described in section 3.5.2, the frequencies could be calculated by taking into account the thermal-optical effect and the thermal expansion effect of Ge. In MZI of waveguide 1, there was only the frequency 1.04 K^{-1} , which is in agreement with the Fabry-Perot resonance of the waveguide length 7.1 mm. In the MZI of waveguide 3, the slower frequency was 0.29 K^{-1} , which was in agreement with the asymmetry of waveguide path 4 mm. The relationship can be written as

$$f_{MZ} = \frac{a \cdot n_{eff} \cdot d}{\lambda} \quad (e.q.5.1)$$

where f_{MZ} was the frequency, a was the thermal-optical coefficient of the effective refractive of the waveguide, and d was the path difference. Here the thermal expansion effect was small and neglected. We could see the frequency was linearly proportional to the length difference, which was in agreement with the slower frequency in the MZI of waveguide 2, which was half of the one in waveguide 3. Due to the asymmetric designs, the extinction ratios of these MZI were relatively low, because the propagation losses of the waveguides were in the range of 3-5 dB/cm. Since the alignment was optimized at room temperature, the average output decreased with the increasing temperature due to the misalignment of thermal expansion of the mechanical elements in the setup.

This temperature driven MZI showed the feasibility of an integrated interferometer on the Ge-on-Si platform. Because it required the heating up of the whole substrate to modulate the output, this MZI was not suitable for applications which need high speed switching. For improvement, designs with a thin film heater over the waveguide may reduce the switching time to the level of tens of μs , and it allows symmetric MZI which has high extinction ratio and is less sensitive to temperature. The superposition of the Fabry-Perot resonance may induce noise, but it can be reduced by applying anti-reflection treatments, which will be discussed in the next section.

5.1.2 Mach-Zehnder interferometer integrated with microfluidics

MZI devices integrated with microfluidics have been used for bio-sensing applications in the visible wavelength on a silicon substrate [72]. Here we demonstrate a mid-IR MZI integrated with a microfluidic system on Ge-on-Si platform.

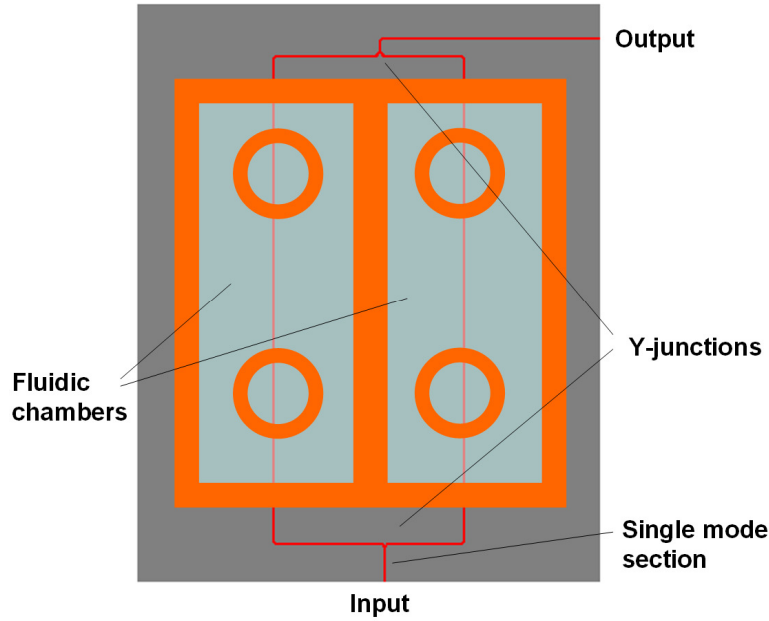


Figure 5.4 Scheme of a Mach-Zehnder interferometer integrated with a microfluidic chip: The two arms go through different microfluidic chambers. The liquid samples were switched in real time when the output is recorded.

As shown in figure 5.4, the two arms of the MZI go through two separated microfluidic chambers, which are 10 mm long, 1 mm wide and 50 μm high. Each chamber consists of one inlet and one outlet for liquid flows. The liquid samples can be switched with a multi-selection valve before the inlet. The microfluidic chip is fabricated with NOA81 by the same process described in chapter 4. The optical measurement setup is similar as in figure 3.13, in which the device is on a stage with temperature controlled in a range of 0.02 K. Figure 5.5 shows the image of the device integrated a Ge-on-Si MZI and a microfluidic chip.

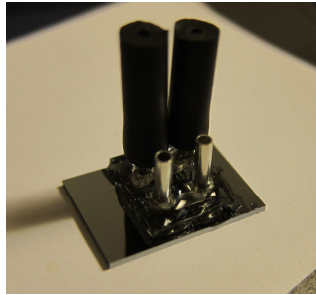


Figure 5.5 A photo image of the Ge-on-Si MZI integrated with a microfluidic system

Because the output signal of a MZI is a periodic function, the slope of output to the phase difference is close to zero, when it is near the maximum or the minimum. For a MZI sensor, it is important to work at the point of large slope, when a small phase difference needs to be detected. In this MZI, we added a 1.6 mm difference between the lengths of the two arms. When the waveguide

propagation loss is 3 dB/cm, this additional length decreases the intensity of one arm by 10%, but also allows us to tune the working point by changing the device temperature [73]. As shown in figure 5.6, the output curve of a MZI can be shifted by the temperature, in order to have a higher sensitivity at the working point. For a 1.6 mm difference of our Ge waveguide, a temperature shift of 2.08 K can move the curve for a quarter of the period.

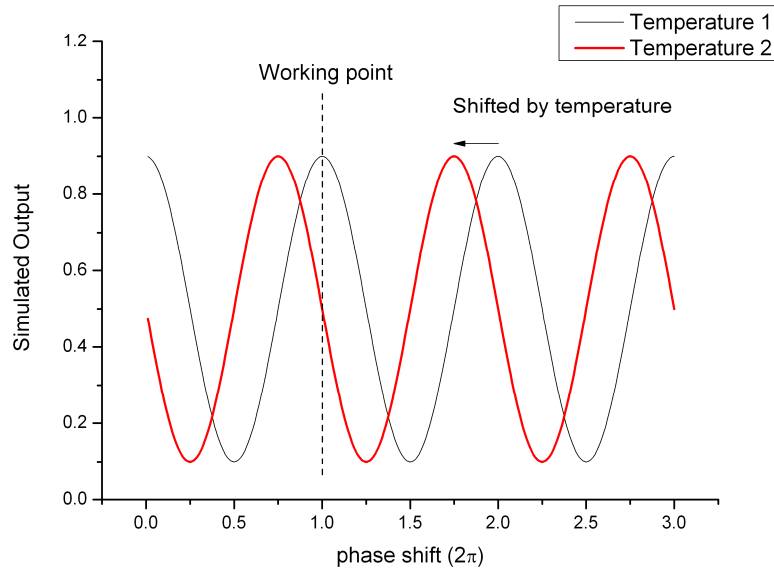


Figure 5.6 Simulated MZI output shifted by temperature: The asymmetric MZI allows a shift by changing the device temperature, in order to work at a high sensitivity region.

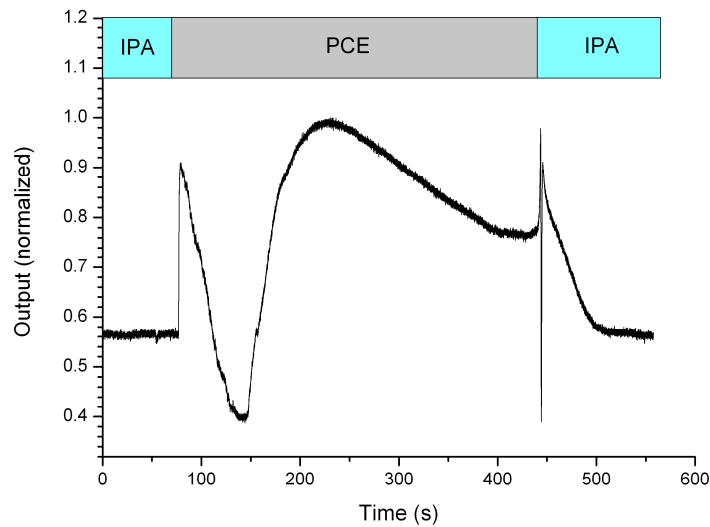


Figure 5.7 Measured MZI output with the liquid flows: One microfluidic channel flowed IPA and PCE. The refractive index of the cladding can be measured.

To demonstrate the sensing of the refractive index in the cladding with our device, we modulated the MZI by switching the liquid between isopropyl alcohol (IPA) and tetrachloroethylene (PCE), which have refractive indices around 1.36 and 1.47 respectively for the wavelength of 5.8 μm [74,75]. These two organic solvents both have low absorption near 5.8 μm .

We kept one of the microfluidic channels filled with only air, and first filled the other channel with IPA. A syringe pump sucked the liquids with a flow rate of 50 $\mu\text{L}/\text{min}$. During the measurement, the valve was switched between the reservoirs of IPA and PCE. As shown in figure 5.7, when the flow changed from IPA to PCE, the phase difference changed rapidly in the beginning and slowly stabilized after 5 minutes. The switch from PCE to IPA was nearly 5 times faster, and stabilized after 1 minute. The hydrophilic property of the waveguide surface was suspected to be a reason of the asymmetric response speeds.

From IPA to PCE, the phase change was 3π while the bulk index change was 0.11. The sensitivity of this device could be represented by the phase change corresponding to a unit refractive index change. It was 27.3π for this device, which was more than a magnitude lower than other MZI demonstrated in the visible wavelength range [76]. This was due to that the light was highly confined in the high refractive index core of the waveguide. To improve the sensitivity to index changes, the waveguide can be modified to allow more light in the surrounding material [52].

This result demonstrated the sensing of refractive index changes in liquids, with a Ge-on-Si MZI in combination of a microfluidic system. Further development can be the integration of a surface functionalized layer for sensing of specific molecules or proteins, which has been realized with Ge crystal for ATR-FTIR spectroscopy [77]. The development of waveguides with enhanced evanescent field can increase the sensitivity to the refractive index changes in the surrounding medium.

Comparing to a single waveguide for sensing based on spectroscopy, this MZI device has the potential to have a higher sensitivity. The use of a functionalized layer not only can enhance the concentration of the target molecules, it also has potential to prevent light absorbing molecules entering the evanescent field. In mid IR, this means that strong water absorption could be eliminate and the extraction of analytes from human fluids is no longer necessary. For this purpose, a highly confined field is desirable because the thickness of the functionalized layer could be thinner.

5.2 Antireflection for end-facets of Ge-on-Si waveguides

For integrated optical circuits, reflectivity at the interfaces of two materials is critical for various optical elements, including planar waveguides, distributed feedback lasers, and external cavity lasers. A low reflectivity is preferred for the coupling between two elements. However, materials like semiconductors usually have high refractive indices and the Fresnel reflection cannot be neglected. The refractive index of bulk Ge is around 4 in the mid-IR, and the end facets of our

Ge-on-Si waveguides have a high reflectivity of 34.2% at the wavelength of 5.8 μm . For the detection utilizing waveguides, a reduced reflectivity also leads to smaller fringe contrast of resonances which are often disturbing in a measurement system. In the waveguide spectroscopy applications, anti-reflection gives a higher transmittance, and the waveguide can be made longer to enhance the interaction volume for a better sensitivity.

5.2.1 Single quarter wave film

A general method to reduce the reflection is based on the deposition of thin films at the interface. The simplest design is a single layer with a thickness which has a phase retardation of a quarter of the wavelength [78]. As illustrated in figure 5.8, n_0 and n_s are the refractive indices of the air and the substrate. For the normal-incident light, when we choose a material which has a suitable refractive index, the reflection can be reduced to be lower than 1% near the designed wavelength.

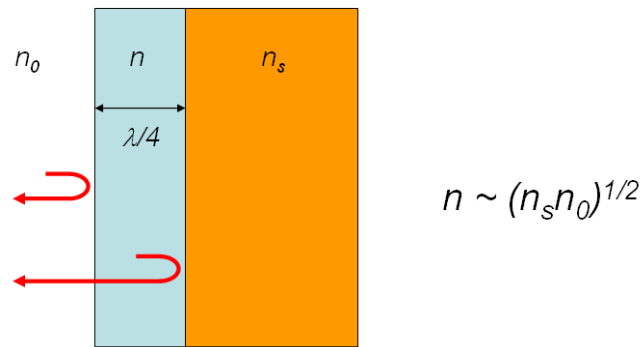


Figure 5.8 Illustration of a single film for antireflection: A thin film can reduce the reflection near the designed wavelength.

The refractive index of Ge is around 4. Therefore the material for a single layer anti-reflection film should have the refractive index near 2. Among common materials which are transparent in the mid-IR, we found ZnS (Zinc sulfide) and ZnSe (Zinc selenide) have refractive indices near 2.24 and 2.43 respectively.

On a bulk Ge wafer, we tested the anti-reflection property of a thin layer of ZnS, which was deposited with an e-beam thermal evaporation to the thickness of 700 nm. The transmission spectrum was then compared with a Ge wafer without the ZnS coating. Figure 5.9 shows the ratio of their transmittances measured with FTIR spectroscopy. An obvious anti-reflection effect in a wide range of spectrum could be seen. At the peak wavelength, the transmission of a Ge wafer without coating was about 65% of the sample with ZnS coating, which was in agreement with the estimated reflection of a Ge/air interface, 36%. The peak value in the curve was near 6.4 μm , considering the thickness of 700 nm, the refractive index of the coated ZnS layer could be calculated to be near 2.28.

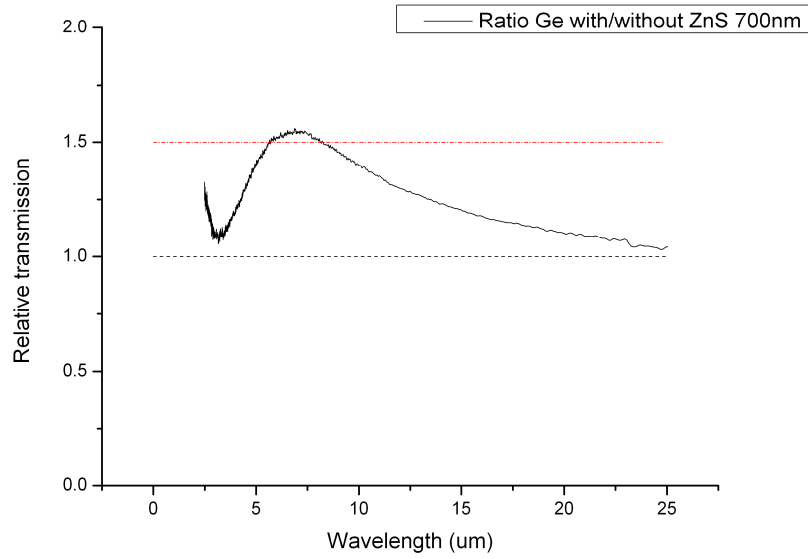


Figure 5.9 Transmittance ratio of Ge wafer with and without ZnS thin film: A 700nm ZnS film on a bulk Ge wafer enhanced the transmittance in a wide range of the mid-IR.

This test with a ZnS film on a bulk Ge wafer showed a good antireflection result in the mid IR. However, the ZnS film suffered the problem of weak adhesion on Ge and on Si surfaces. To improve this, further development can be the fabrication technologies of deposition on the waveguide facets. It may require an oblique evaporation technique and an intermediate layer for a good adhesion.

5.2.2 Subwavelength structures for antireflection

Another method to reduce the reflection is based on subwavelength structures on the reflecting surface. It has been demonstrated on the facets of SOI (silicon on insulator) waveguides with light of 1.55 μm wavelength [79]. In the mid-IR region, it has been used for the facets of QCLs with emission wavelength at 4.9 μm and 9.8 μm [80]. One advantage of this technology is less sensitive to the wavelength when the structure is designed to have gradient index over the thickness. In addition, for high power applications (e.g. laser cavities), structural antireflection treatment has no adhesion problems like thin films.

The design of the subwavelength structures can be simplified by using the effect medium theory (EMT). As illustrated in figure 5.10, consider a subwavelength grating structure, in which the refractive indices are n_s and n_0 for the two materials. The effective index is dependent on the polarization of the light. When the period d is much smaller than the wavelength, the effective indices can be approximated with the first order EMT as following [81]:

$$n_{\parallel} = (fn_s^2 + (1 - f)n_0^2)^{1/2} \quad (eq.5.2)$$

$$n_{\perp} = \left(\frac{f}{n_s^2} + \frac{(1 - f)}{n_0^2} \right)^{-1/2} \quad (eq.5.3)$$

Here the n_{\parallel} (n_{\perp}) is the effective index of light which has the polarization parallel (perpendicular) to the gratings, and f is the fill factor which is defined as w/d .

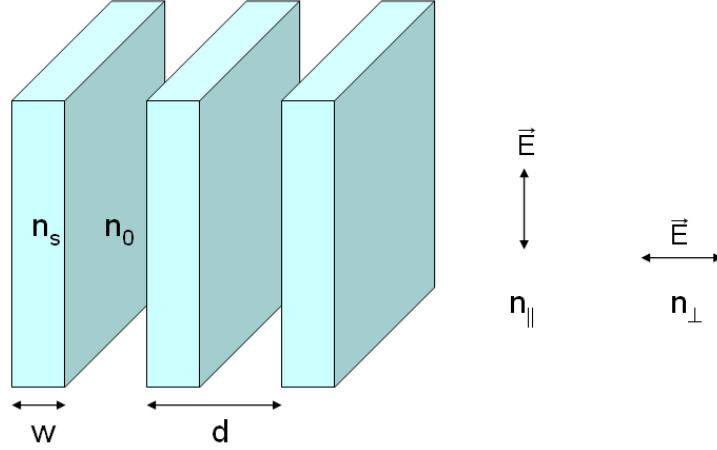


Figure 5.10 Illustration of subwavelength structures: The effective refractive index is polarization dependent and related to the filling factor.

Applying the single film design for anti-reflection, the optimized effective index is $(n_s n_0)^{1/2}$, and the thickness of the grating is a quarter wave of the wavelength in the medium.

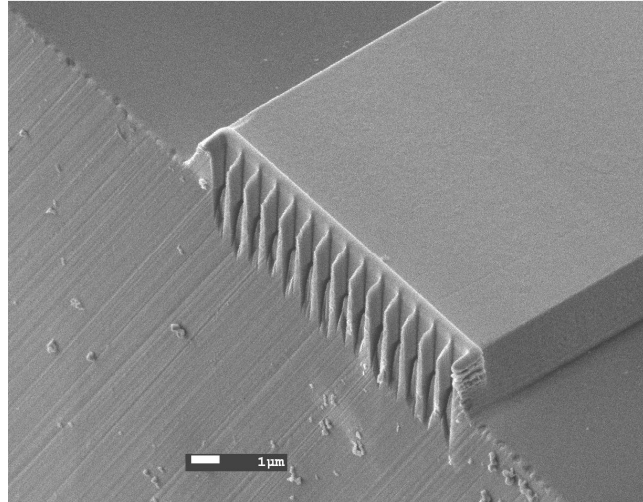


Figure 5.11 SEM image of subwavelength gratings on the waveguide facet: On the facet of a Ge-on-Si waveguide, we made gratings with FIB milling. A thin Pt layer avoided excess damage on the Ge material.

In our case of Ge-on-Si waveguides, we consider the TM polarization which was adapted to the QCL. For a structure which could be realized with dry etching process, we designed gratings which were parallel to the electric field. These gratings were designed to have period of $1\text{ }\mu\text{m}$ with the fill factor near 0.2, and the thickness of 725 nm into the direction of the waveguide axis.

As a quick test on these gratings, we used FIB (focus ion beam) milling to realize the structure directly on a waveguide. Ga ions struck on Ge and Si surface with energy of 30 KeV. To avoid excess damages on Ge, we put a thin layer of Pt as a protection on the milling area. Figure 5.11 shows the SEM image of the facet after structuring. We made the same structures on both facets of one waveguide.

The optical effect of the subwavelength gratings was tested with the Fabry-Perot resonance method, in which we measured the waveguide transmittance by varying the temperature. See section 3.5.1, as shown in equation 3.4, the resonance fringes are related to both the propagation loss and the reflectivity of the two facets. By comparing the fringes of the same waveguide before and after the FIB milling, we could measure the change of the reflectivity.

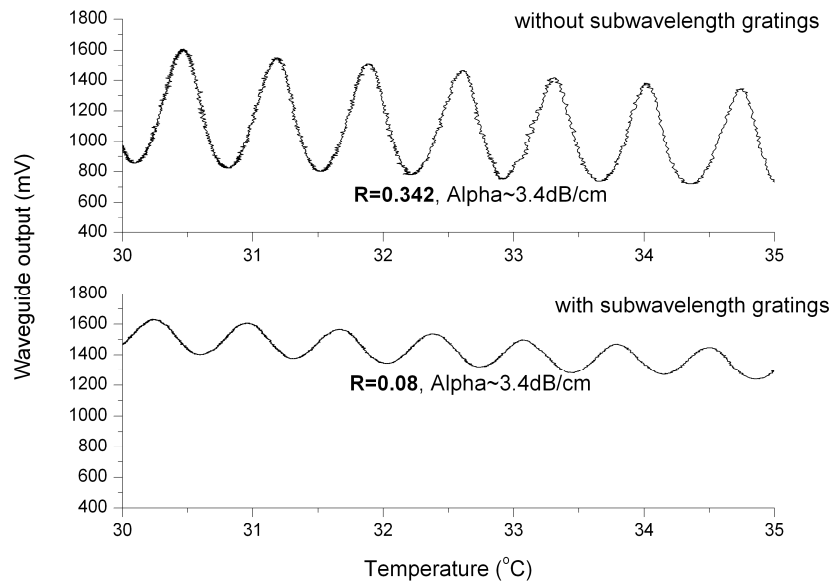


Figure 5.12 Fabry-Perot fringes before and after subwavelength structuring: The reflectivity decreased from 34.2% to 8%.

As shown in figure 5.12, the modulation depth of the Fabry-Perot fringes had an obvious drop after structuring the subwavelength gratings on the two facets. Assuming the propagation loss kept the same, we could determine the reflectivity reduced from 34.2% to 8%. However, the transmittance of the waveguide also decreased to 90%, when they were compared at the best aligned position. This additional loss could be attributed to the remaining of the Pt thin layer on the waveguide and the damages on the Ge material after FIB milling.

Further development of the subwavelength anti-reflection structures can be the improvement of FIB milling in order to remove the Pt protection layer. In addition, subwavelength structures can be fabricated in the same batch lithography as the Ge waveguide to avoid extra fabrication costs.

Chapter 6

Conclusion

This study aimed to develop a compact device for sensing in liquid environments with absorption spectroscopy in the evanescent field of a mid IR waveguide. The device was successfully realized with a Ge-on-Si waveguide integrated with a microfluidic chip, and demonstrated the detection of cocaine in tetrachloroethylene.

We demonstrated a singlemode mid-infrared strip waveguide based on a new combination of materials, monocrystalline germanium on silicon substrate, which had been proposed but not realized. These Ge-on-Si waveguides could be made with low propagation loss (<3 dB/cm) and low bending loss (0.12 dB per 90° bend). Besides the compatibility with Si technologies, both Ge and Si have large third order non-linearity. These properties make it a very good platform for further investigations of various mid-IR integrated devices, including couplers, interferometers, and resonators. In combination with QCLs which are high power, tunable, and compact, we can foresee a growing development base on this waveguide in the mid-IR photonics.

One important application for the light in the mid-IR spectrum is sensing of chemicals and biological substances. In this study, we integrated a Ge-on-Si strip waveguide with a microfluidic system, for the detection of cocaine in tetrachloroethylene. This device allows real time measurement of cocaine absorption in liquid environments, which shows the potential for studying dynamic phenomena in microfluidic environments. By adding a reference waveguide, the noise of the device was reduced to a level that 3 times of the standard deviation was 0.17%. With enhanced absorption of a longer waveguide, the limit of detection can be estimated to near $5 \mu\text{g/ml}$. When a tunable laser is used, this device can be used to probe a wider spectral range in the mid-IR. The

compact size of the device makes it ideal for the future development of a portable lab-on-chip system.

A Mach-Zehnder interferometer integrated with a microfluidic chip was also demonstrated here. Using Ge-on-Si waveguides, the MZI showed sensing of the refractive index changes of the surrounding medium in the mid-IR range. This result showed potentials of not only sensing, but also devices like optical switches and modulators.

Subwavelength structures were made on the facets of the Ge-on-Si waveguides for antireflection purpose. The measured reflectivity was reduced from 34.2% to 8%. Further improvement has chance to achieve a reflectivity below 1%.

Bibliography

- [1] J. Faist, F. Capasso, D. L. Sivco, C. Sirtori, A. L. Hutchinson, and A. Y. Cho, "Quantum Cascade Laser," *Science* **264**, 553–556 (1994).
- [2] R. Soref, "Mid-infrared photonics in silicon and germanium," *Nat Photon* **4**, 495–497 (2010).
- [3] P. Del’Haye, A. Schliesser, O. Arcizet, T. Wilken, R. Holzwarth, and T. J. Kippenberg, "Optical frequency comb generation from a monolithic microresonator," *Nature* **450**, 1214–1217 (2007).
- [4] K. M.-C. Hans, M. Gianella, and M. W. Sigrist, "Sensing cocaine in saliva with attenuated total reflection infrared (ATR-IR) spectroscopy combined with a one-step extraction method," in *proc. SPIE* **8229** (2012), p. 822919–822919–7.
- [5] X. Wang, S.-S. Kim, R. Roßbach, M. Jetter, P. Michler, and B. Mizaikoff, "Ultra-sensitive mid-infrared evanescent field sensors combining thin-film strip waveguides with quantum cascade lasers," *The Analyst* **137**, 2322 (2012).
- [6] S.-S. Kim, C. Young, and B. Mizaikoff, "Miniaturized mid-infrared sensor technologies," *Anal Bioanal Chem* **390**, 231–237 (2008).
- [7] C. Charlton, M. Giovannini, J. Faist, and B. Mizaikoff, "Fabrication and Characterization of Molecular Beam Epitaxy Grown Thin-Film GaAs Waveguides for Mid-Infrared Evanescent Field Chemical Sensing," *Analytical Chemistry* **78**, 4224–4227 (2006).
- [8] J. Hu, N. Carlie, N.-N. Feng, L. Petit, A. Agarwal, K. Richardson, and L. Kimerling, "Planar waveguide-coupled, high-index-contrast, high-Q resonators in chalcogenide glass for sensing," *Optics Letters* **33**, 2500 (2008).
- [9] K. Okamoto, "Fundamentals of Optical Waveguides", 2nd edition, Academic Press (2006)
- [10] F. Prieto, B. Sep lveda, A. Calle, A. Llobera, Dom ngezC, A. Abad, A. Montoya, and L. M. Lechuga, "An integrated optical interferometric nanodevice based on silicon technology for biosensor applications," *Nanotechnology* **14**, 907–912 (2003).
- [11] F. Vollmer, D. Braun, A. Libchaber, M. Khoshsima, I. Teraoka, and S. Arnold, "Protein detection by optical shift of a resonant microcavity," *Applied Physics Letters* **80**, 4057 (2002).
- [12] K. Tiefenthaler and W. Lukosz, "Integrated optical switches and gas sensors," *Optics Letters* **9**, 137 (1984).
- [13] J. Homola, S. S. Yee, and G. Gauglitz, "Surface plasmon resonance sensors: review," *Sensors and Actuators B: Chemical* **54**, 3–15 (1999).

- [14] M. N. Stojanovic, P. de Prada, and D. W. Landry, "Aptamer-Based Folding Fluorescent Sensor for Cocaine," *Journal of the American Chemical Society* **123**, 4928–4931 (2001).
- [15] B. Mizaikoff, R. Göbel, R. Krska, K. Taga, R. Kellner, M. Tacke, and A. Katzir, "Infrared fiber-optical chemical sensors with reactive surface coatings," *Sensors and Actuators B: Chemical* **29**, 58–63 (1995).
- [16] N. Harrick, "Study of Physics and Chemistry of Surfaces from Frustrated Total Internal Reflections," *Physical Review Letters* **4**, 224–226 (1960).
- [17] J. Fahrenfort, "Attenuated total reflectionA new principle for the production of useful infra-red reflection spectra of organic compounds," *Spectrochimica Acta* **17**, 698–709 (1961).
- [18] L. A. Averett, P. R. Griffiths, and K. Nishikida, "Effective Path Length in Attenuated Total Reflection Spectroscopy," *Analytical Chemistry* **80**, 3045–3049 (2008).
- [19] J. T. Bradshaw, S. B. Mendes, and S. S. Saavedra, "Planar Integrated Optical Waveguide Spectroscopy," *Analytical Chemistry* **77**, 28 A–36 A (2005).
- [20] M. Brandstetter, A. Genner, K. Anic, and B. Lendl, "Tunable external cavity quantum cascade laser for the simultaneous determination of glucose and lactate in aqueous phase," *The Analyst* **135**, 3260 (2010).
- [21] J. Faist, C. Gmachl, F. Capasso, C. Sirtori, D. L. Sivco, J. N. Baillargeon, and A. Y. Cho, "Distributed feedback quantum cascade lasers," *Applied Physics Letters* **70**, 2670 (1997).
- [22] J. M. Chalmers, "Mid-Infrared Spectroscopy of the Condensed Phase," in *Handbook of Vibrational Spectroscopy*, J. M. Chalmers, P. R. Griffiths, and J. M. Chalmers, eds. (John Wiley & Sons, Ltd, 2006).
- [23] N. J. Everall, "Raman Spectroscopy of the Condensed Phase," in *Handbook of Vibrational Spectroscopy*, J. M. Chalmers, P. R. Griffiths, and J. M. Chalmers, eds. (John Wiley & Sons, Ltd, 2006).
- [24] A. Hugi, R. Maulini, and J. Faist, "External cavity quantum cascade laser," *Semiconductor Science and Technology* **25**, 083001 (2010).
- [25] M. Haberkorn, J. Frank, M. Harasek, J. Nilsson, T. Laurell, and B. Lendl, "Flow-Through Picoliter Dispenser: A New Approach for Solvent Elimination in FT-IR Spectroscopy," *Applied Spectroscopy* **56**, 902–908 (2002).
- [26] Edelmann, J. Diewok, J. R. Baena, and B. Lendl, "High-performance liquid chromatography with diamond ATR-FTIR detection for the determination of carbohydrates, alcohols and organic acids in red wine," *Anal Bioanal Chem* **376**, 92–97 (2003).

- [27] Lendl, J. Frank, R. Schindler, A. Müller, M. Beck, and J. Faist, "Mid-Infrared Quantum Cascade Lasers for Flow Injection Analysis," *Analytical Chemistry* **72**, 1645–1648 (2000).
- [28] J. Hu, V. Tarasov, A. Agarwal, L. Kimerling, N. Carlie, L. Petit, and K. Richardson, "Fabrication and testing of planar chalcogenide waveguide integrated microfluidic sensor," *Opt Express* **15**, 2307–2314 (2007).
- [29] J. Dostálek, J. Čtyroký, J. Homola, E. Brynda, M. Skalský, P. Nekvindová, J. Špírková, J. Škvor, and J. Schröfel, "Surface plasmon resonance biosensor based on integrated optical waveguide," *Sensors and Actuators B: Chemical* **76**, 8–12 (2001).
- [30] Y.-C. Chang, P. Wägli, V. Paeder, A. Homsy, L. Hvozdar, P. van der Wal, J. Di Francesco, N. F. de Rooij, and H. Peter Herzig, "Cocaine detection by a mid-infrared waveguide integrated with a microfluidic chip," *Lab on a Chip* **12**, 3020 (2012).
- [31] P. Waegli, Y.-C. Chang, P. D. van derWal, L. Hvozdar, A. Homsy, H. P. Herzig, N. F. de Rooij, Droplet-based liquid–liquid extraction and on-chip IR-waveguide-spectroscopy detection of cocaine in human saliva, accepted for oral presentation at mTAS-Conference 2012, Okinawa, Japan.
- [32] NIST Chemistry WebBook, <http://webbook.nist.gov/chemistry>
- [33] R. A. Soref, S. J. Emelett, and W. R. Buchwald, "Silicon waveguided components for the long-wave infrared region," *Journal of Optics A: Pure and Applied Optics* **8**, 840–848 (2006).
- [34] A Sa'ar, F. Moser, S. Akselrod, and A. Katzir, "Infrared optical properties of polycrystalline silver halide fibers," *Applied Physics Letters* **49**, 305 (1986).
- [35] Paiss, "Core-clad silver halide fibers for CO₂ laser power transmission," in *Proceedings of SPIE* (1991), pp. 141–148.
- [36] Y. Raichlin and A. Katzir, "Fiber-optic evanescent wave spectroscopy in the middle infrared," *Appl Spectrosc* **62**, 55A–72A (2008).
- [37] O. Eyal, V. Scharf, S. Shalem, and A. Katzir, "Single-mode mid-infrared silver halide planar waveguides," *Optics Letters* **21**, 1147 (1996).
- [38] T. Lewi and A. Katzir, "Silver halide single-mode strip waveguides for the mid-infrared," *Optics Letters* **37**, 2733 (2012).
- [39] B. Dekel and A. Katzir, "Silver halide planar waveguides and grating couplers for middle infrared integrated optics," *Applied Physics Letters* **97**, 241106 (2010).
- [40] Benjamin J. Eggleton, Barry Luther-Davies, and Kathlenn Richardson, "Chalcogenide photonics," *Nature Photonics* **5**, 141–148 (2011)

- [41] T. Baehr-Jones, A. Spott, R. Ilic, A. Spott, B. Penkov, W. Asher, and M. Hochberg, "Silicon-on-sapphire integrated waveguides for the mid-infrared," *Opt. Express* **18**, 12127 (2010).
- [42] F. Li, S. D. Jackson, C. Grillet, E. Magi, D. Hudson, S. J. Madden, Y. Moghe, C. O'Brien, A. Read, S. G. Duvall, P. Atanackovic, B. J. Eggleton, and D. J. Moss, "Low propagation loss silicon-on-sapphire waveguides for the mid-infrared," *Optics Express* **19**, 15212 (2011).
- [43] S. E. Plunkett, S. Propst, and M. S. Braiman, "Supported planar germanium waveguides for infrared evanescent-wave sensing," *Applied Optics* **36**, 4055 (1997).
- [44] J. Vongsvivut, J. Fernandez, S. Ekgasit, and M. S. Braiman, "Characterization of Supported Cylinder–Planar Germanium Waveguide Sensors with Synchrotron Infrared Radiation," *Applied Spectroscopy* **58**, 143–151 (2004).
- [45] W. S. C. Chang and K. W. Loh, "Experimental Observation of 106- μ m Guided Waves in Ge Thin Films," *Applied Optics* **10**, 2361 (1971).
- [46] P. Mehta, M. Krishnamurthi, N. Healy, N. F. Baril, J. R. Sparks, P. J. A. Sazio, V. Gopalan, J. V. Badding, and A. C. Peacock, "Mid-infrared transmission properties of amorphous germanium optical fibers," *Applied Physics Letters* **97**, 071117 (2010).
- [47] J. Fan and P. K. Chu, "Group IV Nanoparticles: Synthesis, Properties, and Biological Applications," *Small* **6**, 2080–2098 (2010).
- [48] J. Liu, X. Sun, R. Camacho-Aguilera, L. C. Kimerling, and J. Michel, "Ge-on-Si laser operating at room temperature," *Optics Letters* **35**, 679 (2010).
- [49] J. M. Hartmann, A. Abbadie, N. Cherkashin, H. Grampeix, and L. Clavelier, "Epitaxial growth of Ge thick layers on nominal and 6° off Si(0 0 1); Ge surface passivation by Si," *Semiconductor Science and Technology* **24**, 055002 (2009).
- [50] Marc J. Madou, *Fundamentals of Microfabrication: The Science of Miniaturization* 2nd edition, Taylor & Francis, 2002
- [51] G. S. Oehrlein, "Selective Dry Etching of Germanium with Respect to Silicon and Vice Versa," *Journal of The Electrochemical Society* **138**, 1443 (1991).
- [52] T. Fujisawa and M. Koshiba, "Polarization-independent optical directional coupler based on slot waveguides," *Optics Letters* **31**, 56 (2006).
- [53] Robert G. Hunsperger, "Integrated Optics: Theory and Technology," 6th edition, Springer, 2009
- [54] G. Tittelbach, B. Richter, and W. Karthe, "Comparison of three transmission methods for integrated optical waveguide propagation loss measurement,"

- Pure and Applied Optics: Journal of the European Optical Society Part A **2**, 683–700 (1993).
- [55] J. Buus, "Analytical approximation for the reflectivity of DH lasers," IEEE Journal of Quantum Electronics **17**, 2256–2257 (1981).
 - [56] H. H. Li, "Refractive index of silicon and germanium and its wavelength and temperature derivatives," Journal of Physical and Chemical Reference Data **9**, 561 (1980).
 - [57] J. Kuligowski, G. Quintas, M. de la Guardia, and B. Lendl, "Analytical potential of mid-infrared detection in capillary electrophoresis and liquid chromatography: A review," Analytica Chimica Acta **679**, 31–42 (2010).
 - [58] S. Kulka, G. Quintas, and B. Lendl, "Automated sample preparation and analysis using a sequential-injection?capillary electrophoresis (SI-CE) interface," The Analyst **131**, 739 (2006).
 - [59] S. Kulka, G. Quintas, and B. Lendl, "On-line capillary electrophoresis FTIR detection for the separation and characterization of proteins," Vibrational Spectroscopy **42**, 392–396 (2006).
 - [60] <http://www.quantared.com>
 - [61] G. M. Whitesides, "The origins and the future of microfluidics," Nature **442**, 368–373 (2006).
 - [62] J. N. Lee, C. Park, and G. M. Whitesides, "Solvent Compatibility of Poly(dimethylsiloxane)-Based Microfluidic Devices," Analytical Chemistry **75**, 6544–6554 (2003).
 - [63] P. Wägli, A. Homsy, and N. F. de Rooij, "Norland optical adhesive (NOA81) microchannels with adjustable wetting behavior and high chemical resistance against a range of mid-infrared-transparent organic solvents," Sensors and Actuators B: Chemical **156**, 994–1001 (2011).
 - [64] L.-H. Hung, R. Lin, and A. P. Lee, "Rapid microfabrication of solvent-resistant biocompatible microfluidic devices," Lab on a Chip **8**, 983 (2008).
 - [65] A. Homsy, P. D. van der Wal, W. Doll, R. Schaller, S. Korsatko, M. Ratzer, M. Ellmerer, T. R. Pieber, A. Nicol, and N. F. de Rooij, "Development and validation of a low cost blood filtration element separating plasma from undiluted whole blood," Biomicrofluidics **6**, 012804 (2012).
 - [66] P. Wägli, A. Homsy and N. F. de Rooij, "UV-Curable Adhesive as the Low-Cost Material of Choice for Microfluidic Forensic Applications" Proceedings International Meeting on Chemical Sensors (IMCS), Nuremberg, Germany, p.1166-1168 (2012)
 - [67] D. Bartolo, G. Degré, P. Nghe, and V. Studer, "Microfluidic stickers," Lab on a Chip **8**, 274 (2008).

- [68] G. Wysocki, R. F. Curl, F. K. Tittel, R. Maulini, J. M. Bulliard, and J. Faist, "Widely tunable mode-hop free external cavity quantum cascade laser for high resolution spectroscopic applications," *Applied Physics B* **81**, 769–777 (2005).
- [69] J. Faist, C. Gmachl, F. Capasso, C. Sirtori, D. L. Sivco, J. N. Baillargeon, and A. Y. Cho, "Distributed feedback quantum cascade lasers," *Applied Physics Letters* **70**, 2670 (1997).
- [70] D. Hofstetter, M. Beck, J. Faist, M. Nägele, and M. W. Sigrist, "Photoacoustic spectroscopy with quantum cascade distributed-feedback lasers," *Optics Letters* **26**, 887 (2001).
- [71] Edward D. Palik, "Handbook of optical constants of solids" Academic Press, 1st edition, 1997
- [72] F. Prieto, B. Sep lveda, A. Calle, A. Llobera, Dom nguezC, A. Abad, A. Montoya, and L. M. Lechuga, "An integrated optical interferometric nanodevice based on silicon technology for biosensor applications," *Nanotechnology* **14**, 907–912 (2003).
- [73] David R. Huber, "Method for linearizing an unbalanced Mach Zehnder optical frequency discriminator", US patent 5373389, (1994)
- [74] R. E. Kagarise, "Infrared Dispersion of Some Organic Liquids," *Journal of the Optical Society of America* **50**, 36 (1960).
- [75] C. S.-C. Yang, B. R. Williams, M. S. Hulet, T. E. Tiwald, R. W. Miles, Jr., and A. C. Samuels, "Optical constants of neat liquid-chemical warfare agents and related materials measured by infrared spectroscopic ellipsometry," in (2011), p. 80180M–80180M–8.
- [76] B. J. Luff, J. S. Wilkinson, J. Piehler, U. Hollenbach, J. Ingenhoff, and N. Fabricius, "Integrated optical Mach-Zehnder biosensor," *Journal of Lightwave Technology* **16**, 583–592 (1998).
- [77] S. Devouge, J. Conti, A. Goldsztein, E. Gosselin, A. Brans, M. Voué, J. De Coninck, F. Homblé, E. Goormaghtigh, and J. Marchand-Brynaert, "Surface functionalization of germanium ATR devices for use in FTIR-biosensors," *Journal of Colloid and Interface Science* **332**, 408–415 (2009).
- [78] H. A. Macleod, *Thin-film Optical Filters* (Institute of Physics Pub., 2001).
- [79] J. H. Schmid, P. Cheben, S. Janz, J. Lapointe, E. Post, and D.-X. Xu, "Gradient-index antireflective subwavelength structures for planar waveguide facets," *Optics Letters* **32**, 1794 (2007).
- [80] A. O. Dirisu, G. Silva, Z. Liu, C. F. Gmachl, F. J. Towner, J. Bruno, and D. L. Sivco, "Reduction of Facet Reflectivity of Quantum-Cascade Lasers With Subwavelength Gratings," *IEEE Photonics Technology Letters* **19**, 221–223 (2007).

- [81] R. Bräuer and O. Bryngdahl, "Design of antireflection gratings with approximate and rigorous methods," *Applied Optics* **33**, 7875 (1994).
- [82] A. J. Jenkins, J. M. Oyler, and E. J. Cone, "Comparison of heroin and cocaine concentrations in saliva with concentrations in blood and plasma," *J Anal Toxicol* **19**, 359–374 (1995).

Acknowledgements

First of all, I want to thank my thesis advisor, Prof. Hans Peter Herzig, who gave me the opportunity to work in his group. He is always ready to answer questions and shows great patience to his students.

I would like to thank the jury: Prof. Nico de Rooij, Prof. Bernhard Lendl, Prof. Markus Sigrist, and Dr. Lorenzo Sirigu for their critical reviews on my thesis.

I wish to thank Dr. Lubos Hvozدارa, for his supervision on the project and the full support in the laboratories. From him, I have learned important experimental skills in the clean room, in the machine shop, and in the mid IR optics. He is full of passions for helping people, in all kind of circumstances.

I want to thank Dr. Lorenzo Sirigu for his supervision in the early stage of my study in Neuchâtel. He led me into the field of optical sensors.

I am grateful to Prof. Wataru Nakagawa for the discussions on issues from both the work and the life.

I was lucky to have the excellent microfluidic chips made by Philip Wägli, who gave me a complete support on the fluidic measurements. These experiments could not be made without him. I especially thank Philip for his continuous help until the last minutes.

I want to thank Dr. Alexandra Homsy for the nice collaboration in the project and the critical review of the co-authored paper.

Dr. Vincent Paeder and I shared the same office in the last years. I wish to thank him for the important simulation part of the project, and the various techniques he taught me for farm works.

I would like to thank Marcel Groccia, Libo Yu, Irène Philipoussis Fernandez, and Joab Di Francesco for their support on the electronics, the software, and the fabrication parts of the experiments.

I also like to thank Sylvain Dunand and Joffrey Pernollet for the fabrication of the antireflection films and nano-structures.

I would like to thank Dr. Yargo Bonetti, Prof. Daniel Hofstetter, and Kerstin Hans for the support in the IRSens project of Nano-Tera.

I am grateful to Dr. Valeria Musi and Dr. Jose Dintinger for the abstract in French. The encouraging words and ice creams from Valeria were especially important.

I want to thank Armando Cosentino, one of my best friends in Switzerland, for the friendship and the time we spent together in CMI, in the SEM room, and in the cafeteria. We were the team of E-beam fabrication.

I want to thank my colleagues: Qing Tan, Sara Santi, Eric Logean, Tristan Sfez, Pierre-Yves Baroni, Myun-Sik Kim, Matthieu Roussey, Gerben Boer, Hicham Farah, Patrick Ruffieux, Olivier Scherler, Toralf Sharf, Houda Sellame, Laura Chantada Santodomingo, Julie Lenoble Zwahlen, Roland Bitterli, Ali Naqavi, and Gael Osowiecki, for the friendly environment they build.

Many thanks to Brigitte Khan, Mary-Claude Gauteaub, Sandrine Piffaretti for their help on the administrative affairs for my stay in Switzerland.

I also like to thank all my friends in Neuchâtel for their friendship and the time we shared.

Particularly, I want to express my gratitude to my grand parents and my parents for their long-term support of my study in Taiwan and in Switzerland.

Finally, I want to thank Chau, my wife, for always being beside me and giving me support on my study. Her Vietnamese cuisine gives me energy to overcome challenges and go further.

Curriculum vitae

Yu-Chi CHANG
Chemin des Liserons 2
2000 Neuchatel
Switzerland
Tel : +41 78 901 9379
Year of birth : 1976

Education & working experience

- 2007-2012 Doctoral Assistant in Optics & Photonics Technology
Laboratory, Institute of Micro-engineering (IMT), EPFL,
Switzerland.
- 2002-2006 Engineer, TPO Display Corp.
(A Toppoly and Philips display company), Taiwan
- 2000-2002 Master of Science in Optical Sciences at National Central
University, Jhongli, Taiwan
- 1994-1998 Bachelor of Science in Physics at National Taiwan
University, Taipei, Taiwan

Publications

- Yu Chi Chang, V. Paeder, L. Hvozdar, J.-M. Hartmann, and H. P. Herzig, "Low-loss germanium strip waveguides on silicon for the mid-infrared," *Optics Letters* **37**, 2883 (2012).
- Yu Chi Chang, P. Wägli, V. Paeder, A. Homsy, L. Hvozdar, P. van der Wal, J. Di Francesco, N. F. de Rooij, and H. Peter Herzig, "Cocaine detection by a mid-infrared waveguide integrated with a microfluidic chip," *Lab on a Chip* **12**, 3020 (2012).
- P.-Y. Baroni, V. Paeder, Yu Chi Chang, M. Roussey and H. P. Herzig et al., "Demonstration of superprism effect in silicon pillar 2-D photonic crystal infiltrated with liquid crystals," *Optical Engineering*, vol. 50, num. 1, p. 014601, (2011).
- Yu Chi Chang, V. Paeder, L. Hvozdar, P. Wägli and A. Homsy et al. Mid-infrared Waveguide Evanescent Field Chemical Sensor for Liquids. *Conference on Lasers and Electro Optics - European Quantum Electronics Conference, CLEO Europe 2011, Munich, Germany, 2011*.
- Yu Chi Chang, V. Paeder, J.-M. Hartmann, P. Wägli and A. Homsy et al. Single Mode Mid-infrared Waveguide for Evanescent Sensor Scheme in Liquids. *6th International Conference on Microtechnologies in Medicine and Biology (MMB 2011), Lucerne, Switzerland, 2011*.

- Yu Chi Chang, H. T. Tien, C. D. Sung, C. C. Lee, C. M. Wang, and J. Y. Chang, “A Micropolarizer Fabricated from CaCO₃ by Anisotropic Wet Etching”, *Appl. Opt.* **42**, 4423 (2003)
- C. M. Wang, Yu Chi Chang, C. D. Sung, H. T. Tien, C. C. Lee, and J. Y. Chang, “Anisotropic Wet Etching on Birefringent Calcite Crystal”, *Appl. Phys. A*, 00, 1-4 (2004)
- Yu Chi Chang, and etc. “Fabrication and Testing of Polarization Selective Diffractive Optical Elements”, *Conference Proceeding of Optics and Photonics Taiwan 2001 (OPT-2001)*

Languages

English:	Advanced
Chinese:	Mother tongue
French:	Intermediate
Hakka dialect:	Fluent